UNIVERSITY OF CALIFORNIA
Los Angeles

A SEARCH FOR THE CP-VIOLATING DECAY OF THE K-LONG INTO PI-ZERO ELECTRON POSITRON

A dissertation submitted in partial satisfaction of the
requirements for the degree Doctor of Philosophy
in Physics

by

Jacobo Konigsberg

1989

The dissertation of Jacobo Konigsberg is approved.

Edward Hoffman

William Slater

Robert Cousins, Committee Chair

University of California, Los Angeles

1989

TABLE OF CONTENTS

page

LIST OF TABLES

LIST OF FIGURES

ACKNOWLEDGEMENTS

For making this work possible I thank the E791 collaboration:

K. Arisaka, L. B. Auerbach, S. Axelrod, K. A. Biery, P. Buchholz, M. D. Chapman, R. D. Cousins, M. Eckhause, J. F. Ginkel, A. D. Hancock, G. W. Hart, V. L. Highland, G. M. Irwin, D. Joyce, J. R. Kane, C. J. Kenney, W. W. Kinnison, P. Knibbe, J. Kubic, K. Lang, D. M. Lee, J. Margulies, C. Mathiazhagan, W. K. McFarlane, R. J. McKee, P. Melese, E. C. Milner, W.R. Molzon, D. A. Ouimette, J. L. Ritchie, P. Rubin, G. H. Sanders, M. Sivertz, W. E. Slater, Q. H. Trang, J. Urheim, W. F. Vulcan, D. Wagner, R. E. Welsh, R. J. Whyley, R. G. Winter, S. G. Wojcicki, H. J. Ziock.

I am very grateful in particular to:

George Irwin, for getting me out from, (and sometimes into), various software traps. John Kubic, for his skillful assistance. Karol Lang, for many useful discussions and for his effort in corroborating my results. Jeremy Margulies, for shedding light on many issues and for marching together with me on this sometimes tortuous path. Jack Ritchie, for efficient discussions and guidance regarding the intricacies of $K_L^0 \rightarrow \pi^0 e^+ e^-$. Philip Melese, for a great collaborating experience and the many coffees at Kerkhoff. Bill Slater, for reading this work and making valuable suggestions. Tom Graeber, for much help in software development. Claudio Dib, for his useful explanations regarding the theory of $K_L^0 \rightarrow \pi^0 e^+ e^-$ decays. My advisor, Bob Cousins, for his concern that I obtain the best possible training in this field and for his readily available, and always expert, counsel.

The support of the AGS staff at the Brookhaven National Laboratory is greatly appreciated.

The UCLA staff has been most kind and helpful to me: Christine Green, Penny Lucky, C.J. Farrar and Mary Yost. Sharon Wong's assistance has been invaluable.

I could never thank my parents and family enough. Their unconditional love and support has always been the force behind me. Claudia, my wife, is the best companion anyone can have. Her understanding, love, encouragement and advice have made the hard times bearable and the successes so much sweeter.

This work was partially supported by the United States Department of Energy.

VITA

Oct. 25, 1958	Born, Mexico D.F., Mexico
June, 1976	High School Graduation Colegio Hebreo Tarbut, Mexico City
1977-1980	B.Sc. in Physics and Mathematics Hebrew University Jerusalem
1980-1981	Mathematics Teacher Colegio Hebreo Tarbut, Mexico City
1981-1983	M.Sc. in Physics, Hebrew University Jerusalem CONACYT scholarship award Physics Lecturer, HUJ School for Overseas Students
1984-1985	Teaching Assistant, Department of Physics University of California, Los Angeles
1985-1989	Research Assistant, Department of Physics University of California, Los Angeles

PUBLICATIONS & PRESENTATIONS

R. D. Cousins *et al.*, "Search for the decays $K_L^o \to \mu e$ and $K_L^o \to ee$", Phys. Rev. D 38, 2914 (1988).

R. D. Cousins, *et al.*, "Fast Parallel Pipelined Readout Architecture for a Completely Flash Digitizing System with Multi-level Trigger", Nucl. Instr. and Meth., A277, 517 (1989).

C. Mathiazhagan, *et al.*, "New experimental Limits on $K_L^o \to \mu e$ and $K_L^0 \to e^+e^-$ Branching Ratios". Phys. Rev. Lett. **63**, 2181 (1989).

C. Mathiazhagan, *et al.*, "Measurement of the Branching Ratio for the Decay $K_L^o \to \mu\mu$". Phys. Rev. Lett. **63**, 2185 (1989).

J. Konigsberg, "$K_L^0 \to \pi^0 e^+e^-$ Experiments; BNL E791", Proceedings of the International Workshop on Weak Interactions and Neutrinos, Ginosar, Israel, 9-14 April, 1989. To be published in Nuclear Physics B, Proceedings Supplements Section.

J. Konigsberg *et al.*, " $K_L \to \pi^o e^+e^-$ experiments, BNL E791 etc. ". Contributed talk at the Twelfth Workshop on Weak Interactions and Neutrino Physics, Ginosar, Israel, April 9-14, 1989.

J. Konigsberg *et al.*, " $K_L \to \pi^o e^+e^-$ at BNL E791 ". Contributed talk at the Spring Meeting of the APS, Baltimore, Maryland, May 1-4, 1989.

ABSTRACT OF THE DISSERTATION

A Search for the CP-violating Decay of the

K-long into Pi-zero Electron Positron

by

Jacobo Konigsberg

Doctor of Philosophy in Physics

University of California, Los Angeles, 1989

Professor Robert D. Cousins, Chair

The $K_L^0 \rightarrow \pi^0 e^+ e^-$ process has recently been the subject of renewed consideration by both experimentalists and theoreticians. In this thesis I describe the basic ideas that motivate this search and the results of experiment E791, performed at the Brookhaven National Laboratory Alternating Gradient Synchrotron in the period of March to May 1988.

This flavour-changing process is supressed in the Standard Model, with predictions for a branching ratio of the order of 10^{-11}. The decay could have a sizeable CP violating contribution in the decay amplitude ("direct" CP violation). $K_L^0 \rightarrow \pi^0 e^+ e^-$ is therefore a process that would enable us to study the various effects of the still obscure CP violation phenomenon. The observation of this decay at rates larger than those predicted by the Standard Model would be a clear signal for new physics.

Prior to 1988 the limit on the branching ratio was 2.3×10^{-6}. In our experiment we found no events consistent with $K_L^0 \to \pi^0 e^+ e^-$. We collected the equivalent of 10^7 $K_L^0 \to \pi^+\pi^-\pi^0$ events for normalization purposes. The estimated 90% confidence level limit on the branching ratio is: $B(K_L^0 \to \pi^0 e^+ e^-) < 6.0 \times 10^{-7}$. This limit is consistent with tighter bounds established by other recent experiments.

1. INTRODUCTION

The Standard Model of the strong and electroweak interactions described by the $SU(3) \times SU(2) \times U(1)$ symmetry provides a highly accurate description of all known particle physics phenomena. It does not, however, provide natural explanations for many of its *ad hoc* features, such as CP violation, the values of the quark masses, the lepton masses and the coupling constants. While experiments have failed so far to find clear evidence of phenomena beyond the scope of the Standard Model predictions, many new models such as Technicolor, Supersymmetry, Left-Right symmetric models, etc., have emerged in an effort to provide for a natural extension to the Standard Model predicting new, yet unobserved, phenomena.

The experimental effort in the search for new physics follows three main paths. The first is performing experiments at ever higher energy where the new physics, (and some of the not yet observed features of the Standard Model such as the top quark and the Higgs boson) may show up. The second path is making precision measurements of Standard Model parameters such as the "Weinberg angle" or the $\mid \epsilon\prime/\epsilon \mid$ ratio. Deviations from the predicted values will signal new physics. The third is building experiments which search for new phenomena which, at not so high energies, would occur very rarely. This kind of experiments could in principle observe indirectly, through the rare decays of known particles, very heavy mediating particles that may, or may not, be observable at the high energy accelerators.

Experiment E791 at the Alternating Gradient Synchrotron (AGS) in the Brookhaven National Laboratory belongs to this second class of experiments. The experiment design was optimized to search for the decay of the long lived (5.18×10^{-8} sec) neutral meson K_L^0 into an electron and a muon: $K_L^0 \rightarrow \mu e$. This process is not allowed in the Standard Model because it violates the conservation of the Separate Lepton Number. Nonstandard models predict this decay to occur with very low probability. Other decays we have searched for include $K_L^0 \rightarrow \mu\mu$ and $K_L^0 \rightarrow ee$ which, although allowed in the Standard Model via second order electroweak processes, are very supressed.

The search for the $K_L^0 \rightarrow \pi^0 e^+ e^-$ decay is the focus of this dissertation. As discussed in chapter 2, this process could shed some light on the many interesting aspects of the not well understood CP violation mechanism in the Standard Model. This flavour-changing decay is expected to proceed with a branching ratio of only about 10^{-11}. Therefore, in order for it to be observed, an experiment with very high sensitivity needs to be performed. Before 1988 the branching ratio limit[1] was 2.3×10^{-6}. This limit has been recently moved[2,3] to a few times 10^{-8} and experiments are under way to push this limit even lower. As also discussed in chapter 2, the measurement of a rate larger than that predicted in the Standard Model would be a definite signal of new, CP violating, physics. There is still quite a large "window" for this kind of physics to emerge. All this should make the search for $K_L^0 \rightarrow \pi^0 e^+ e^-$ an exciting one.

In order to reach a high sensitivity in a finite running time, one needs to produce many observable K_L^0 decays as cleanly as possible. As described in chapters 3 and 4, this requires a suitable beamline and fast readout and detector systems. In chapter 5 of this work I describe the analysis I have performed on the data taken in our 1988 running period (March through May) while searching for the $K_L^0 \to \pi^0 e^+ e^-$ decay. The final three chapters (6 through 8) deal with the various studies and simulations that, given the fact that no candidates were found, allow us to obtain a limit on the branching ratio of the decay. The final $K_L^0 \to \pi^0 e^+ e^-$ sensitivity reached in this run was greater than that of older experiments but less than our initial expectation. This is mainly due to the small three-body decay geometrical acceptance of the detector (which was optimized for background rejection for $K_L^0 \to \mu e$). It is my hope, however, that this thesis describes clearly enough some aspects of the exciting, and the sometimes not-so-exciting work involved in particle physics experiments.

2. THEORETICAL CONSIDERATIONS

2.1 *CP* violation in $K_L^0 \to \pi^0 e^+ e^-$

The presence of *CP* violation in the mass matrix of the neutral K system results in a small ($O(10^{-3})$) admixture of the $|K_1>$ state in the long-lived $|K_L^0>$ eigenstate. As a result, the $|K_L^0>$ meson is described as a superposition of well-defined *CP* eigenstates such that: $|K_L^0> \approx |K_2> + \epsilon|K_1>$, where $|K_2>$ and $|K_1>$ are odd and even respectively under the *CP* transformation.

There are three distinct classes of amplitudes that can contribute to $K_L^0 \to \pi^0 e^+ e^-$ decays:

$$\begin{array}{lll} \text{(A)} & \mathrm{K}_1 & \to \pi^0\gamma^* \to \pi^0 e^+ e^- \\ \text{(B)} & \mathrm{K}_2 & \to \pi^0\gamma^* \to \pi^0 e^+ e^- \\ \text{(C)} & \mathrm{K}_2 & \to \pi^0\gamma^*\gamma^* \to \pi^0 e^+ e^- \end{array}$$

Amplitudes **A** and **B** proceed through a virtual photon (Fig. 2.1(a)). Given that $CP(\pi^0\gamma)$ is even for a state of zero total angular momentum, a $|K_L^0>$ decay via amplitude **A** violates the *CP* symmetry only due to the small admixture of $|K_1>$ ("indirect" *CP* violation), whereas amplitude **B** violates *CP* directly in the $|K_2>$ decay amplitude ("direct" CP violation). In the class **C** with two intermediate virtual photons (Fig. 2.1(b)), CP is not necessarily violated and the amplitude is regarded as "CP conserving".

Recent theoretical estimates[4,5,6,7,8] of each of these amplitudes independently result in a branching ratio for $K_L^0 \to \pi^0 e^+ e^-$ of the order of 10^{-11}. These estimates are model dependent and lack the exact value of parameters such as the mass of the top quark. The largest discrepancy is in the contribution of the CP conserving part; some calculations[5,9] assign it negligible contribution, while others[10,11] obtain that it may be a large amplitude in the decay. $K_L^0 \to \pi^0 e^+ e^-$ is therefore a process in which the "direct" and "indirect" CP violating amplitudes are of the same order of magnitude, in contrast with the well known $K_L^0 \to \pi^+ \pi^-$ decay, in which the "direct" CP violating part is very suppressed with respect to the "indirect" one. I describe in the next section some of the theoretical considerations entering the calculation of these three different type of amplitudes.

2.2 Calculations and Branching Ratio Predictions

$K_L^0 \to \pi^0 e^+ e^-$ occurs via the electroweak process $s \to de^+e^-$. The absence of flavor-changing neutral currents in the Standard Model does not allow this transition at the tree level Feynman diagrams. The leading contribution thus occurs at the one loop level of the electroweak interactions and is therefore very supressed.

In estimating the indirect CP violating amplitude one can use the identity[12]:

$$B(K_L^0 \rightarrow \pi^0 e^+ e^-)_{\text{indirect}} \equiv$$

$$B(K^+ \rightarrow \pi^+ e^+ e^-) \times \frac{\tau_{K_L}}{\tau_{K^+}} \times \frac{\Gamma(K_1 \rightarrow \pi^0 e^+ e^-)}{\Gamma(K^+ \rightarrow \pi^+ e^+ e^-)} \times \frac{\Gamma(K_L^0 \rightarrow \pi^0 e^+ e^-)_{\text{indirect}}}{\Gamma(K_1 \rightarrow \pi^0 e^+ e^-)} \quad (2.1)$$

The first two factors are experimentally[13] known to be equal to 2.7×10^{-7} and 4.2, respectively. The last factor is simply $\mid \epsilon^2 \mid$ by definition. The theoretical estimation of the third factor is model dependent, being equal to 1 if the transition between the K and the π involves an isospin change of 1/2 ($\Delta I = 1/2$), and equal to 4 if $\Delta I = 3/2$. If both amplitudes are present and interfere with each other the value is not well known. A chiral perturbation theory calculation[9] yields two values of 0.25 or 2.5 depending on possible solutions for normalization coupling constants. A value of unity for this factor results in:

$$B(K_L^0 \rightarrow \pi^0 e^+ e^-)_{\text{indirect}} = 0.58 \times 10^{-11}$$

The problem in estimating the indirect CP violating amplitude straightforwardly from the $K_1 \rightarrow \pi^0 e^+ e^-$ diagrams stems from the fact that this part is mediated by the real part of the Hamiltonian, which allows light quarks (u) to enter in the calculations. QCD corrections in this case may be quite large and are not well defined. Efforts to estimate these short-distance contributions, using chiral perturbation theory, have been made[8] which yield similar results to the one quoted just above. However, long-distance contributions may also be important in understanding the magnitude of the amplitude. An experimental measurement of $K_S^0 \rightarrow \pi^0 e^+ e^-$ would provide a direct determination of the third factor above and thus supply a precise prediction for the contribution of this amplitude.

The direct CP violating amplitude is mediated by the imaginary part of the Hamiltonian and includes contributions only from the heavy c and t quarks. With a heavy top quark ($m_t \approx m_W$), this calculation is expected to be less dependent on QCD corrections, on the renormalization point μ and on long-distance contributions. Three type of diagrams are expected to contribute in the amplitude. Figures 2.2(a) to 2.2(c) show the "electromagnetic penguin", the "Z penguin" and the "W box" diagrams. Even though the Z and W contributions are not negligible at large m_t, due to the smallness of the Z coupling to the electrons, the "electromagnetic penguin" still is expected to dominate the decay. The calculations result in a predicted branching ratio of:

$$B(K_L^0 \rightarrow \pi^0 e^+ e^-)_{\text{direct}} \approx 10^{-11}$$

The fact that the two types of CP violating effects may be of comparable magnitude will lead to an interference term in the total decay rate. One could imagine measuring a full interference pattern (as has been done for $K_L^0 \rightarrow \pi^+\pi^-$), where one sees both the regime of $K_S^0 \rightarrow \pi^0 e^+ e^-$ followed by that of $K_L^0 \rightarrow \pi^0 e^+ e^-$, with an interference region between the two regimes of exponential decays. This would measure not only the two independent rates but also the phase between the "indirect" and "direct" amplitudes.

We now turn to the CP conserving case via two photons. This process, although being of higher order in α (the electromagnetic coupling constant), is not *a priori* negligible in comparison with either of the CP violating amplitudes which are also supressed precisely for containing factors that are related to CP violation. If $\epsilon_1^\mu \epsilon_2^\nu M_{\mu\nu}$ is the amplitude for $K_L^0 \to \pi^0\gamma\gamma$ then[7]:

$$M_{\mu\nu}(q_1, q_2, k) = A(k\cdot q_1, k\cdot q_2)\Big[q_{2\mu}q_{1\nu} - q_1\cdot q_2 g_{\mu\nu}\Big] +$$

$$B(k\cdot q_1, k\cdot q_2)\left[\frac{k\cdot q_1\, k\cdot q_2}{q_1\cdot q_2}g_{\mu\nu} + k_\mu k_\nu - \frac{k\cdot q_1}{q_1\cdot q_2}q_{2\mu}k_\nu - \frac{k\cdot q_2}{q_1\cdot q_2}q_{1\nu}k_\mu\right] \quad (2.2)$$

where $\epsilon_{1,2}$ are the polarization vectors for the on-shell photons, $q_{1,2}$ their momenta, and k is the momentum of the kaon. The term with the A form factor corresponds to an S-wave photon pair and becomes small when it picks up a factor of m_e when the electrons are attached to form the $K_L^0 \to \pi^0 e^+ e^-$ process. The B term contains S and D-waves and does not suffer the mass suppression, but it is estimated very differently by the "Vector Meson Dominance" model (VMD) and the chiral Lagrangian method. (The CP nonconserving and off-shell photon form factors are neglected.)

In chiral perturbation theory the prediction[9] for $K_L^0 \to \pi^0 e^+ e^-$ is:

$$B(K_L^0 \to \pi^0 e^+ e^-) \approx 10^{-14} - 10^{-15} \quad (CP \text{ conserving, Chiral})$$

In the VMD calculations[7,11,10] the predicted upper limit range is:

$$B(K_L^0 \to \pi^0 e^+ e^-) \leq 2 - 8 \times 10^{-11} \quad (CP \text{ conserving, VMD})$$

The direct measurement of $K_L^0 \to \pi^0\gamma\gamma$ can clearly be used as input to these calculations. In particular, one could separate the A and B amplitudes by making a measurement on the Dalitz plot of the two-photon invariant-mass distributions[12]. In addition, the relative rates of $K_L^0 \to \pi^0 e^+ e^-$ and $K_L^0 \to$

$\pi^0\mu^+\mu^-$ could help understand better the A term, in which the lepton mass plays an important role.

If both the CP conserving and CP violating amplitudes are present with equivalent strengths, then a Dalitz plot distribution would show a large lepton/antilepton energy asymmetry[10].

The conclusion is that a $K_L^0 \to \pi^0 e^+ e^-$ experiment, in order to measure the different contributions of these amplitudes, would have to reach a level of 10^{-12} or better in sensitivity. Even if such sensitivity is not achieved, these experiments can view a fairly large "window" for physics beyond the Standard Model.

In the next section I make some comments on nonstandard models for $K_L^0 \to \pi^0 e^+ e^-$.

2.3 $K_L^0 \to \pi^0 e^+ e^-$ in non-Standard Models

Two questions are of interest. The first is whether nonstandard models allow $K_L^0 \to \pi^0 e^+ e^-$ at rates larger than those predicted by the Standard Model. The second is whether CP is violated in this cases.

In principle it is possible for nonstandard models to conserve CP in their leading amplitude[8]. If there is a scalar-scalar vertex in the form $\bar{s}d\bar{e}e + h.c.$ it would permit $K_L^0 \to \pi^0 e^+ e^-$ in the absence of CP violation. However, such an operator in the effective lagrangian would allow $K_L^0 \to ee$ without helicity suppression. The current experimental limit[14] $B(K_L^0 \to ee) < 3.1 \times 10^{-10}$ excludes the possibility that $K_L^0 \to \pi^0 e^+ e^-$ can occur through a CP conserving vertex at a rate in excess of $\approx 10^{-12}$, which is near the bound of the Standard Model CP conserving prediction. One concludes that if $K_L^0 \to \pi^0 e^+ e^-$ is observed at a rate larger than any of the Standard Model estimates, the nonstandard physics must involve new CP violation.

Various nonstandard models can be considered for the $K_L^0 \to \pi^0 e^+ e^-$ decay[8]. A model with lepto-quarks in which the lepto-quark couples only to a single helicity of quarks and leptons might allow $K_L^0 \to \pi^0 e^+ e^-$ to occur at a rate substantially larger than the predicted by the Standard Model[15]. If there are two lepto-quarks with different $U(1)$ charges the decay can proceed without violating CP and, as we discussed above, this process must be small. A composite model such as the Composite Technicolor Standard Model[16] (CTSM) allows $K_L^0 \to \pi^0 e^+ e^-$ at about the same magnitude of the maximum allowed Standard Model rate, so an observation would not be a clear signature of CTSM. Supersymmetric models do not seem to yield larger rates than the Standard Model either. In general, most nonstandard models are very constrained by the known limits and known characteristics of flavor-changing currents.

3. EXPERIMENTAL APPARATUS

In order to reach a high sensitivity in a finite running time, one needs to produce as many observable K_L^0 decays as possible. This requires high intensity proton beams impinging on a suitable target. A neutral beam is then produced by magnetically deflecting away charged particles. The neutral beamline needs to be well collimated and shielded, and the neutron to kaon ratio beam needs to be kept as small as possible. All this, together with a good vacuum decay region, should yield as reduced as possible accidental rates. In order to handle the high kaon decay rates in the detector with little or no dead-time, fast trigger logic and a fast readout system are required (Ch. 4).

In this chapter I describe the experimental apparatus and the conditions under which our search for $K_L^0 \rightarrow \pi^0 e^+ e^-$ was performed. These conditions were, of course, identical for the other K_L^0 decays studied in the 1988 run: $K_L^0 \rightarrow \mu e, K_L^0 \rightarrow \mu\mu$, and $K_L^0 \rightarrow ee$

The experiment took place in the Alternating Gradient Synchrotron (AGS) at the Brookhaven National Laboratory. The running period lasted from January until May 1988. Data taking for $K_L^0 \rightarrow \pi^0 e^+ e^-$ began on March 1988.

3.1 Accelerator & Beamline

The AGS supplied our beamline (B5) with an average of 2.75×10^{12} protons every pulse (3.2 seconds) with an energy of 24 GeV/c^2. These protons were extracted continuously over a period of approximately 1.4 seconds.

The incoming proton beam hit a copper target measuring $3 \times 3 \times 190$ mm^3 (1.26 nuclear interaction lengths). Charged particles were swept by a dipole magnet (with a set of lead foils to convert photons) while the neutral beam coming at 2.75 degrees from the target traveled through a series of collimators (and another sweeping magnet) on its way to a 10-meter-long vacuum decay region. This decay volume ended with a 20 mil mylar window through which the K_L^0 decay products traversed. The K_L^0 beam spanned a solid angle of 60 μsr. Figure 3.1 shows the elevation view of the elements that form the E791 neutral beamline. The rates through the various counters were in the range of 3 to 6 Mhz.

3.2 Tracking and Triggering

Figure 3.2 shows a plan view of the E791 detector. The coordinate system adopted in all aspects of the experiment, and to which I will refer to in the rest of this thesis, is defined such that the positive z axis points in the beam direction, the positive y axis points from the floor to the ceiling, the positive x axis points left when one stands with one's back to the target. The origin is the nominal target position. The "downstream" direction is defined by going from the vacuum window along the the beam direction. The opposite direction is referred to as "upstream".

In this section I describe the detectors used in tracking and triggering: the drift chambers (DC), analyzing magnets and the trigger scintillation counters (TSC). The rest of the detectors are used mainly for particle identification purposes and will be described in section 3.3.

A spectrometer of five drift chamber modules and two dipole magnets is used for measuring charged particle's trajectories and momenta. Low mass materials are used in the chambers to minimize the effect of multiple scattering in order to achieve good momentum measurements. Table 6.1 lists the radiation length of every detector in the experiment. Helium bags are placed in between drift chamber modules in order to minimize interactions of the neutral beam traversing the detector and thus reduce the accidental rates. Two analyzing magnets are used in order to measure the track's momenta twice and thus improve the two-track invariant mass resolution. The strength of the two magnets is set such that they give equal and opposite transverse (in the x direction) momentum impulses of about 0.300 GeV/c^2 to charged particles, thus restoring the original track direction after the second magnet. This setup optimizes the background rejection[17] for $K_L^0 \rightarrow \mu e$, however it reduces dramatically the acceptance for three body decays such as $K_L^0 \rightarrow \pi^0 e^+ e^-$.

Each drift chamber module contains two vertical and two horizontal planes of sense wires, measuring $\{x, x'\}$ and $\{y, y'\}$ coordinates, respectively. The sense wires are 1.0 cm apart on each plane. The x' and y' planes are offset by 0.5 cm from the x and y planes. The two measurements in each dimension allows to resolve the left-right ambiguity of traversing tracks. The sense wires are 0.001 inch gold plated tungsten. Copper-beryllium field wires, 0.0043 thick, (held at 2500 volts) shape the electric field surrounding the sense wires. The module's walls are 1 mil aluminized mylar. An aluminum frame supports the whole structure. A gas mixture of 49% argon, 49% ethane and 2% ethanol flows through the modules. The sense wires are capacitively coupled to preamplifier and discriminator circuit boards. Signals are then carried to 2.5 ns least count, 6-bit TDC's[18], and to the Level 1 logic for triggering the experiment. The time measurement allows one to measure the track position in the chamber with an intrinsic resolution of about 120μm. The average electron drift velocity is 50 μm/ns. The wire position resolution is about 25μm and wire efficiencies were, on average, better than 99%.

The first analyzing magnet is a 48D48 magnet: a dipole with a pole piece measuring 48 inch $\times$ 48 inch in x and in z, respectively. It has a 37 inch wide gap. It operates at approximately 1991 Amps and has a maximum central field value of about 6.2 Kgauss. B_y, the main field component, points in the negative y direction. The second magnet is a 96D40 magnet with a 44 inch gap. It operates at about 2477 Amps and produces a maximum central field of approximately 6.4 Kgauss. Both magnets have, upstream and downstream of them, iron frames which serve the purpose of constraining the stray field away from the detectors. We mapped the B_y and B_x components of the magnetic field over most of the volume of the spectrometer[19]. The B_x component was as large as 10% of the B_y component in some places in the 48D48 and only about 1% in the 96D40. Due to various uncertainties in the measuring apparatus, the measured B_x component was not used. Instead we used B_x (and B_z) from

2-dimensional Poisson simulation[20].

The two modules of trigger scintillating counters, located upstream and downstream of the Čerenkov counter, are each composed of one plane of 60 x-measuring and one plane of 63 y-measuring slats. The x (y) measuring slats are 1.80 (1.28) m long and 2.014 (2.814) cm wide. The upstream slats are 0.5 cm thick and the downstream ones 1.0 cm. This minimizes the probability of knock-on electrons onto the Čerenkov counter. An x measuring slat shares its top photomultiplier tube (PMT) with the adjacent slat on one side while the bottom tube is shared with the adjacent slat on the other side. We used one-inch Hamamatsu R1398 PMT's to which the slats were coupled using a sillicone rubber with an index of refraction similar to the Kyowa glass scintillators. (Kyowa glass is a brand of doped polystyrene). The slats are individually wrapped in aluminized mylar and each plane encased in a light-tight box. The analog signals were carried to ECL-output discriminators and from there to both to the L1 trigger logic and to TDC's. The efficiency for registering the passage of a charged particle was estimated to be 0.998. The time resolution was approximately 1.7 nsec. The attenuation length of the scintillator material was measured to be about 1.3 m. Light propagates at a speed of about 0.138 m/nsec along the counters.

3.3 Particle Identification

In this section I describe the detectors used for particle identification purposes in the experiment (Ch. 7): the Čerenkov counter, the lead glass array, the muon hodoscope and the muon range-finder.

The Čerenkov counter is a gas threshold device used to generate fast electron signals for the Level 1 trigger and to identify electrons in the offline analysis. We used a gas mixture of 40% nitrogen and 60% helium, corresponding to an index of refraction of n = 1.00014 or a threshold of $\beta = 0.99986$. Charged pions with momentum lower than about 8.2 GeV and muons with momentum less than about 6.2 GeV will, in general, fail to produce signals in the counter. The index of refraction was monitored by means of a Mach-Zehnder interferometer illuminated with a helium-neon laser. The momentum threshold accuracy is within ± 0.25 MeV. Each Čerenkov aluminum box is 3 meters long by 1.6 meters wide. The sides perpendicular to the particles' trajectories are 1/32 inch thick in order to reduce the amount of material traversed by the particles. There are 8 0.25 inch thick lucite spherical mirrors in each box, arranged in a matrix with 2 rows, in the x direction, of 4 mirrors each. The mirrors are supported by a 0.020 inch aluminum frame and are coated by a thin aluminum film. Each mirror measures 35 cm in x by 89 cm in y, and has a radius of curvature of 2.2 m. At the focal point of each mirror there is a 6.5 inch quartz window onto which the photons radiated within the gas are reflected. Aluminized Mylar light funnels bring the light to 5 inch RCA 8854 Quantacon PMT's which have their window coated with a thin film of p-terphenyl (which acts as wave-length shifter to improve the tube's response to the photon's spectrum). The average electron produces approximately five photoelectrons. The tubes are protected from the fringe magnetic field by three layers of magnetic shielding metal. A continuous flux of dry nitrogen gas is maintained through the tubes in order to prevent damage from helium penetration. The Čerenkov signals are carried to the Level 1 logic circuits and to TDC's and charge-integrating bilinear, 8-Bit, flash ADC's[21], which have a total dynamic range of 100pC. The efficiency of these counters in particle identification is discussed in Chapter 7.

The lead glass array (Fig. 3.3) functions as an electromagnetic calorimeter. It is composed of three distinct layers of detectors. The upstream-most layer is formed by 52 lead glass blocks measuring 0.109 m in x, 0.90 m in y and 0.10 m in z. There are two rows of 13 blocks each on each side of the detector. Each block presents 3.3 radiation lengths to the incoming particles. This layer is referred to as "the converter" and it serves the purpose of converting photons (and, of course, electrons) from K_L^0 decays into electromagnetic showers. Each of the 12 blocks closest to the beam, on each side of the detector, is attached to fast Amperex XP3642 phototubes while the rest of the blocks have slower EMI 9531R tubes. The blocks are read out into both TDC's and ADC's.

Just downstream of the converter blocks, two planes of 5.1 cm wide, 1.5 cm thick, x and y-measuring, scintillating slats are used for precise timing and position measurement of electromagnetic showers. These counters are dubbed "finger counters" or simply "FNG". They are made of SCSN-38 Kyowa glass and wrapped in aluminized mylar and black vinyl. There are 27, 1.93 m long, x-measuring slats on each side of the detector. Their top is attached with light guides to Amperex 56AVP PMT's while the bottom uses EMI 9902 phototubes. The 1.43 m long y-measuring counters have a single XP2230 PMT in the side far from the beam. There are a total of 26 of these slats on each side of the detector. The speed of light in the scintillator was measured to be about 0.145 m/nsec. Signals from these counters are brought to the Level 1 circuits (to form the "photon condition" of the trigger -Sec. 4.1) and read out by both TDC's and ADC's.

The TDC time measurements are corrected for signal path-lengths, for hit position along the counters and for signal pulse-height (using the ADC information). The time resolution is approximately 1.1 nsec. The ADC information, corrected by subtracting a pedestal and using the appropriate slope, yields a pulse-height measurement in units of pico-Coulombs. Weighting properly the pulse-heights of the counters involved in a shower yields a good measurement of the position of the showering particle with a resolution of about 1.5 cm (Sec. 5.3).

The last section of the lead glass array is formed by two walls of 15.3 cm in x by 15.3 cm in y by 32.2 cm in z lead glass blocks. These 10.5 radiation-length back-blocks absorb all the energy of the electromagnetic showers, and, together with the converter blocks provide the only means of measuring photon energy in the experiment. Their coarser segmentation, compared to the finger counters, also provides a shower position measurement. There are a total of 216 blocks arranged in 12 columns of 9 blocks each, on each side of the detector. They span a total area of 1.38 m in x by 1.84 m in y. The inner two columns of blocks and the 4 central blocks of the third column are attached to fast 5 inch Amperex 58AVP and 58DVP type phototubes. The rest of the blocks are attached to slower EMI 9618R 5 inch tubes. A temperature-controlled light-tight wooden hut houses the whole lead glass array. Signals from the back blocks are input to both TDC's and ADC's. Table 3.1 lists some of the properties of the lead glass, converter and back blocks. The energy resolution of the array varies with the track's position due to the different types of phototubes. On the average, for the fast blocks the resolution was given by: $\sigma_E/E \approx 2\% + 15\%/\sqrt{E}$. For the slower tubes a better resolution was obtained: $\sigma_E/E \approx 2\% + 7\%/\sqrt{E}$ (E is the total energy in Gev/c^2).

In our $K_L^0 \to \pi^0 e^+ e^-$ search, the Čerenkov counter and the lead glass array are primarily used for electron identification and charged pion rejection purposes (Ch. 7). The muon hodoscope and range-finder are used in this analysis only in a very limited fashion, mainly for selecting K_{e3} decays for particle identification efficiency studies. We make vetoes on these detectors on the charged pion candidate in order to reduce the probability that the particle is a muon.

The muon hodoscope is formed by two planes of 18.7 cm wide, 2.54 cm thick Bicron BC408 scintillator slats. It is located downstream of a 0.91 m thick steel wall which acts as a hadron filter. There are 14 y-measuring 2.286 m long slats and 11 2.692 m long x-measuring slats on each side of the detector. All slats are wrapped in aluminized mylar and photo-grade polyethylene. Two-inch Amperex XP2230 PMT's are attached to both ends of the x-measuring counters and to the end far from the beam of the y-measuring counters. Signals from the muon hodoscope were sent to both the Level 1 trigger logic and to TDC's.

The muon range-finder[22] is made of planes of proportional wire-chambers placed in between marble and aluminum, 7.62 cm thick, degrader planes. It is designed to measure the momentum of muons in the range of 1.5 to 6.0 GeV/c. We use 150 planes of marble and 50 of aluminum, and 13 pairs of x and y-measuring proportional chamber planes. The amount of degrader in between chamber planes is such that $\Delta p/p \approx 10\%$ at each gap. A helium bag is placed in between the two arms of the range-finder to reduce interactions of the beam with air. The chamber planes are composed of panels containing 8 cells measuring 1.2 by 2.1 cm, strung with two parallel wires spaced 1.06 cm apart. The x-measuring planes contain 12 panels, each 3.01 m long, while the y-measuring planes have 16 panels 2.25 m long. Both wires are held at an average voltage of

2650 V in a gas flow mixture of 49% argon, 49% ethane and 2% ethanol. The signals pass through amplifier-discriminator circuits on their way to electronic latch-modules which register in one channel the OR of all 8 cells in a panel. The total number of latch channels is therefore 724. The efficiency of a typical plane for registering the passage of a muon is about 96%.

4. DATA AQUISITION

In this chapter I describe in detail the processes involved in the data taking of the experiment. Various detector signals are examined in real time using fast electronic logic modules to decide whether an event may be of interest. If so, all signals are digitized and then read out into an online computer which in turn performs fast software calculations to further reduce the number of interesting events. The remaining events are written into magnetic tape for further analysis. Each event has a word associated with it which contains the information on why that particular event triggered the detector: the Level 1 (L1) trigger word.

4.1 Level 1 Trigger

Our first level trigger[23] (Level 1) was a hardware trigger designed to detect events of the type $K_L^0 \rightarrow e^+e^-\gamma + X$, of which $K_L^0 \rightarrow \pi^0 e^+e^-$ is a subset. Two charged tracks, one on each side of the spectrometer, defined by a suitable coincidence of hits in the first three drift chamber planes and in the trigger scintillator counters, constituted our minimum bias trigger (MB). In addition, signals provided by the Čerenkov counter were required for the two tracks to be consistent with electrons. The scintillator hodoscope ("finger counters") used in our lead glass array served to identify photons. For the other searches carried out in the experiment, signals from the muon hodoscope were used to provide muon triggers. I describe below the details of how these triggers were formed.

First, a Level 0 (L0) strobe was formed using the discriminated signals from the trigger scintillation counters. The two sides of the spectrometer were treated identically. Therefore, unless otherwise specified, in the following descriptions I will normally refer only to the left side's nomenclature. The signals coming from the top and bottom phototubes in the x-measuring counters were mean-timed. All the upstream x mean-time outputs were OR'ed to provide a single logical signal, LTFX. The horizontal (y-measuring) upstream counters were not used in the trigger. The downstream x mean-time outputs were OR'ed in four groups of consecutive counters, the four OR outputs where then properly delayed to be in coincidence with a signal formed by the OR of all y-measuring downstream counters. The coincidence signal was labeled LTBX. A programmable logic unit (PLU) enabled the L0 strobe if LTFX and LFBX and the corresponding strobes for the right side, RTFX and RTBX, were all asserted and in time.

A second PLU examined the signals coming from the first two drift chamber modules. Signals from adjacent x, x' (and adjacent y, y') wires were mean-timed in each of the modules. The mean-time outputs for x, x' and y, y' were OR'ed independently to generate two output signals per module: LD1X, LD1Y and LD2X, LD2Y. The analogous signals were formed for the right side chambers, and all eight signals were fed into another PLU. To have a track on one of the sides of the detector was required that 3 out of 4 of the above mentioned signals on the corresponding side would be asserted. If a track was found on both sides, a strobe signal, D12, was asserted.

If both the L0 and the D12 strobes are enabled we define it as having a minimum bias trigger. This trigger was pre-scaled, in hardware, by a factor of 1,000 in the initial part of the run. The pre-scale factor was later changed to 2,000.

The particle identification triggers were formed from the signals of Čerenkov counters and the muon hodoscope. They were generated only if the minimum bias requirement was met. If the OR of all eight signals from one of the Čerenkov counters was set, and in time with the minimum bias signal, we would consider having a potential electron on that side, and a bit would be set flagging the fact, e_L. Another bit was set, μ_L, if the muon hodoscope signals (OR of x mean-times set, and OR of y's set) were consistent with a muon candidate.

A condition for identifying photons was also established in the L1 trigger by examining the signals from the finger counters. The signals from the x-measuring counters were all mean-timed. A cluster of hits in either x or y was defined as one or more consecutive hit counters. All that was required to identify the possible presence of a photon was that there would be two or more clusters in either one of the four modules: x and y, right and left. Presumably one of the clusters would be associated with the track and one with a photon. The timing resolution of this trigger was approximately 30 ns.

Events for which both the electron bits on both sides of the detector were set and the photon condition was satisfied were identified by having a particular bit set in the L1 trigger word, the "$ee\gamma$" bit.

Table 4.1 lists all the different physics triggers that were implemented simultaneously during the run, together with the corresponding bit number that was set in the L1 trigger word. No vetoes were allowed in any of channels used for our rare K_L^0 decays searches. In addition to physics triggers we also had, during data taking, a number of calibration triggers in which pulses of laser light and LED's were used to monitor various of the detectors' performance. Figure 4.1 shows a schematic of the logic used in the L1 trigger.

4.2 Readout System

We used a fast custom-built readout system[24] which digitized all signals into ADC's, TDC's and latches within about 250 ns from the time of the particles' passage through the detector. Figure 4.2 shows a simplified schematic of the E791 readout.

The ability to store up to two events in the front-end of the digitizing modules, along with a highly parallel sparse data scan for reading out the events, resulted in a speedy and virtually deadtimeless readout. By physically connecting every electronic data crate with a farm of up to eight dual-port memory 3081 emulating machines[25], a 48 byte-wide bus was effectively used. Reading an event with a clock of about 130 ns wide strobes took only a few microseconds. When one of the 3081/E's memory filled up with data, a readout supervisor circuit made another one available and signaled the CPU of the full one to run a software filter (Level 3) on the accumulated data. Events passing this filter got uploaded into a micro-Vax computer to be written out to magnetic tape.

4.3 Online Filter

For all events, the Level 3 (L3) online algorithm found a set of hits in the upstream spectrometer (first three drift chamber planes) that would be consistent with a charged track on each side of the detector. It used a table which contained information (in terms of $\int B_y(z)dz$) about the magnetic field in the spectrometer. A calculation of the invariant mass of the charged pair was then performed assuming different mass possibilities for the particles.

If the event's mass was consistent with the K_L^0 mass for a two body decay of interest, the event was uploaded with no further delay. If the event, with the appropriate L1 bit for a $K_L^0 \rightarrow \pi^0 e^+ e^-$ decay, did not pass the two body requirement, it was then tested for consistency with having at least two photons (one on each side of the detector) in the lead glass back blocks[26]. A cluster finding algorithm found clusters of energy in these blocks, searching for a pattern in which there are two electrons (one on each side of the array) and a photon or more, all within a given time window. If the event satisfied this condition it was uploaded and written out. A cluster was identified as an electron if the principal block (the block with largest energy in the cluster) had an energy of at least 0.2 GeV and a total energy of at least 1 GeV. Photons needed to satisfy the same constraint on the energy of the principal block and to have at least a total energy of 0.4 Gev.

On the average, we wrote about 200 events (of all types) to tape each spill. At the end of our running period we collected about 1400 tapes, with about 90,000 events per tape.

4.4 Trigger Efficiencies

There were three distinct types of inefficiencies in the triggers used in our $K_L^0 \to \pi^0 e^+ e^-$ search. Since we normalize our sensitivity to the number of $K_L^0 \to \pi^+\pi^-\pi^0$ events obtained from the minimum bias data, only the relative efficiencies of the physics triggers to that of the minimum bias trigger are relevant to branching ratio measurements.

The first inefficiency to consider was in the generation and propagation of the L1 dilepton trigger bits. The second one resulted from the implementation of the photon condition in the L1 trigger. The third inefficiency came in from the L3 online filter.

By studying minimum bias events and using our offline particle identification one can determine whether a given event should or should not have the L1 dilepton bit set. It was determined[27] that about 1.5% of the events that should have had the dilepton bit set did not have it. This inefficiency increased with beam intensity. The number quoted here is the one corresponding to our average 2.75×10^{12} protons on target per AGS pulse.

In order to study the efficiency of the photon condition we used, once more, minimum bias events. An offline program identified, for events that have the $e_L e_R$ L1 bit set, clusters of adjacent finger counters hit, with times within a 30 ns window. This window corresponded approximately to the time window in the logic modules used in conforming this trigger (Sec. 4.1). If the offline routine decided that the L1 photon condition (two or more clusters in either of the four finger modules) was satisfied, the $ee\gamma$ L1 trigger bit was checked. We measured the efficiency of the photon condition to be $96.8 \pm 0.1\%$. This number is an average of two cases. The first when the requirement was that the $\mathrm{e_L e_R}$ bit would be the only L1 dilepton bit set (96.8% efficiency) in the events under consideration, and the second one when no such requirement was made (96.7% efficiency).

In the initial part of our running period (until run # 2565, which was 32.1% of the total run), the photon condition was not implemented and the $ee\gamma$ bit was set to be identical to the $\mathrm{e_L e_R}$ bit. However, there was a 0.8% inefficiency of unknown origin. Combining these efficiencies we obtain the photon condition efficiency to be $98.2 \pm 0.1\% \pm 1.0\%$. The first error is statistical and the second systematic. The latter includes the effects of using different size time windows and looking at different data sets. This number is ϵ_{L1} in the sensitivity calculation in Chapter 8.

The efficiency of the L3 filter was calculated[26] by applying separately the L3 conditions on well identified electrons (from K_{e3} decays) and photons (from the final $K_L^0 \to \pi^+\pi^-\pi^0$ sample). We calculated these efficiencies as a function of energy bins and used the Monte Carlo $K_L^0 \to \pi^0 e^+ e^-$ energy distributions for electrons and photons to determine the overall efficiency for the L3 trigger for this decay. Given a $K_L^0 \to \pi^0 e^+ e^-$ event, to each decay product corresponds an efficiency depending on its energy. A random number between 0 and 1 was then selected, if this number was larger than the corresponding efficiency then we would throw the event away. All four decay products needed to pass this test for the event to be kept. The overall efficiency was simply the ratio of the number of events that passed the test to the total number of events that were tested. We obtained an efficiency of $69.1 \pm 1.5\% \pm 1.5\%$. The first error is statistical, the second systematic. The systematic error was obtained by changing the efficiencies for all energy bins by ± 1 sigma. This changed the answer by about 2% but overestimates the change. A conservative estimate was an error of 1.5%.

The large inefficiency is likely to have resulted from using only the back blocks in the energy calculation. Fluctuations in the longitudinal development of the electromagnetic shower can result in low depositions of energy in these blocks especially at low energies. We in fact found very low efficiencies in the low energy regime.

We had an extra source of inefficiency in the L3 trigger due to a mistake in the software. As mentioned above, events were first examined to determine if they are consistent with a two-body K_L^0 decay. Only if they failed they were examined by the "three-body" filter. After run number 2520 a colinearity cut was implemented on the two-body filter; events with colinearity greater than 20 mr would be failed and passed on to the three body filter. However, for events that failed due to colinearity, the wrong tracks' parameters were passed to the three-body filter. These events had therefore to be ignored in the offline analysis. By running our Monte Carlo simulation we determined that $75\% \pm 3\%$ of all $K_L^0 \rightarrow \pi^0 e^+ e^-$ events had colinearity smaller than 20 mr. The two-body colinearity cut was applied during the last 29% of the run. This corresponds to a loss of about 15% in efficiency.

5. DATA ANALYSIS

In searching for $K_L^0 \rightarrow \pi^0 e^+ e^-$ candidates, the offline event-selection program sets a series of requirements (cuts) to be satisfied by the tracks and the two photons from the prompt π^0 decay. The copious $K_L^0 \rightarrow \pi^+ \pi^- \pi^0$ decay is the K_L^0 decay that bears the closest similarity to $K_L^0 \rightarrow \pi^0 e^+ e^-$ and is therefore used as our normalization signal. Except for particle identification type cuts, all cuts are applied identically to both $K_L^0 \rightarrow \pi^0 e^+ e^-$ and $K_L^0 \rightarrow \pi^+ \pi^- \pi^0$ candidates. There are distinct requirements for the charged tracks, for the photon part of the event and for the full reconstructed event.

The track parameters, momenta and positions, are those obtained by the Level 3 Filter (L3), described in section 4.3. Two good tracks are defined by having their vertex within a fiducial region in the decay volume. The vertex z position and its divergence from the beam center are constrained. The x position of the tracks must clear the central flange of the vacuum window. The tracks are transported (swum) throughout the detector, using the measured magnetic field, assigning a predicted position at each detector element (Sec. 5.1). Each detector element is then studied in order to find hits that would be consistent with the projected track. Different criteria of consistency, such as time, position and pulse height, are applied in the different counters (Sec. 5.2 to 5.4). Electron candidates must have momenta lower than 8.0 GeV (the Čerenkov pion threshold) and satisfy particle identification requirements made in the Čerenkov counter and in the lead glass array (Sec. 5.3,7.2). The maximum kinematically allowed invariant mass for the charged pair in a $K_L^0 \to \pi^0 X^+ X^-$ decay is $(m_{K_L^0} - m_{\pi^0}) = 0.3627$ GeV. We require that $m_{e^+e^-}$ and $m_{\pi^+\pi^-}$ be less than 0.370 GeV for $K_L^0 \to \pi^0 e^+ e^-$ and $K_L^0 \to \pi^+\pi^-\pi^0$ respectively.

Photons are identified in the lead glass and "finger counters" by a cluster finding algorithm (Sec. 5.3) that had previously selected clusters associated with the event tracks. The resulting cluster information includes energy, position and timing measurements. Due to the coarse segmentation of the lead glass array, special care is taken so that photon associated clusters don't overlap with the ones associated with tracks.

In section 5.4 the event reconstruction is described in detail. By constructing a $\chi^2_{\pi^0}$ with the measured photon positions and energies, all possible photon pair combinations, with a photon on either side of the detector, are tested for consistency with coming from a single π^0 decay at the track vertex. This $\chi^2_{\pi^0}$ is minimized constraining the invariant mass $m_{\gamma\gamma}$ of the photon pair to be equal to m_{π^0}, and a cut on $\chi^2_{\pi^0}$ applied. All four particles in the event must be in time. Each π^0 candidate is then combined with the two tracks in order to reconstruct K_L^0 candidates. The photon trajectory (a straight line), from the event vertex to the lead glass must go through the fiducial volume of the detector, clear of detector edges and material.

Table 5.5 summarizes the final selection criteria used in analysing the data while Tables 5.1 to 5.4 list the cuts applied in the preliminary stages of the analysis (Sec 5.2). The final sample of $K_L^0 \to \pi^0 e^+ e^-$ and $K_L^0 \to \pi^+\pi^-\pi^0$ candidate events, with a colinearity angle, (Fig. 5.6), $\Theta_c^2 \leq 50$ μsr, and with a reconstructed mass in the range $0.450\text{GeV} \le m_{\pi^0 e^+ e^-} \le 0.550\text{GeV}$, is presented in the form of scatter plots of these two variables. Figure 5.7(a) shows the remaining $K_L^0 \to \pi^0 e^+ e^-$ candidates and Fig. 5.7(b) the $K_L^0 \to \pi^+\pi^-\pi^0$ sample. Figures 5.8 and 5.9 are the projections in mass and colinearity of Fig. 5.7(b).

5.1 Particle Transport

By specifying a particle's momentum and direction cosines at a given z position, the offline analysis program is capable of transporting, or "swimming", a particle from a given position in the detector to another new position. Swimming in the magnetic field is performed by means of a fourth-order Runge-Kutta[28] integration method using 5 cm steps. The swimming routines use tables prepared from the magnetic field map which contain the value of the components of the magnetic field, B_x, B_y and B_z, in (x, y) planes at prescribed z positions along the detector.

In dealing with real data events we first swim tracks from the second to the third drift chamber by using the track's position, direction cosines and momentum as calculated by the L3 filter. The momentum is then adjusted by comparing the swum track position with the measured hit in chamber three and forcing the particle to go through that hit. In this fashion the particle's trajectory will match more precisely with the hits in the various detectors. This adjustment is necessary due to the fact that the L3 filter uses $\int B_y(y)dz$ tables (Sec. 4.3) which only approximate the actual field seen by the traversing particle. Tracks are then transported downstream all the way through the spectrometer to the lead glass array. Track positions and direction cosines are stored in common blocks at various planes in z ("apertures") that correspond to defined positions relative to the different detectors. This allows us to associate hits in every detector element with each track.

5.2 Offline Passes

In order to reduce the 1371 raw data tapes to a more manageable number on which a more accurate analysis can be performed, they were run through three different offline jobs, or "passes", with progressively tighter cuts. By allowing a reduced number of apertures in the swimming through the magnetic field (Sec. 5.1), in the first two passes, we were able to speed up the jobs considerably. The rather loose cuts applied guarantee that the less precise swimming did not compromise the analysis.

The first pass, with a reduction factor of approximately 28, yielded 49 tapes. Events that had the $ee\gamma$ or the MB Level 1 trigger bit set (Sec 4.1) were selected. Each of the two charged tracks was required to have associated hits in the trigger scintillation counters (TSC) consistent with having satisfied the Level 1 trigger. We required that the product of the number of vertical TSC counters hit in the upstream and downstream modules be at least 2. We also demanded that the sum of the upstream and downstream horizontal counters hit be greater than 0. A hit had to be within a 20 ns time window. In reconstructing events, we adopted version A of our cluster finding algorithm (Sec. 5.3). Version B was only used in the final stages of the analysis. The event was rejected if there was not at least one pair of photons, one on each side of the spectrometer, consistent with a π^0 (Sec. 5.4). For each π^0 combination in each event, different mass hypotheses, corresponding to $K_L^0 \to \pi^0 e^+ e^-$ or $K_L^0 \to \pi^+ \pi^- \pi^0$, were tried. We required that the $\chi^2_{\pi^0}$ be less than 30., that the colinearity, Θ_c, be less than 0.015 radians and that the reconstructed mass, $m_{\pi^0 e^+ e^-}$, lie in the range of 0.450 to 0.550 GeV. If any of the hypotheses passed these cuts, for any combination, the event was kept. Table 5.1 summarizes the cuts applied in this pass.

The purpose of the second pass, which also used the fast swimming, was to apply particle identification requirements to electron candidates to help reduce charged pion contamination (Ch. 7), and to separate events from which we would obtain our $K_L^0 \to \pi^0 e^+ e^-$ candidates and our $K_L^0 \to \pi^+ \pi^- \pi^0$ normalization signal. We produced only 4 tapes of each type. Events that were consistent with both hypotheses were written out to both streams. The 49 tapes from the first pass also contained events that, up to that point, were consistent with $K_L^0 \to \pi^0 \mu^+ \mu^-$ and $K_L^0 \to e^+ e^- \gamma$ decays. The fate of those events will not be discussed in here. Events with the MB Level 1 bit set did not need to satisfy any particle identification cuts, and were written out directly to the $K_L^0 \to \pi^+ \pi^- \pi^0$ stream for further analysis. On events with the $ee\gamma$ Level 1 bit set, the charged tracks were required to have a ratio of energy (as measured by the lead glass) to spectrometer momentum (E/p) greater than 0.70 and the ratio of energy deposited in the lead glass converter blocks to the total lead glass energy (E_C/E) needed to be greater than 0.04. These events were written out to the $K_L^0 \to \pi^0 e^+ e^-$ stream tapes. We accumulated about 193,000 such events, and about 284,000 in the $K_L^0 \to \pi^+ \pi^- \pi^0$ tapes. Table 5.2 lists the cuts applied in the second pass.

In the third pass we used the standard, more precise, swimming. The requirement of consistent hits for tracks on the TSC, defined above, was re-applied. We adopted tighter particle identification type cuts on lead glass measurements for electrons on $K_L^0 \to \pi^0 e^+ e^-$ candidates: $0.75 \leq E/p \leq 1.50$, $E_C/E \geq 0.05$ and $D_{BB}^2 \leq 0.01$ m^2, were D_{BB} is the distance between the position of the projected track in the back blocks to the position of the centroid of the cluster associated with that track (Sec. 5.3). In addition, the Čerenkov counter was required to have signals consistent with a "good" electron. See Chapter 7 for a thorough description of these cuts and their efficiency. On both $K_L^0 \to \pi^0 e^+ e^-$ and $K_L^0 \to \pi^+ \pi^- \pi^0$ tighter Θ_c^2, $\chi_{\pi^0}^2$, and timing cuts were applied. Times for both tracks and photons were given by the "finger" counters array, or FNG, (see Sec. 5.3). The two track times, and those of the two photons in each π^0 combination, had to be within 5 ns of each other. Finally, events passed if any π^0 combination had $\chi_{\pi^0}^2 \leq 15.$ and $\Theta_c^2 \leq 50$ μsr. As a result of these cuts, we obtained 25,262 $K_L^0 \to \pi^+ \pi^- \pi^0$ and 5,121 $K_L^0 \to \pi^0 e^+ e^-$ candidates. Table 5.3 outlines the cuts applied in this third pass.

5.3 Cluster Finding Algorithm

The lead glass array (Fig. 3.3) is used as an electromagnetic calorimeter (Sec. 3.3) allowing us to identify electrons and photons by searching for clusters of energy produced by the showering particles. The algorithm works identically on the left and right sides of the detector. It starts by identifying a hit converter block and a hit back block from the projected positions of the tracks in these counters. Then the energies of the hit block and of a group of neighbouring blocks are summed up. After the track clusters are identified, the algorithm then searches for extra clusters of energy which, if certain conditions are satisfied, will become photon candidates. Two different versions, described below (with somewhat different criteria for incorporating converter blocks into a cluster), were used. Version A was applied in the first three offline passes, while version B was adopted for the final analysis stages.

Let us examine first the cluster definition for electromagnetic showers associated with tracks. For back blocks an array of 3×3 blocks, with the hit block in its center, is considered a cluster (Fig. 5.1): 9 blocks in total (except when the hit block is near the edge of the detector). In the converter up to 6 blocks can be part of the track cluster, depending on where the projected track position is. Figure 5.2 shows three cases were the projected track position in a converter block is below beam center (y=0). In version A of the algorithm, used in the two fast offline passes, if the y position of the hit is below a strip 20 cm wide from the top edge of that block, then only one block to the left and one to the right are considered part of the cluster (the top converter blocks would be too far from the hit position for them to be included). If, on the other hand, the hit is less than 20 cm below the beam center line then the converter block on top of the hit one and the ones to the left and right of it are included in the cluster , a total of 6 blocks. The above procedure is applied similarly when the projected track hits one of the top converter blocks. If the track hits a converter block on the edge of the array then the cluster will have 2 or 4 blocks depending on the hit position with respect to beam center line. The total lead glass energy associated with the track is then the sum of the converter cluster energy and the back blocks cluster energy: $E = E_C + E_{BB}$. In version B (Fig. 5.3), used in the rest of the analysis following the second fast pass, the 20 cm wide strip was reduced to 4 cm. Showers should be well contained within this radius in the 3.3 radiation lengths of the converter (the "Molière" radius[29] is approximately 4 cm). Also, a converter block adjacent to the hit block will be part of the cluster only if the projected track is at least 4 cm from its edge. The cluster energy centroid $(\bar{X}^{BB}, \bar{Y}^{BB})$ is calculated from the back blocks (for photons and tracks alike) by:

$$\bar{X}^{BB} = \frac{\sum_i x_i{}^{BB} E_i{}^{BB}}{\sum_i E_i{}^{BB}} \quad \text{and} \quad \bar{Y}^{BB} = \frac{\sum_i y_i{}^{BB} E_i{}^{BB}}{\sum_i E_i{}^{BB}} \tag{5.1}$$

Where (x_i, y_i) is the center of block "i", E_i its energy, and the sum extends over all back blocks in the cluster. The position resolution of these centroids is obtained by studying well identified electrons from K_{e3} decays and found to be approximately 5 cm.

The method adopted in searching for photon clusters proceeds as follows. All back blocks with non zero energy are sorted out, from largest to smallest energy. We then search for "principal blocks", or blocks which would have the largest energy in each of the photon clusters, by looping over the sorted array and requiring that each principal block has a minimum of 200 MeV energy deposited and that its center is at least 20 cm away from the projected position of the track on the same side of the detector. This serves the purpose of isolating, to some extent, the photons from the charged tracks. A principal block must also have good timing. Using the center position of the block, the matching counters in the "finger" scintillation counters (Sec. 3.3), which give the best timing in the lead glass array, are located and inspected, and a rather loose time cut is applied.

The matching horizontal finger counter, two counters above and two below are considered, as well as the matching vertical counter and two neighbours to its right and to its left. In x (vertical) and in y (horizontal), separately, the times of these counters are averaged and the difference of these averages is taken. The separate time averages must be within a 40 ns time window while the difference must be within a 30 ns window. Once a principal back block is identified, a 3×3 block array, just as for tracks (Fig. 5.1), is the back block cluster for that photon. In version A of the algorithm, 6 converter blocks were automatically considered part of the cluster. Figure 5.4 shows the converter blocks cluster that correspond to the principal back block. If there are no hits in the corresponding converter blocks, the cluster is not considered a photon candidate. The photon cluster total energy, converter plus back blocks, has to exceed 400 MeV. This helps reduce background from accidental minimum ionizing tracks (muons and charged pions) which will deposit between 300 and 400 MeV in the lead glass array.

The final criterion for the cluster to be a photon candidate is that it be well separated from previously found photon candidates. New photon candidate centroids must be at least 20 cm away from the centroids of all previously identified photon clusters. Otherwise, they are discarded since these blocks are most likely to already be part of another cluster. In version B of the algorithm the criterion by which neighbouring converter blocks become part of a cluster was changed. In this version (Fig. 5.5), if the principal back block is low (high) enough in y, then only the bottom (top) 3 converters are part of the cluster. The actual requirement is that the distance in y from the bottom of the back block to the top of the top converters and to the bottom of the bottom converters be less than 1.10 meters in order for that converter to become part of the cluster.

The final stage of the cluster finding algorithm is performed in the finger scintillating counter array. Once the energies and positions of photon clusters are measured in the lead glass converter and back blocks, the associated hits in the finger counter modules are analyzed. These signals contain timing and pulse height information. The photon's centroid in the back blocks projects onto one vertical and one horizontal FNG counter. In addition to these counters, $\pm$ 2 vertical counters and $\pm$ 2 horizontal counters are also examined. The times from the top and bottom tubes of the vertical counters are averaged with the times of the horizontal counters to obtain a cluster time. This procedure is applied also to the track associated clusters to yield precise track timing (about 1 ns resolution). In the case when the x (y) positions of the photon cluster and of the projected track are within 30 cm, or less, of each other, the times of the vertical (horizontal) counters will be ambiguous. The cluster time, for the track and for the photon, is then re-defined to be only the average of the horizontal (vertical) counters' times.

Due to the finer segmentation of these counters a better position resolution for photons, about 1.4 cm, is achieved. This is to be compared to about 5 cm resolution of the given by the lead glass. Using the pulse height information the FNG pulse height centroid, $(\bar{X}^{\mathrm{FNG}}, \bar{Y}^{\mathrm{FNG}})$, is calculated by:

$$\bar{X}^{\mathrm{FNG}} = \frac{\sum_i x_i{}^{\mathrm{FNG}} PH_i{}^{\mathrm{FNG}}}{\sum_i PH_i{}^{\mathrm{FNG}}} \quad \text{and} \quad \bar{Y}^{\mathrm{FNG}} = \frac{\sum_j y_j{}^{\mathrm{FNG}} PH_j{}^{\mathrm{FNG}}}{\sum_j PH_j{}^{\mathrm{FNG}}}, \tag{5.2}$$

where $x_i(y_j)$ is the x (y) position of the middle of the vertical (horizontal) counter "i" ("j"), and $PH_i(PH_j)$ its pulse height.

Summarizing, from the cluster finding algorithm we obtained energy and position measurements for tracks and photons in the lead glass, and timing and position measurements in the finger counters. These quantities are used for particle identification purposes (Ch. 7) and in the final event reconstruction (Sec. 5.4).

5.4 Event Reconstruction

In this section the final analysis criteria used in reconstructing $K_L^0 \to \pi^0 e^+ e^-$ and $K_L^0 \to \pi^+\pi^-\pi^0$ decays are described. Due to the large amount of background for $K_L^0 \to \pi^0 e^+ e^-$ further restrictions on tracks and photons had to be implemented.

The particle identification requirements were made stricter by demanding that electrons tracks have $E_C/E \geq 0.055$ and $0.75 \leq E/p \leq 1.25$. We used the finger counters to aid in the pion rejection task by applying cuts on the track's first and second moments (Ch. 7). Namely, we demanded that the distance in x (and in y) between the track position and the FNG track centroid be less than 4 cm, and that the width of the FNG cluster be such that at least 2 vertical counters and two horizontal counters are hit and in time.

In order to reject accidental backgrounds, tight timing requirements for the four different particles are imperative. Table 5.4 summarizes the timing cuts we adopted. Constraints were made on the relative time of the two tracks and the two photons, on the average of the track times and on the average of the photon times. In addition, both photons needed to be in time with the tracks time average and, finally, the difference and the average, of the earliest and latest times of all four particles were also constrained to be within a given time window.

The next step is reconstructing π^0's from all the different pairs of photon candidates. Only combinations with one photon on each side side of the detector are considered. Track/photon separation conditions, in addition to those used within the cluster finding algorithm (Sec. 5.3), had to be applied. We took advantage of the better position resolution of the finger counters to require that the distance from the photon FNG centroid to the track position be greater than 20 cm. Also, due to the coarse segmentation of the converter blocks, we demanded that if both the track and the photon hit the top or the bottom half of the converters, their distance in x should be at least 10 cm. This ensures that in this cases, the track and the photon will be isolated by at least the width of one converter block, and helps measure more accurately the separated track and photon converter energies.

In order to be sure that the identified photons originated at the track's vertex, we projected a straight line from this vertex through the whole volume of the detector, all the way down to the photon FNG cluster position in the lead glass array. We verified that this trajectory did not cross through any part of the detector with any significant amount of material. Specifically we checked at various z planes that it cleared the magnet apertures, coils and iron shields. It was also required that it cleared the central spout of the vacuum window (although photons were allowed to go in the inside of that spout). The large accidental background near the neutral beam halo tended to give hits in the lead glass back blocks that would simulate photon clusters. Also, due to leakage etc., these blocks were not properly calibrated for energy measurements. Therefore, we were forced to constrain the fiducial area on the back blocks on which photon cluster centroids would be allowed; we ignored π^0 combinations which had a photon in the innermost back block column.

Combining the photon energies and positions measured in the lead glass array (Sec. 5.3), together with the reconstructed track vertex, one obtains the two photon invariant mass: $m_{\gamma\gamma} = (E_{\gamma_1} + E_{\gamma_2})^2 - (\vec{p}_{\gamma_1} + \vec{p}_{\gamma_2})^2$. A chi-squared ($\chi^2_{\pi^0}$) function on these variables, defined below, was then minimized with the constraint that $m_{\gamma\gamma} = m_{\pi^0}$.

$$\chi^2_{\pi^0} = \sum_{i=1}^{2} \frac{(E^{\rm fit}_{\gamma_i} - E_{\gamma_i})^2}{\sigma^2_{E_i}} + \frac{(X^{\rm fit}_{\gamma_i} - X^{\rm FNG}_{\gamma_i})^2}{\sigma^2_{X_i}} + \frac{(Y^{\rm fit}_{\gamma_i} - Y^{\rm FNG}_{\gamma_i})^2}{\sigma^2_{Y_i}} \tag{5.3}$$

E_{γ_i} are the measured photon energies and $(X^{\rm FNG}_{\gamma_i}, Y^{\rm FNG}_{\gamma_i})$ the photon FNG centroids. The σ's are the measurement uncertainties in the corresponding quantities; $\sigma_{E_i}/E_i \approx 1\% + 10\%/\sqrt{E_i}$, $\sigma_X, \sigma_Y \approx 1.5$ cm. $\{E^{\rm fit}_{\gamma_i}, X^{\rm fit}_{\gamma_i}, Y^{\rm fit}_{\gamma_i}\}$ is the set of values at which $\chi^2_{\pi^0}$ attains its minimum. A cut on $\chi^2_{\pi^0} \leq 7.0$, obtained from our $K^0_L \to \pi^+\pi^-\pi^0$ normalization signal, was applied. This cut is equivalent to cutting directly on $m_{\gamma\gamma}$.

Table 5.5 summarizes the final values of all cut parameters used in this analysis. The $K^0_L \to \pi^0 e^+ e^-$ and $K^0_L \to \pi^+\pi^-\pi^0$ candidates that pass these selection criteria are characterized in a scatter plot (Fig. 5.7(a),5.7(b)) of the squared of their colinearity angle, Θ^2_c, vs. their reconstructed invariant mass, $m_{\pi^0 e^+ e^-}$ or $m_{\pi^0 \pi^+ \pi^-}$. The colinearity angle (see Fig. 5.6) is the angle formed by the direction of the reconstructed 3-momentum vector of the event: $\vec{p}_{\pi^0 ee} = \vec{p}_{\pi^0} + \vec{p}_{e^+} + \vec{p}_{e^-}$, and the line connecting the K^0_L decay point, (given by the tracks' vertex), to the target center. When calculating the event invariant mass, we make use of the set of fit values $\{E^{\rm fit}_{\gamma_i}, X^{\rm fit}_{\gamma_i}, Y^{\rm fit}_{\gamma_i}\}$ for the π^0 parameters.

The final sample of reconstructed $K^0_L \to \pi^0 e^+ e^-$ candidates is shown in Figure 5.7(a). We find no events in the region with $0.4827 \le m_{\pi^0 e^+ e^-} \le 0.5127$ and $\Theta^2_c \le 20\mu$sr. We calculate the sensitivity of our search in this region (Ch. 8). Figures 5.7 to 5.9 show the reconstructed Θ^2_c and $m_{\pi^0\pi^+\pi^-}$ distributions. for the final $K^0_L \to \pi^+\pi^-\pi^0$ candidates. The corresponding Monte Carlo distributions are shown in Figures 6.4 and 6.5. In Figures 5.10 to 5.19 various other distributions from this sample are shown.

We count 7,220 $K^0_L \to \pi^+\pi^-\pi^0$ reconstructed events within the signal box. The electronic prescale factor on our minimum bias Level 1 trigger had two different values during the run. 2,178 events are found in the period with a prescale factor of 1000, and the other 5,042 correspond to the period with a prescale factor of 2000. By properly weighting these numbers we conclude that the effective number of observed $K^0_L \to \pi^+\pi^-\pi^0$ events is $N_{\pi^0\pi^+\pi^-} = 12.26 \times 10^6$. The statistical error on this number is 1.5%.

We need two other studies in order to estimate the sensitivity of our $K^0_L \to \pi^0 e^+ e^-$ search (Ch. 8). In Chapter 6, which describes our Monte Carlo technique for event simulation, we calculate the $K^0_L \to \pi^+\pi^-\pi^0$ to $K^0_L \to \pi^0 e^+ e^-$ acceptance ratio, while in Chapter 7, results of the particle identification efficiency study are obtained.

6. EVENT SIMULATION

We have developed a software program which simulates the experiment. K_L^0 decays are generated using a Monte Carlo method described in section 6.1. The decay products (daughters) are then transported through a simulated detector and the simulated responses of the various detector elements to these tracks are digitized and packed in the same format as real data (Sec. 6.2).

These simulated events are extremely important in debugging the various pieces of software used in analysing real data. By comparing Monte Carlo events to real data of a particular kind, the simulation can be perfected and then used to predict various distributions and properties of kinds of events.

In this particular search for $K_L^0 \to \pi^0 e^+ e^-$ we have used the Monte Carlo events to understand the difference in geometrical acceptance between $K_L^0 \to \pi^0 e^+ e^-$ and $K_L^0 \to \pi^+ \pi^- \pi^0$ (Sec. 6.3). In addition, by running our data analysis programs on Monte Carlo generated events we can estimate the different effects of the various cuts on these two classes of decays and therefore be able to estimate the sensitivity of our search (Sec. 8.1).

6.1 Monte Carlo Event Generation

Protons with an energy of 24.0 GeV/c impinging on a copper target will produce neutral kaons with a differential cross section which can be expressed as a function of the production angle, θ, and the magnitude of the kaon momentum, p_K. We choose our production angle to be $\theta = 2.75°$. The K_L^0 momentum spectrum was taken from the measurements of neutral kaon production at proton beam energies of 200 and 300 GeV/c made by Skubic *et al.*[30]. Feynman scaling is used to predict the kaon production flux at the AGS energies.

On a given event, p_K is chosen randomly from the Skubic distribution. The direction of the kaon is obtained by choosing randomly a generation point along the target and a projection point on an (x, y) plane 10 meters downstream of the target. The lifetime of this kaon is, once more, obtained by sampling randomly the K_L^0 exponential lifetime distribution in a way that only kaons decaying in the decay volume in the range of $9.0 < z < 17.8$ m are considered. The K_L^0 mean lifetime is $\tau_{K_L^0} = 5.184 \times 10^{-8}$ sec.

The kaon momentum, $\vec{p}_{K_L}$, and lifetime determine the K_L^0 decay point in the decay volume where the momenta and energies of the decay products are selected in the kaon center of mass. For the three-body decays in consideration here, first the energies of the charged daughters are selected randomly from a flat distribution within the Dalitz envelope. For $K_L^0 \rightarrow \pi^+\pi^-\pi^0$ the actual parameterization of the measured density of the Dalitz envelope[13] is sampled using the method of "hit or miss" Monte Carlo. For $K_L^0 \rightarrow \pi^0 e^+ e^-$ we have assumed a flat distribution in the Dalitz plot. Using conservation of energy and the two charged daughter's energies the energy of the third decay particle is obtained.

The program proceeds to chose randomly, from the flat phase space distribution, two angles: $\cos\theta_1$ and φ_1 for the first charged daughter's direction and the angle δ_{12} between the directions of the two charged decay particles. The last parameter needed to constrain the decay's kinematics is the angle γ between the plane formed by the two charged particle's momentum vectors and the direction of the first charged particle's momentum.

From conservation of momentum the third particle's momentum is completely determined. Using the K_L^0 momentum $\vec{p}_{K_L}$, the decay is boosted by means of a Lorentz transformation from the kaon center of mass into the laboratory frame.

In general, if the decay products are unstable, a lifetime is chosen from their lifetime distribution and at the appropriate point in the spectrometer the particles are forced to decay. This is how the charged pions in $K_L^0 \rightarrow \pi^+\pi^-\pi^0$ are handled when $\pi^\pm \rightarrow \mu^\pm + \nu$ (mean life $\tau_{\pi^\pm} = 2.6030 \times 10^{-8}$ sec). The neutral pion is decayed promptly via $\pi^0 \rightarrow \gamma\gamma$ ($\tau_{\pi^0} = 0.83 \times 10^{-16}$ sec, $c\tau_{\pi^0} = 2.5 \times 10^{-6}$ cm) at the K_L^0 decay point. Therefore, we obtain in the final states of $K_L^0 \rightarrow \pi^0 e^+ e^-$ and $K_L^0 \rightarrow \pi^+\pi^-\pi^0$ two charged particles and two photons with well defined four-momentum vectors ready to be transported (swum) through the various detector elements (Sec. 6.2).

6.2 Detector Simulation

Each track product of the simulated K_L^0 decay is projected through the detector using the magnitude of its momentum and its direction cosines in the lab frame of reference. (The swimming of particles in the magnetic field is described in section 5.1).

Each arm of the detector is simulated as being formed of consecutive rectangular apertures, or planes, having a fixed z position. The apertures bear a close resemblance to the actual cross section presented by the various detectors in the spectrometer, and are, in general slightly larger than the fiducial detector area. The effect of the various detectors on the traversing particles is calculated using a single parameter which characterizes the interaction of charged particles with matter: the radiation length. Table 6.1 lists the apertures used in the simulation together with the radiation length of the aperture itself and that of the material in between apertures.

The projection is performed discretely, one aperture at a time. Particles outside the fiducial area of any aperture will cause that event to be cut. For charged tracks, at each aperture, or in between apertures (at the decay point of unstable particles), the effects of Coulomb multiple scattering[31,32] and bremsstrahlung[33,34] (for electrons only) are computed.

The multiple scattering simulation changes randomly the direction cosines and the x, y coordinates of the scattered particle by sampling a non-Gaussian probability distribution scaled to the Gaussian width:

$$\sigma_{ms} = \frac{.014}{p}\sqrt{N_L}\left[1 + \frac{1}{9}\log_{10}(N_L)\right], \tag{6.1}$$

where N_L is the number of radiation lengths of material, p is the particle's momentum (in GeV) and σ_{ms} is in radians.

The bremsstrahlung simulation uses the following formula, by Tsai[34], for the probability of an electron with initial energy $\mathrm{E_0}$ to end up with an energy in the range [E,E+dE] after traversing N_L radiation lengths of material (by emitting one or more photons):

$$P(\mathrm{E_0}, \mathrm{E}, \mathrm{N}_L) = \left(\frac{\mathrm{E_0} - \mathrm{E}}{\mathrm{E_0}}\right)^{\mathrm{bN}_L} \frac{\rho(\mathrm{E_0}, \mathrm{E_0} - \mathrm{E})\mathrm{N}_L}{\Gamma(1 + \mathrm{bN}_L)} \tag{6.2}$$

$\rho(\mathrm{E}, \mathrm{k})$ is the bremsstrahlung distribution function :

$$\rho(\mathrm{E}, \mathrm{k}) = \frac{1}{\mathrm{k}}\left[\frac{4}{3} - \frac{4}{3}\frac{\mathrm{k}}{\mathrm{E}} + \left(\frac{\mathrm{k}}{\mathrm{E}}\right)^2\right], \tag{6.3}$$

and b is given by:

$$\mathrm{b} = \mathrm{lim}_{\mathrm{k}\to 0}\ \ \mathrm{k}\rho\ \ \left(= \frac{4}{3}\right) \tag{6.4}$$

The x, y positions of the tracks resulting from these projections, at the various detectors, are stored and used to simulate the response of the detector to the specific particle going through it. The drift chamber positions are smeared by a gaussian distribution with an rms of 150 μm, corresponding approximately to the real resolution. The Čerenkov counter will digitize simulated hits for electrons (properly smearing the number of photoelectrons produced). It will also generate signals for pions and muons above threshold. The response of the lead glass array is simulated by using prescribed gaussian profiles for the showering particles, using different parameters for the converter and back blocks. The energy fraction deposited in the converter is fixed to be 1/3 of the total energy. The energy in each lead glass block is then smeared randomly from a gaussian distribution with a σ_{E} given by:

$$\frac{\sigma_{\mathrm{E}}}{\mathrm{E}} = \mathrm{A} + \frac{\mathrm{B}}{\sqrt{\mathrm{E}}}, \tag{6.5}$$

where we chose $\mathrm{A} = 0.03$ and $\mathrm{B} = 0.09$ for all converter and all slow back blocks, and $\mathrm{B} = 0.22$ for fast back blocks (Sec. 3.2).

The finger counters were simulated at a higher level by simply smearing the particle's position by the actual resolution of the detector, 1.5 cm. At this stage, photons, were required, when projected from their creation point to the z position of the lead glass array, to hit the fiducial area of the lead glass.

6.3 Acceptance Ratio: $A_{\pi^0\pi^+\pi^-}/A_{\pi^0e^+e^-}$

Knowledge of this ratio is necessary in order to estimate the sensitivity of our null search for $K_L^0 \to \pi^0 e^+ e^-$ (Sec. 8.1). Due to the low detector acceptance, we selected large samples of digitized Monte Carlo events that passed the geometrical cuts imposed by the detector simulation in terms of apertures (Sec. 6.2). For $K_L^0 \to \pi^+\pi^-\pi^0$ events, charged pions were allowed to decay normally in the spectrometer.

These Monte Carlo events were, in most respects, treated like real data when run through the same offline analysis program used in studying our data (Ch. 5). However, there were some differences in the method used in track reconstruction, and in the fact that a timing simulation was not used for Monte Carlo events. All events were, by definition, "in time". In addition, no electron identification cuts were implemented directly. Instead a study of the efficiency of our particle identification cuts was performed on semileptonic decays (Ch. 7). These efficiencies were parameterized in the relevant variables (momentum, position, etc.) and the distributions of Monte Carlo electrons that pass all other cuts were then re-weighted according to these efficiencies (Sec. 7.2,7.3).

Track reconstruction for real data was performed online by the Level 3 filter (Sec. 4.3). In reconstructing tracks for Monte Carlo events, we used a Pattern Recognition program[35]. The digitized hits at the two upstream-most drift chambers are connected by a straight line which is projected to the center of the first magnet (48D48). Another line is drawn connecting the hits in the fourth and fifth drift chambers and the line projected upstream to the center of the second magnet (96D40). A line is drawn connecting the two projected points at the center of the two magnets and if this line comes close to the hit in the third drift chamber (in between the magnets) then a track is formed. The momentum of the track is found from a $\int B_y(y)dz$ table. This method is used on both the x and the y views, for all the appropriate hit combinations.

The two tracks found are required, when projected back to the decay volume to have a reasonable distance of closest approach. Since this procedure takes into account inefficiencies, smearing and noise on the drift chambers, the reconstructed tracks will bear a close resemblance to real tracks. In addition, since only particles that register hits in the chambers can form tracks, this procedure applies an effective fiducial cut on Monte Carlo events. This makes up for the fact that the chamber apertures (Table 6.1) used in the swimming stage were larger than the real fiducial area of the chambers.

The reconstructed Monte Carlo tracks are then projected to the downstream detectors, using the track position and direction cosines at the fifth drift chamber. We required that an appropriate TSC digitized hit pattern can be associated with the track position in the counters. (These assured that the tracks would satisfy the same Level 1 trigger conditions as real data). As mentioned above, all other cuts, except timing and particle identification, applied to the data were also applied to Monte Carlo events (see Table 5.5).

The geometrical acceptance of $K_L^0 \to \pi^0 X^+ X^-$ depends significantly on the mass of X, m_X. Figure 6.1 shows the acceptance of the detector as a function of m_X, for a mass range from zero (electrons) to 140 Mev (charged pions), for a flat Dalitz plot distribution. Only the last point shows the $K_L^0 \to \pi^+\pi^-\pi^0$ acceptance using the appropriate Dalitz density. Only the relative acceptances are relevant since their value depends on the chosen momentum and z decay position ranges for the kaons.

For calculating the acceptance ratio of $K_L^0 \to \pi^+\pi^-\pi^0$ to $K_L^0 \to \pi^0 e^+ e^-$, we generated 8,923,121 $K_L^0 \to \pi^+\pi^-\pi^0$ and 12,136,519 $K_L^0 \to \pi^0 e^+ e^-$ Monte Carlo events. Kaons decayed between 9.0 and 17.8 m in the decay volume. Their momenta was chosen to be in the range of 3 to 20 Gev. Only 21,243 $K_L^0 \to \pi^+\pi^-\pi^0$ and 5,768 $K_L^0 \to \pi^0 e^+ e^-$ survived the geometrical and pattern recognition cuts. The geometrical acceptance ratio of $K_L^0 \to \pi^+\pi^-\pi^0$ to $K_L^0 \to \pi^0 e^+ e^-$ events is therefore 5.21. These events were then run through the data analysis program.

The number of $K_L^0 \rightarrow \pi^+\pi^-\pi^0$ events that remained in the signal region (see Ch. 5) after the analysis cuts was 4,726, while only 974 $K_L^0 \rightarrow \pi^0 e^+ e^-$ survived. The resulting acceptances and errors are shown in Table 6.2. We obtain that the total acceptance ratio is:

$$A_{\pi^0\pi^+\pi^-}/A_{\pi^0 e^+ e^-} = 6.60 \pm 3.5\%. \tag{6.6}$$

The resulting distributions in mass and colinearity squared for these samples of $K_L^0 \rightarrow \pi^0 e^+ e^-$ and $K_L^0 \rightarrow \pi^+\pi^-\pi^0$ Monte Carlo events are shown in Figures 6.4 and 6.5. Figures 6.2 and 6.3 show a comparison between the data and the Monte Carlo $K_L^0 \rightarrow \pi^+\pi^-\pi^0$ distributions for the vertex z position and for the K_L^0 momentum. In figures 6.6 to 6.9 we show other interesting Monte Carlo distributions for $K_L^0 \rightarrow \pi^0 e^+ e^-$.

7. PARTICLE IDENTIFICATION FOR $K_L^0 \to \pi^0 e^+ e^-$

In this chapter I describe the studies performed in estimating the efficiency of the particle identification criteria used in selecting electrons in our $K_L^0 \to \pi^0 e^+ e^-$ search. Due to the large amount of background, it was necessary to apply stringent electron identification cuts in order to improve rejection of charged pions from K_{e3} decays. These cuts had to be tighter than those applied in the two body analysis, where the constraint that the two body invariant mass reconstructs to the K_L^0 mass can be applied. In that case, cuts on the Čerenkov counter and in the lead glass blocks proved to be sufficient in rejecting undesired background. In our case, we had not only to make tighter cuts on the lead glass, but also to implement new cuts provided by the "finger" counter hodoscope.

As described in detail below, the electron efficiencies for $K_L^0 \to \pi^0 e^+ e^-$ are obtained by estimating efficiencies for electrons from K_{e3} decays as a function of the electron's momenta and position, and then folding in the corresponding $K_L^0 \to \pi^0 e^+ e^-$ momenta and position spectra for Monte Carlo generated events.

7.1 Electron Efficiencies in the Lead Glass Array

Listed in Table 7.1 are the final lead glass/finger counters selection cuts used. In the lead glass blocks, three cuts are implemented: E/p is the ratio of total lead glass energy to spectrometer momentum, E_C/E is the ratio of converter energy to total lead glass energy, and D^2_{BB} is the square of the distance from the position of the projected track in the lead glass back blocks to the centroid of the cluster associated with that track. Electrons penetrating the lead glass converter blocks (3.3 radiation lengths) start an electromagnetic shower, depositing a significant fraction of their energy. As the shower propagates to the back blocks all the energy will be absorbed in the remaining 10.5 radiation lengths of lead glass. Therefore, for electrons, E/p should be approximately unity, and E_C/E larger than some small (about 0.05) value. Charged pions, on other hand, will deposit only a fraction of their energy in the array, resulting in smaller E/p. Also, if they shower, they do at a deeper depth in the converter thus resulting in a smaller E_C/E. In addition, the abundance of particles in the electron shower allows a more precise estimate of the cluster's energy centroid. Therefore, electron clusters' centroids tend to be closely associated with the actual track position. This is not the case with charged pion cluster centroids which deviate much more from the pion position. Similarly the "1st moment" of a track cluster in the finger counters is defined to be the distance between the actual track hit and the pulse height centroid of the cluster. We used the x and y distances separately. The better position resolution of the finger counters allows us to make a more precise electron-pion separation based on this quantity. The last lead glass array cut is the equivalent of the shower profile as measured in the finger counters ("2nd moment"). Electrons produce wider showers than charged pions. By counting the number of vertical and horizontal finger counters in these showers we can further separate pions from electrons.

Figures 7.1 to 7.13 illustrate the above statements on electron-pion separation. We chose to show the correlations of the various cut variables with the more common E/p variable. Figures 7.1(a) to 7.6(a) are scatter plots for electrons of all cut variables in Table 7.1. Figures 7.1(b) to 7.6(b) show the same plots for charged pions. Figures 7.7 to 7.13, (a) and (b), are the corresponding one dimensional histograms for each of these variables. The lines on the plots show the value of the variables for which the various cuts were applied.

Our sample of electrons was obtained by identifying K_{e3} decays in the following way. (The selection criteria for charged pions is described in Sec. 7.3). Two track events from our minimum bias data were selected. In order to be consistent with what we did in the 3-body analysis, we use the track parameters as defined by the level 3 trigger.

For a track to be considered an electron, it must have a positive electron identification as given by the time and pulse height signals from the Čerenkov counter (see Sec. 7.2). The other track, in order to be a charged pion, is vetoed on the lead glass, on the Čerenkov counter and on the muon hodoscope. The lead glass veto is implemented by demanding that $E/p \leq 0.50$. We also require that both the pulse height and the time in the Čerenkov counter be inconsistent with the particle being an electron (Sec. 7.2). The muon veto calls for the track to have a 99% probability of not being a muon[36] together with a muon range requirement that the $|$ last gap - expected gap$| > -4$ gaps[37].

Our electron efficiencies using this selection showed a steep decrease for particles above 6 GeV. This effect was enhanced in the fast block distributions due to the fact that large momentum particles will be more likely to hit these inner blocks. The Čerenkov muon threshold is about 6 GeV. By applying the muon veto mentioned above on the electron tracks this sharp decrease in efficiency at high momentum becomes less striking. The overall efficiencies increase by about 1%. We decide to keep the muon veto on the electron side and to assume that the 1% increase in efficiency would be solely due to the reduction of muon contamination when implementing the veto.

The selected particles were binned according to their momenta and to their position in the lead glass back blocks. We selected a total of ten momentum bins in the range of 0 to 10 Gev, and four position bins: left fast, left slow, right fast and right slow. See Tables 7.2 and 7.3. We estimated the efficiencies in each of these bins when applying all 32 (2^5) possible combinations of cuts.

Table 7.4 lists the total efficiency for each combination of cuts for K_{e3} electrons obtained by integrating over the momentum and position bins. These results are plotted in Fig. 7.14. The five entries, starting with the second one, are the efficiencies when applying each cut separately. The E/p, and the finger moments are the most inefficient ones, followed by the E_C/E cut.

In Fig. 7.15(a) to 7.15(d), the electron efficiencies, for each position bin, as a function of five different cut combinations are depicted. The first bin in the histogram corresponds to applying cut # 1, the second corresponds to cuts 1 and 2 and so on in sequence; the fifth corresponds to applying all cuts 1 to 5. The fast blocks are about 10% less efficient than the slow ones, while the right side seems to be about 3% more efficient than the left side.

Another interesting result is the momentum dependence of the efficiency of these cuts. In Fig. 7.16(a) to 7.16(d) these efficiencies, and their errors, are plotted as a function of momentum for the case when all cuts are applied. We show the efficiencies up to 7 GeV in momentum, which is the relevant range for $K_L^0 \rightarrow \pi^0 e^+ e^-$ (Fig. 6.7). Higher momentum bins have very few statistics, especially for the slow blocks. In general we observe lower efficiencies at low momenta. The same is evident when looking at the momentum dependence of the individual cuts. This is expected from low energy electrons, since there will be little statistics (fewer number of particles), in the electromagnetic shower. In any case, the most relevant momentum bins for estimating K_{e3} electron efficiencies, are the most populated ones; bins 2 to 5.

A correction to these efficiencies is necessary due to the small amount of charged pion contamination in the selected electron sample when calculating the efficiencies for the PBG/FNG cuts. This contamination can be readily seen in the E_C/E vs. E/p scatter plot (Fig. 7.1), where the small cluster of points running along the ordinate resembles the characteristics of the analogous distribution for pions (Fig. 7.2).

From the E/p electron distribution (Fig. 7.7) we estimated, by subtracting a monotonically decreasing distribution at low E/p values from the actual distribution, approximately a 2.5% contamination. Thus, assuming a constant contamination across all bins, the efficiencies in Table 7.4 are underestimated by about 2.5%.

7.2 Electron Efficiencies in the Čerenkov Counter

The condition for selecting electrons in the Čerenkov counter in the $K_L^0 \rightarrow \pi^0 e^+ e^-$ analysis encompasses requirements on the time and pulse height signals of the PMT's illuminated by the track's Čerenkov light. Candidate hit PMT's are selected by knowing the direction of the projected track into the counter and the Čerenkov cone (assuming $\beta = 1$). At least one of the PMT's must satisfy the following conditions obtained from distributions of well-identified electrons. The (pulse-height corrected) time should be within a 5 ns window centered at $t = 0$. In addition, the ratio of the observed number of photo-electrons to the predicted number of photo-electrons associated with the track (obtained from a Monte Carlo simulation of the fraction of light seen by each PMT) should be larger than 0.1. If only the timing requirement is satisfied then a "possible" electron is found, but not a "good" one.

Once more, in order to study the efficiency of this cut, electrons from K_{e3} decays are selected. In this case the electron candidate is identified positively in the lead glass array if $E/p > 0.80$, $E_C/E > 0.45$ and $E_C > 0.2$. The opposite track is vetoed in the Čerenkov counter by requiring that none of the positive electron identification criteria on time and pulse height mentioned above are satisfied. A muon hodoscope veto is also applied on the pion by demanding that the muon confidence level on the time and space probabilities be zero.

In addition the invariant mass of these two tracks is calculated assuming that both are charged pions ($m_{\pi\pi}$). In order to make sure that our sample of K_{e3} decays has no contamination from $K_L^0 \rightarrow \pi^+\pi^-\pi^0$ or $K_L^0 \rightarrow \pi^+\pi^-$ decays, we demand that 0.375 GeV $< m_{\pi\pi} <$ 0.485 GeV.

The efficiency of the Čerenkov cut on "good" electrons for a given mirror is very different for inbend and outbend events.

Table 7.5 shows these efficiencies and their errors, also plotted in Fig. 7.17(a) and 7.17(b), for all 16 Čerenkov cells. Midway during the run the mirror's alignment was changed in order to optimize these efficiencies for the $K_L^0 \to \mu e$ search. The results in Table 7.5 are obtained from minimum bias data over the extent of the run and thus have the proper weight for each of the different alignment periods.

7.3 Combined Efficiency

The purpose of this study is to evaluate the efficiency of the electron selection cuts applied in the $K_L^0 \to \pi^0 e^+ e^-$ analysis. In order to do so, we selected $K_L^0 \to \pi^0 e^+ e^-$ Monte Carlo events that pass all other cuts in the analysis, except particle identification. These cuts are grouped in two, the PBG/FNG cuts (described in Sec. 7.1) and the Čerenkov cuts (described in Sec. 7.2).

In a given event, each electron is first identified by its momentum and its position in the lead glass array. This would correspond to one out of the 40 (10 momenta $\times$ 4 position) possible bins whose efficiencies are given in Fig. 7.16. Assume the efficiency for this bin is ε. A random number between 0. and 1. is generated. If its less or equal to ε, that electron is accepted, otherwise the event is killed. An event is accepted only if both electrons pass this PBG/FNG "cut". It is found that only $52.1 \pm 1.5\%$ of the events will survive these cuts. The error is statistical.

Events that pass the PBG/FNG "cut" are classified as inbends or outbends. In addition, the electrons are projected into the corresponding Čerenkov mirror. Then, for each electron, the corresponding efficiency for that mirror is compared against another random number, in the same way as described above. Again, only events with both electrons satisfying this cut are counted. This comprises $85.3 \pm 1.5\%$ of the events that had already passed the PBG/FNG cuts. If this cut were to be applied independently of the PBG/FNG one, its efficiency would be $84.3 \pm 1.5\%$. The total efficiency, when these particle identification criteria are applied one after the other is $44.4 \pm 1.5\%$.

When calculating the PBG/FNG efficiencies, we observed changes of the order of 1 to 1.5% owing to the different criteria in selecting electrons from K_{e3} decays. Differences of the order of about 2% are observed in the Čerenkov efficiencies when the binning is done in the direction cosines and x, y positions. In addition, by varying each Čerenkov and PBG/FNG bin efficiency, simultaneously for all bins, by ± 1 sigma, the total combined efficiency varied $\pm 2.5\%$. This should be an overestimate of the actual variation. From all this, a reasonable estimate on the systematic error on the combined efficiency is 2.5%.

The results on these efficiency studies are summarized on Table 7.7.

7.4 Charged Pions Rejection

We attempted to study the rejection of charged pions from an electron sample when using the PBG/FNG electron identification cuts listed in Table 7.1. Our sample of pions was obtained from K_{e3} decays in the minimum bias data (Sec. 7.1), and was binned in momentum and position in the same fashion as the electrons in the study described in Sec 7.1. For a track to be a pion, it is required that it not be a "possible" electron as given by the Čerenkov counter signals. (see Sec. 7.2). We veto it on the muon hodoscope, by requiring that the position and timing of the track don't match the known muon distributions. In addition, we demand that the opposite track satisfies all the PBG/FNG electron identification cuts listed in Table 7.1.

As mentioned above, Fig. 7.1(b) to 7.13(b) show scatter plots and histograms of all PBG/FNG electron identification variables for the pion sample resulting from this selection. Figures 7.18(a) to 7.18(d) plot the percentage of charged pions that pass the PBG/FNG cuts for the different (left,right and fast,slow) areas of the lead glass. The first entry is when only cut # 1 is applied, the second with cuts 1 and 2, and so on; the fifth entry has all five cuts applied. In Table 7.6 we list the percentage of pions that survive the application of all the different cut combinations, averaged over momentum and position. We observe that, when all cuts are implemented, only $0.62 \pm 0.04\%$ of the charged pions survive, about 1 in 160. Therefore the charged pion rejection probability when applying the PBG/FNG cuts is $0.9938 \pm 0.0004\%$. This is only a lower bound on the rejection due to the fact that a small electron contamination, possibly of about 0.5%, in the charged pion sample is to be expected.

It is found[38] that the Čerenkov criteria for electron identification will reject about $99.20 \pm 0.06\%$ of selected pions. Therefore a lower bound (allowing for electron contamination in the sample) on charged pion rejection probability Čerenkov counter is about 0.9920. These pion rejection results are summarized in Table 7.8. Combining these separated probabilities for the PBG/FNG and Čerenkov cuts into a total rejection factor would require some more studies.

8. RESULTS

In the previous chapters (5 to 7) I have described the various studies performed in our search for $K_L^0 \to \pi^0 e^+ e^-$. No candidates were found. In this chapter I explain how the results of these studies combine into one number, which is the sensitivity of our search. The error in the estimate of the sensitivity is also discussed.

8.1 Sensitivity Estimate for $K_L^0 \to \pi^0 e^+ e^-$

By knowing the number of observed $K_L^0 \to \pi^+ \pi^- \pi^0$ events, and by folding in the various effects by which the the $K_L^0 \to \pi^0 e^+ e^-$ search differs from $K_L^0 \to \pi^+ \pi^- \pi^0$, we can calculate the sensitivity of this search.

Dividing the $B(K_L^0 \to \pi^+ \pi^- \pi^0)$ branching ratio[13] by the effective number of observed $K_L^0 \to \pi^+ \pi^- \pi^0$ events, $N_{\pi^0 \pi^+ \pi^-}$ (Sec. 5.4), yields the single event sensitivity for $K_L^0 \to \pi^+ \pi^- \pi^0$.

$$\frac{B(K_L^0 \to \pi^+ \pi^- \pi^0)}{N_{\pi^0 \pi^+ \pi^-}} = \frac{0.1239}{12.26 \times 10^6} = 1.01 \times 10^{-8}$$

Since no $K_L^0 \to \pi^0 e^+ e^-$ events were observed, the 90% confidence limit on the branching ratio is given by:

$$B(K_L^0 \to \pi^0 e^+ e^-) \ < \ 2.3 \times \frac{B(K_L^0 \to \pi^+\pi^-\pi^0)}{N_{\pi^0\pi^+\pi^-}} \times \frac{A_{\pi^0\pi^+\pi^-}}{A_{\pi^0 e^+ e^-}} \times \frac{f_\pi}{\epsilon_{\rm L1} \cdot \epsilon_{\rm L3} \cdot \epsilon_{\rm ID}} \quad (8.1)$$

$A_{\pi^0 e^+ e^-}$ and $A_{\pi^0\pi^+\pi^-}$ are the acceptances for $K_L^0 \to \pi^+\pi^-\pi^0$ and $K_L^0 \to \pi^0 e^+ e^-$, respectively, obtained from our Monte Carlo simulation. The efficiency of the Level 1 trigger is given by $\epsilon_{\rm L1}$. This combines the electronic bit efficiency and the efficiency of the photon condition (Sec. 4.4). $\epsilon_{\rm L3}$ is the efficiency of our Level 3 online filter combined with the 15% loss of events due to the improper handling of events with two-tack colinearities less than 20 mrad, (see Sec. 4.4). The efficiency of the electron identification cuts is $\epsilon_{\rm ID}$ (Ch. 7).

f_π represents a correction factor to the observed number of $K_L^0 \to \pi^+\pi^-\pi^0$ events. Some charged pions undergo nuclear interactions in the air and detector materials as they traverse the spectrometer. In this cases the pion can fail to register a hit in the detectors which compose the L1 trigger. The estimated percentage of events with two pions that would fail the L1 trigger due to these interactions is about 1.5%[14].

Table 8.1 lists the values for the factors entering this calculation as well as the resulting sensitivity when each of these factors is sequentially incorporated. The statistical and systematic errors are added in quadrature to give one total error for each factor. The branching ratio for $K_L^0 \to \pi^0 e^+ e^-$ if we had a single event (single event sensitivity) is obtained from equation 8.1 without the factor of 2.3. This result is 2.6×10^{-7}

The factor of 2.3 in equation 8.1 takes us from the limit on the branching ratio based on our single event sensitivity to the limit based on a 90% confidence level (C.L.). If the actual branching ratio for $K_L^0 \to \pi^0 e^+ e^-$ is greater than the 90% C.L. limit then there is less than 10% probability that we observe 0 events.

Assume that p is the real probability for a single K_L^0 to decay as $K_L^0 \to \pi^0 e^+ e^-$. If we have N events that could have decayed into $\pi^0 ee$ then 1/N is our single event sensitivity. The probability that none of them decayed that way is $(1-p)^N$. We therefore need to solve:

$$(1-p)^N < 0.1 \quad \text{or} \quad N \ln(1-p) < \ln(0.1) = -2.3$$

This approximates to solving:

$$-Np < -2.3 \implies p < 2.3/N$$

The same result can be obtained from Poisson statistics, which is the limit of very small p in the binomial statistics. In this case $\lambda = Np$ is the expected number of events. The probability of observing m events is:

$$P(m;\lambda) = \frac{e^{-\lambda}\lambda^m}{m!}.$$

For $m = 0$ we require:

$$P(0;\lambda) < 0.1 \implies e^{-\lambda} < 0.1$$

Which results in:

$$\lambda = Np < 2.3 \quad \text{or} \quad p < 2.3/N$$

which is identical to the binomial analysis.

When multiplying the single event sensitivity branching ratio by 2.3 we get our final result:

$$B(K_L^0 \to \pi^0 e^+ e^-) \; < \; 6.0 \times 10^{-7} \qquad (90\% \text{ C.L.})$$

The error in this calculation is approximately 5%. This is the result of adding in quadrature the errors of each of the factors in equation 8.1 (see Table 8.1).

8.2 Conclusions

This result is consistent with other limits recently established[2,3]. It is not the best the experiment could have done in the 1988 running period given the present detector configuration. Up to a factor of two in signal could have been gained by having had the L1 and L3 triggers ready earlier in the run. Another factor of 1.2 was lost due to the mistake in the colinearity cut in the two-body part of the L3 trigger. And, possibly, the efficiency of the three-body L3 algorithm could have been improved by about 20% by having had updating calibration constants and by having used the converter blocks in the energy measurement. These factors combine to give, approximately, a factor of 3 improvement in the sensitivity. This would have resulted in a 2.0×10^{-7} limit for $K_L^0 \to \pi^0 e^+ e^-$.

Clearly, the optimization of the E791 detector for $K_L^0 \to \mu e$ impaired the search for $K_L^0 \to \pi^0 e^+ e^-$. In addition we lost sensitivity by having to apply stringent cuts on electron identification, on track-to-photon separation and on timing. This is consistent with having backgrounds coming from the copious $K_L^0 \to \pi^\pm e^\pm \nu$ (where the pion is misidentified as an electron) with two accidental "photons". (A photon could have also been faked by an accidental charged particle.) This suggests that in this high rate environment one needs excellent timing, better electron identification and a calorimeter that is more segmented and has better energy resolution. Other backgrounds coming from the Dalitz decay of neutral pions do not play a role in our experiment due to the fact that we do not have any acceptance for low invariant mass electron-positron pairs.

The present generation of $K_L^0 \to \pi^0 e^+ e^-$ experiments has searched for this decay as a by-product of the main purposes of the experiments. A sensitivity of a few times 10^{-8} has been reached, and no events have been observed. A newer generation of optimized and dedicated experiments is expected to achieve sensitivities of 10^{-10} to 10^{-11}. These experiments are, or will be, performed in Europe (CERN), Japan (KEK) and the U.S. (BNL and FNAL). Table 8.2 summarizes the present and future status of $K_L^0 \to \pi^0 e^+ e^-$. Ideas for even more sensitive experiments are just emerging, but no doubt they will at least require very sophisticated and costly equipment if not new, yet to be developed, technology.

REFERENCES

1) A. Carroll *et al.*, Phys. Rev. Lett. **44** (1980), 525.

2) L.K. Gibbons *et al.*, "New limits on $K_L^0 \to \pi^0 e^+ e^-$ Phys. Rev. Lett. **61** (1988), 2661.

3) G.D. Barr *et al.*, "Search for the Decay $K_L^0 \to \pi^0 e^+ e^-$", MZ-ETAP-88-18, October 1988.

4) C.O. Dib, I. Dunietz, F.J. Gilman, "CP Violation in the $K_L^0 \to \pi^0 e^+ e^-$ Decay Amplitude for Large m_t", SLAC-PUB-4762, Nov. 1988.

5) J.F. Donoghue, B.R. Holstein, G. Valencia, $K_L^0 \to \pi^0 e^+ e^-$ as a probe of CP violation", Phys. Rev. D35 (1987) 2769.

6) F.J. Gilman, M. Wise, Phys. Rev. **D20** (1979) 2392; 21 (1980) 3150.

7) J.M. Flynn, L. Randall, "The CP Conserving Long-Distance Contribution to the Decay $K_L^0 \to \pi^0 e^+ e^-$", Phys. Lett. **B216** (1989) 221.

8) J.M. Flynn, L. Randall, "The CP Violating Contribution to the Decay $K_L^0 \to \pi^0 e^+ e^-$", LBL-26310/RAL-88-108, Nov. 1988.

9) G. Ecker, A. Pich, E. de Rafael, $K \to \pi \ell^+ \ell^-$ Decays in the Effective Chiral Lagrangian of the Standard Model", Nucl. Phys. **B303** (1988) 665.

10) L.M. Sehgal, "CP Violation in $K_L^0 \to \pi^0 e^+ e^-$ Interference of One-Photon and Two-Photon Exchange", Phys. Rev. **D38** (1988) 808.

11) T. Morozumi, H. Iwasaki, "The CP-conserving contribution to the decays $K_L^0 \to \pi^0\gamma\gamma$ and $K_L^0 \to \pi^0 e^+ e^-$, KEK-TH-206 (1988).

12) C.O. Dib, Ph.D. dissertation, "Rare K Meson Decays in the Case of a Heavy Top Quark", Stanford University, Jun. 1989.

13) Particle Data Group, "Review of Particle Properties", Phys. Lett. **B204** (April 1988).

14) C. Mathiazhagan, *et al.*, "New experimental Limits on $K_L^0 \to \mu e$ and $K_L^0 \to ee$ Branching Ratios", Phys. Rev. Lett., **63**, 2181 (1989).

15) L.J. Hall, L. Randall, "CP Volation from Scalar Leptoquarks", Nucl. Phys. **B274** (1986) 157.

16) R.S. Chivukula, H. Georgi, Phys. Lett. **188B** 99, (1987); Phys. Rev. **D36** 2102 (1987).

17) R.D. Cousins, *et al.*, "Study of Very Rare K_L^0 decays", Brookhaven National Laboratory, AGS Proposal E791 (June 1984).

18) R.D. Cousins, *et al.*, "32-Channel Digital 6-Bit TDC with 2.5 NS Least Count", IEEE Trans. Nucl. Sci., **36**, 646 (1989).

19) J. Konigsberg, "E791 Magnetic Field", E791 collaboration memorandum **KL-134**, October 1987.

20) R.D. Cousins, "Poisson Modeling of the E791 Spectrometer Magnets", E791 collaboration memorandum **KL-155**, June 1988.

21) K. Biery, *et al.*, IEEE Trans. Nucl. Sci., **36**, 650 (1989).

22) J. Frank, *et al.*, IEEE Trans. Nucl. Sci, **36**, 79, (1989).

23) P. Buchholz, K. McFarlane, "E791 Level 1 Trigger. Changes for the February Run 1988", January 1988.

24) R.D. Cousins, *et al.*, "Fast Parallel Pipelined Readout Architecture for a Completely Flash Digitizing System with Multi-Level Trigger", Nucl. Instr. and Meth., **A277**, 517 (1989).

25) P.F. Kunz, *et al.*, SLAC-PUB-3069, CERN/ DD/ 83/3 (1983).

26) J. Ritchie, "Level 3 Efficiency for $K_L^0 \to \pi^0 e^+ e^-$", E791 collaboration memorandum **KL-259**, November 1989.

27) P. Buchholz, M. Sivertz, "E791 Level 1 trigger bit efficiencies", E791 collaboration memorandum **KL-180**, December 1988.

28) W.H. Press *et al.*, *Numerical Recipes, The Art of Scientific Computing*, Cambridge University Press (1986).

29) C. Fabjan and T. Ludlam, "Calorimetry in High-Energy Physics", Ann. Rev. Nucl. Part. Sci. **32**:335-89, 1982.

30) Skubic *at al.*, Phys. Rev. **D18** 76 (1978).

31) J.B. Marion and B.A. Zimmerman, "Multiple Scattering of Charged Particles", Nucl. Inst. and Meth. **51**, 93 (1973).

32) V.L. Highland, "Some Practical Remarks on Multiple Scattering", Nucl. Inst. and Meth. **129**, 497 (1975).

33) David Wagner, "An Electron Bremsstrahlung Study", E791 collaboration memorandum **KL-156**, Aug. 1988.

34) Yung-Tsu Tsai, Reviews of Modern Physics, **46**, 4 (1974) and errata in **42**, 9 (1977).

35) David Wagner, "Tuning Pattern Recognition" E791 collaboration memorandum **KL-213**, Aug. 1988.

36) M. Sivertz, "E791 Muon Particle Identification Efficiency", E791 collaboration memorandum **KL-176**, Oct. 1988.

37) J. Ginkel, "Summary of Rangefinder Studies for Spring 1988", E791 collaboration memorandum **KL-169**, Aug. 1988.

38) J. Margulies, "Electron Identification in the 1988 Dilepton Analysis", E791 collaboration memorandum **KL-196**, Sep. 1989.

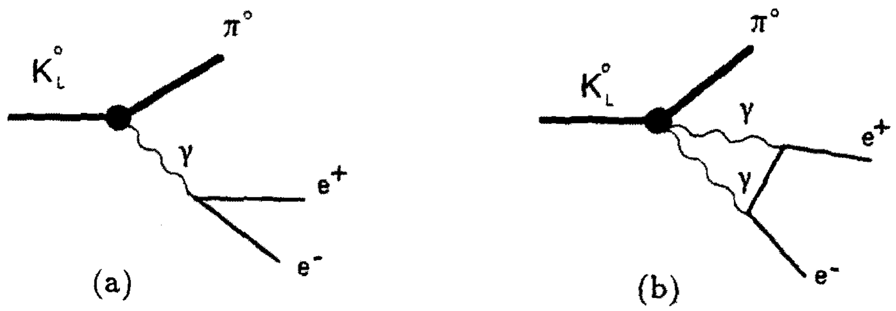

Figures 2.1. One and two-photon amplitudes for $K_L^0 \to \pi^0 e^+ e^-$

Figure 2.1(a) shows the diagram for the *CP* violating $K_L^0 \to \pi^0 e^+ e^-$ decay via one single photon. In figure 2.1(b) the decay proceeds through two intermediate virtual photons and *CP* is not necessarilly violated. See section 2.1.

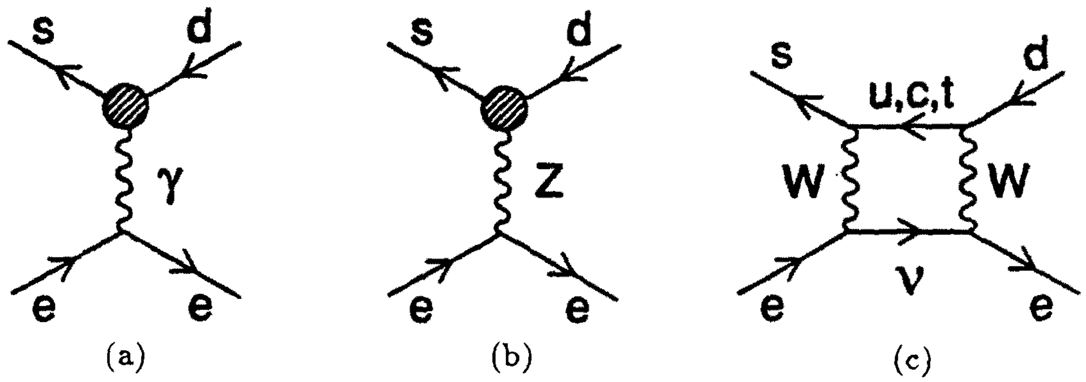

Figures 2.2. *CP* violating diagrams in $K_L^0 \to \pi^0 e^+ e^-$

Figure 2.2(a) is the "electromagnetic penguin", expected to dominate the transition. For large m_t the contributions of the "Z penguin" (Fig. 2.2(b)) and the "W box" diagrams need to be taken into account. See section 2.2. (Figure source: C.O. Dib, Ph.D. Dissertation, Stanford University).

Composition:	%
SiO_2	46 %
Na_2	5 %
K_2O	4 %
PbO	45 %

Parameters:	value
Glass type	Schott type F2
Density	3.6 g/cm^3
Index of Refraction	1.62
Electromagnetic Rad. Length	3.06 cm
Hadronic Int. length	35 cm
Critical Energy	18 MeV

Table 3.1. Lead glass characteristics

The table lists some of the important features of the lead glass block used in our electromagnetic calorimeter (Sec. 3.3).

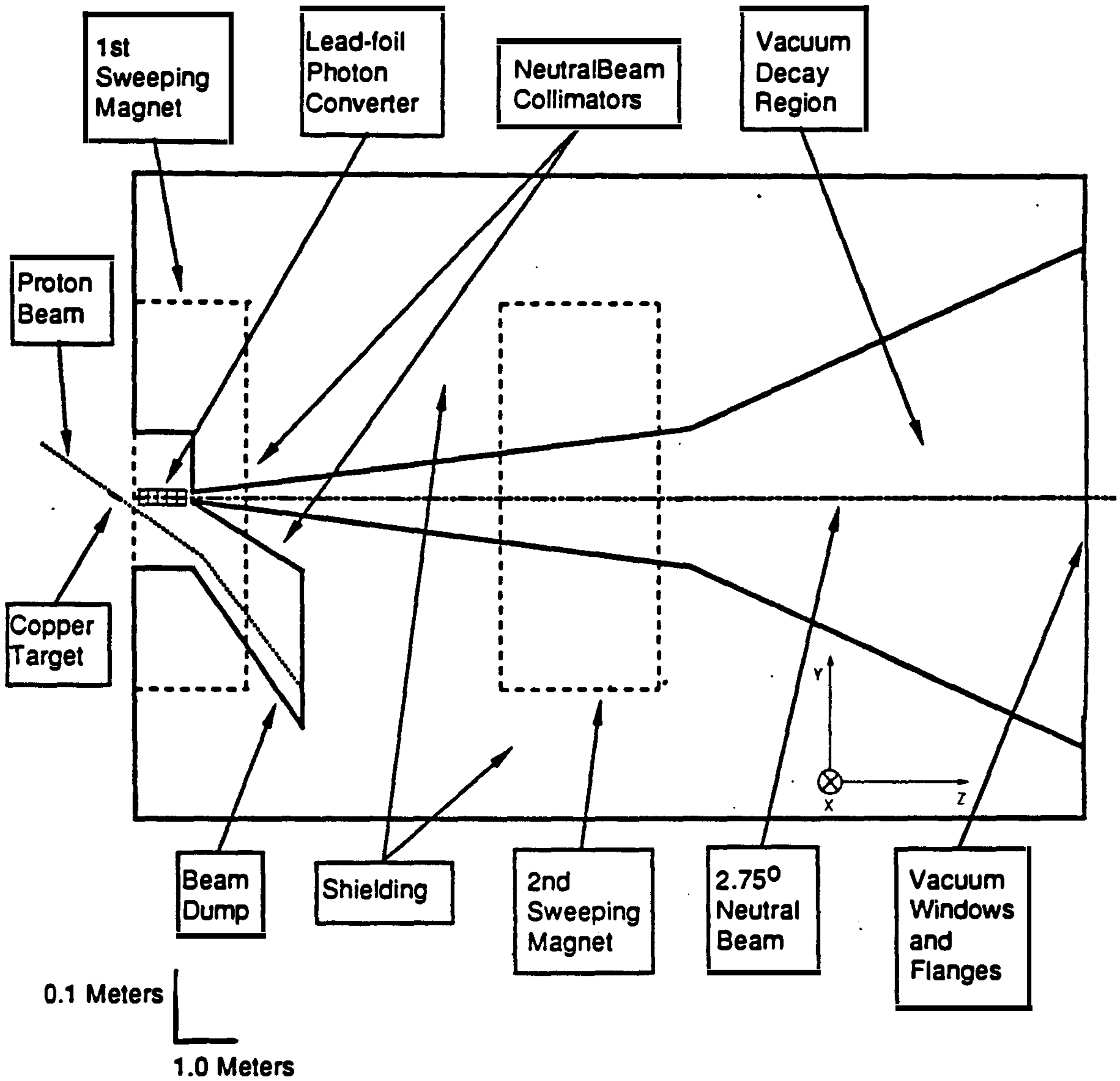

Figure 3.1. E791 neutral beamline, elevation view

The 24 Gev/c^2 proton beam hits a copper target. The neutral beam comes out at an angle of 2.75 degrees and it is collimated into a 10 meter long decay region. Charged particles are swept away by dipole magnets. The K_L^0 beam spans a 60 μsr solid angle. (Figure source: C. Kenney, Ph.D. Dissertation, The College of William and Mary).

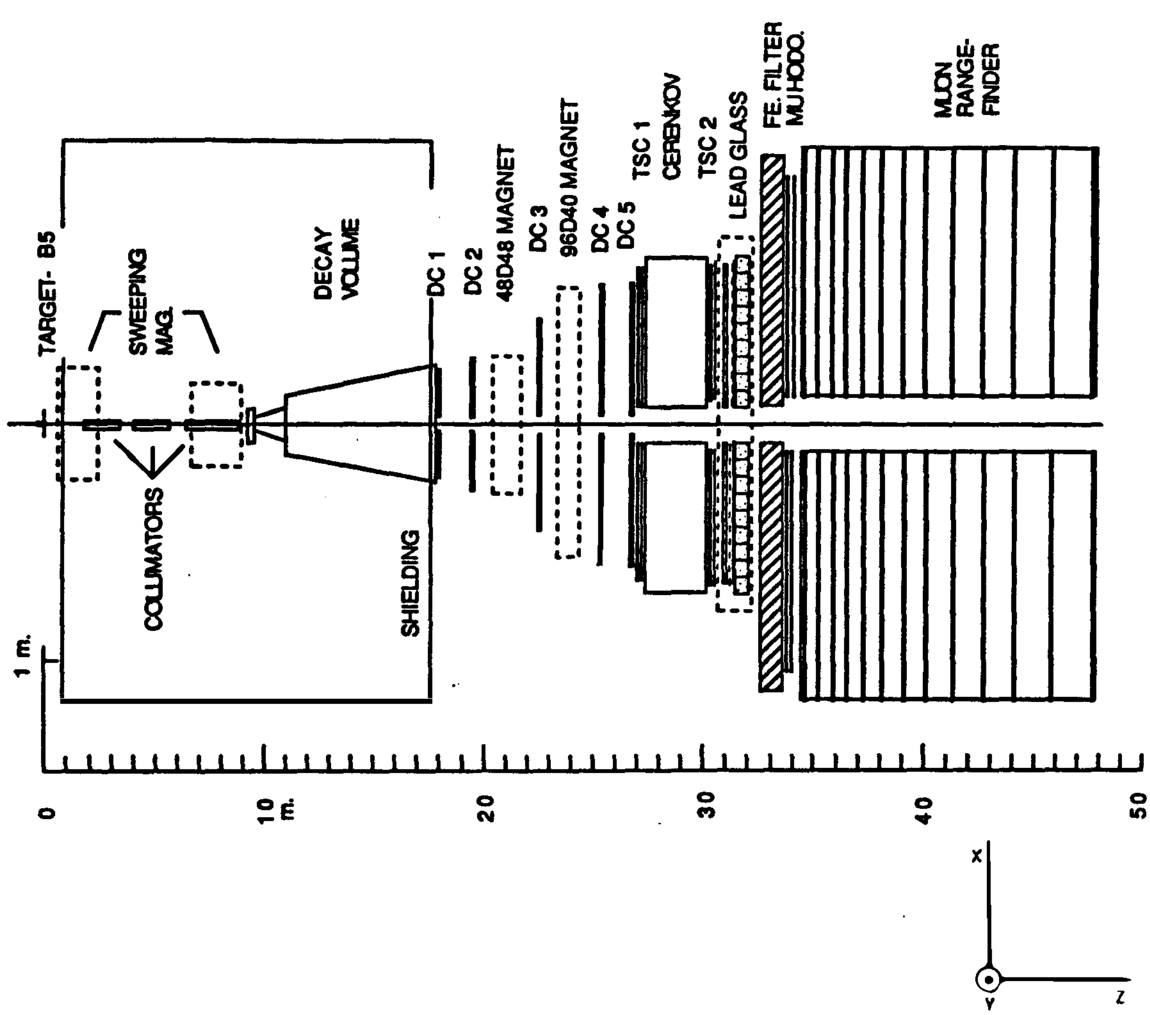

Figure 3.2. E791 detector, plan view

The detector is formed of two identical arms. Five drift chamber planes (DC) and two trigger scintillation counters (TSC) are used for tracking and triggering. The lead glass array (PBG), Čerenkov counter (CER), muon hodoscope (MHO) and muon range-finder are used for particle identification. See chapter 3 for a detailed description of these detectors. (Figure source: C. Kenney, Ph.D. Dissertation, The College of William and Mary).

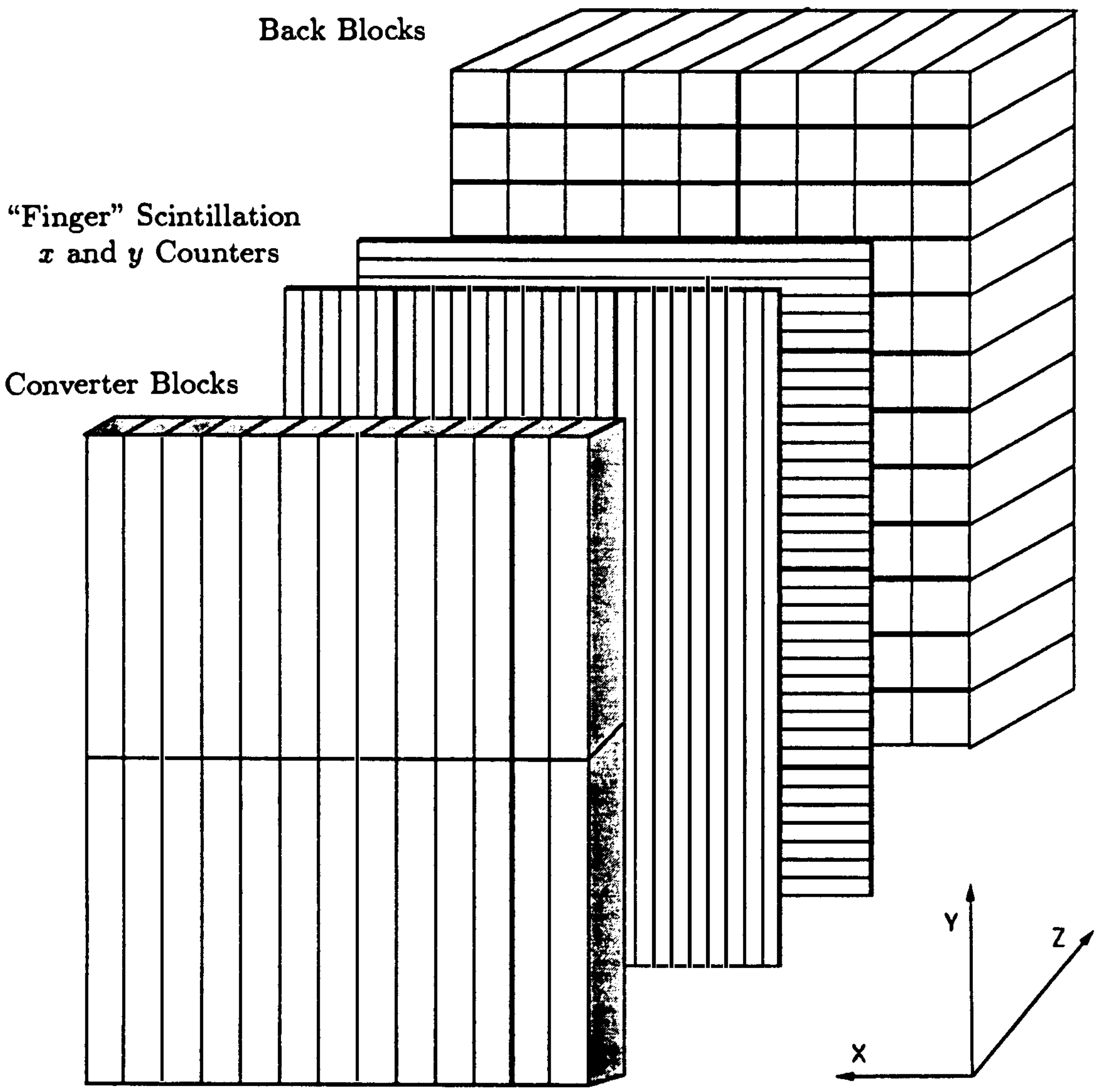

Figure 3.3. E791 Lead Glass Array

The Lead Glass Array is composed of three sections. The converter lead-glass blocks are used to force electrons and photons to convert into electromagnetic showers. The "finger" counters are an array of scintillating slats which measures the time and position of showers. The back lead-glass blocks measure the shower's energy. (Figure source: C. Kenney, Ph.D. Dissertation, The College of William and Mary).

Bit Set	Event Type	Logic Definition
0	μ e	L0·DC12·μ_L·e_R
1	eμ	L0·DC12·e_L·μ_R
2	$\mu\mu$	L0·DC12·μ_L·μ_R
3	ee	L0·DC12·e_L·e_R
4	Min Bias	L0·DC12
5	$\pi\pi$	L0·DC12·$\overline{e}_L \cdot \overline{e}_R \cdot \overline{\mu}_L \cdot \overline{\mu}_R$
6	$ee\gamma$	L0·DC12·e_L·e_R·γ
7	$\mu\mu\gamma$	L0·DC12·μ_L·μ_R·γ

Table 4.1. E791 Physics Level 1 triggers

If any of the triggers is satisfied a bit is set in the Level 1 trigger word. Triggers are inclusive, i.e. an event may satisfy more than one of the criteria. In that case more than one bit will be set. Only for the $\pi\pi$ trigger (not used in the analysis) vetoes were allowed. The logic definitions are found in section 4.1.

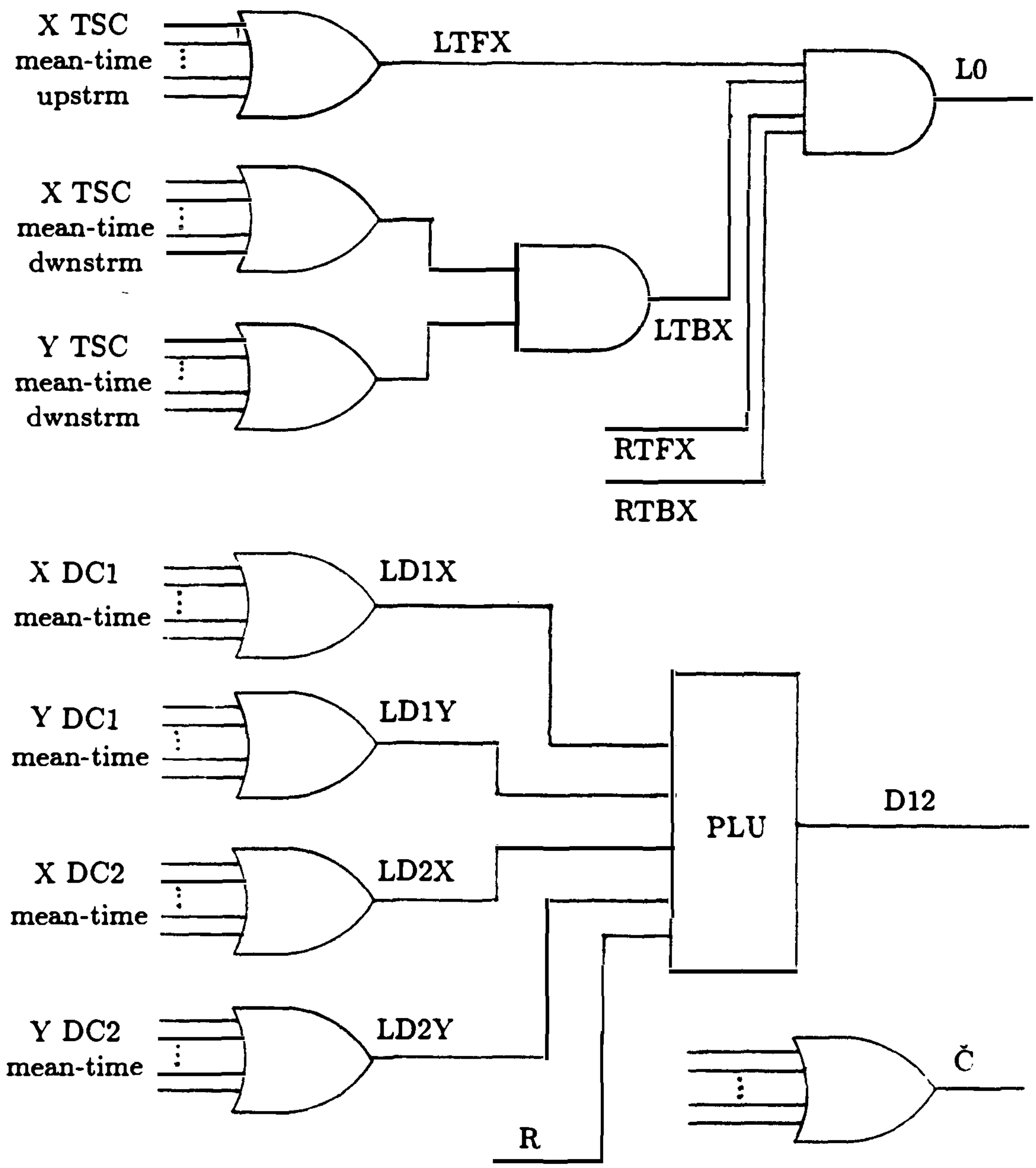

Figure 4.1. E791 Level 1 Schematic

This figure shows schematically the logic used in the Level 1 configuration (Sec. 4.1). The coincidence between the trigger counter's L0 signal and the drift chamber's D12 signal forms the minimum bias trigger. The Čerenkov signals provide electron identification.

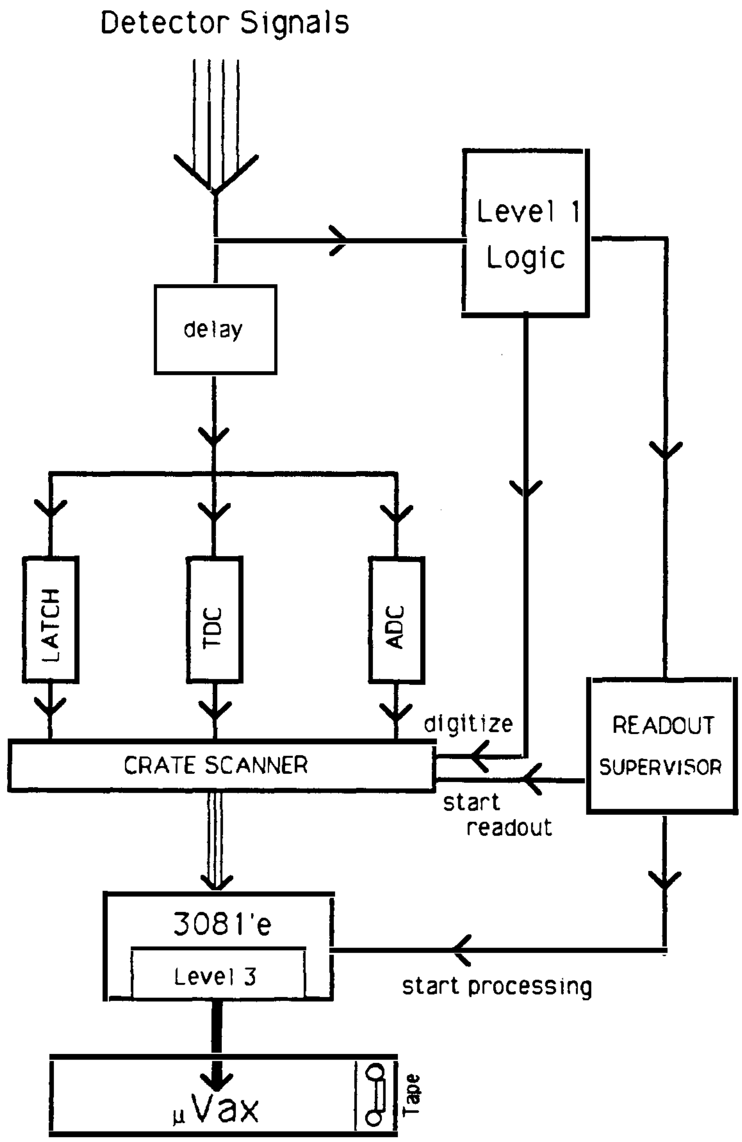

Figure 4.2. E791 Readout Schematic

This figure shows schematically the flow of information from the detectors to the magnetic tape. Logic decisions are provided by the readout supervisor and the Level 1 trigger (see Sec. 4.2). For simplicity only one of each element involved in the readout is shown.

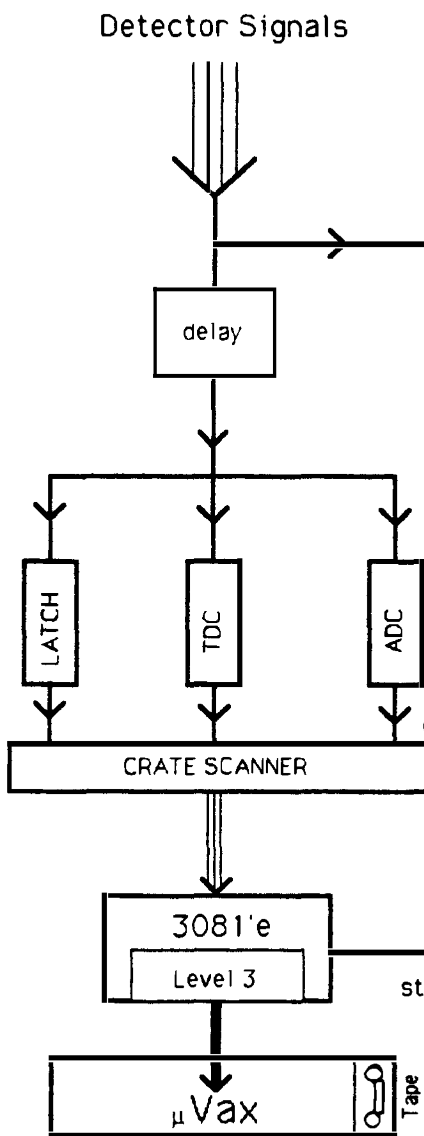

Figure 4.2. E791 Readout Schematic

This figure shows schematically the flow of information from the detectors to the magnetic tape. Logic decisions are provided by the readout supervisor and the Level 1 trigger (see Sec. 4.2). For simplicity only one of each element involved in the readout is shown.

Cut Parameter	$K_L^0 \to \pi^0 e^+ e^-$, select if:	$K_L^0 \to \pi^+ \pi^- \pi^0$, select if:
Level 1 bit	$ee\gamma$ bit set	Min. Bias bit set
TSC hits (tracks)	NHTUPX*NHTDNX ≥ 2 NHTUPY+NHTDNY ≥ 1	NHTUPX*NHTDNX ≥ 2 NHTUPY+NHTDNY ≥ 1
# of π^0's	≥ 1	≥ 1
$\chi^2_{\pi^0}$	$\chi^2_{\pi^0} \leq 30.$	$\chi^2_{\pi^0} \leq 30.$
Θ_c^2	$\Theta_c^2 \leq 15.$ mrad	$\Theta_c^2 \leq 15.$ mrad
$m_{\pi^0 e^+ e^-}$	$.450 \leq m_{\pi^0 e^+ e^-} \leq .550$ GeV	$.450 \leq m_{\pi^0 e^+ e^-} \leq .550$ GeV

Table 5.1. Selection Criteria in the First Offline Pass

When applying the above cuts, a reduction of the raw data by a factor of approx. 28 is achieved. NHTUPX(Y), NHTDNX(Y) are the number of in-time hits in the x(y) view of the upstream and downstream TSC respectively. The first offline pass used a fast swimming version. If any π^0 combination passes these criteria the event is kept. For a more detailed explanation on how these cuts are implemented see section 5.2.

Cut Parameter	$K_L^0 \to \pi^0 e^+ e^-$, select if:	$K_L^0 \to \pi^+\pi^-\pi^0$, select if:
Level 1 bit	$ee\gamma$ bit set	Min. Bias bit set
E_C/E, tracks	$E_C/E \geq 0.04$	—
E/p, tracks	$E/p \geq 0.70$	—

Table 5.2. Selection Criteria in the Second Offline Pass

The ratio of lead glass converter blocks energy to total lead glass energy (E_C/E), together with the ratio of total lead glass energy to spectrometer momentum (E/p) serve to reject charged pions in the electron sample of $K_L^0 \to \pi^0 e^+ e^-$ candidates (Sec 5.4). Events were separated after this stage into two output streams: $K_L^0 \to \pi^0 e^+ e^-$ and $K_L^0 \to \pi^+\pi^-\pi^0$. If an event passes as both $K_L^0 \to \pi^0 e^+ e^-$ and $K_L^0 \to \pi^+\pi^-\pi^0$, the event is written out to both streams. In this pass, the fast swimming was also implemented. See section 5 2 for further details.

Cut Parameter	$K_L^0 \to \pi^0 e^+ e^-$, select if:	$K_L^0 \to \pi^+\pi^-\pi^0$, select if:
TSC hits, tracks	NHTUPX*NHTDNX ≥ 2 NHTUPY+NHTDNY ≥ 1	NHTUPX*NHTDNX ≥ 2 NHTUPY+NHTDNY ≥ 1
E_C/E, tracks	$E_C/E \geq 0.05$	—
E/p, tracks	$0.75 \leq E/p \leq 1.50$	—
D_{BB}^2, tracks	$D_{BB}^2 \leq 0.01$ meter^2	—
Čerenkov, tracks	good time & pulse height	—
Time diff., tracks	$\mid t_1^{trk} - t_2^{trk} \mid \leq 5.0$ ns	$\mid t_1^{trk} - t_2^{trk} \mid \leq 5.0$ ns
Time diff., photons	$\mid t_1^{\gamma} - t_2^{\gamma} \mid \leq 5.0$ ns	$\mid t_1^{\gamma} - t_2^{\gamma} \mid \leq 5.0$ ns
$\chi^2_{\pi^0}$	$\chi^2_{\pi^0} \leq 15.$	$\chi^2_{\pi^0} \leq 15.$
Θ_c^2	$\Theta_c^2 \leq 50$ μsr	$\Theta_c^2 \leq 50$ μsr

Table 5.3. Selection Criteria in the Third Offline Pass

In this pass, the standard swimming was used and the TSC requirements re-applied. Particle identification cuts on the lead glass for electrons are more stringent; tighter E/p and E_C/E and a new D_{BB}^2 cut (D_{BB} is the distance between the projected track and its cluster centroid in the back blocks), described in section 5.4, were applied. Also, to aid in charged-pion rejection, Čerenkov signals consistent with a "good" electron track were required (see Sec. 5.4 for details). Tracks needed to be in time with each other and so did the two photons. Times were measured in the "finger" counters (Sec 5.3). If any π^0 combination satisfied the photon timing condition and the $\chi^2_{\pi^0}$ and Θ_c^2 cuts, we would keep the event.

FNG Timing Cuts, select if:
$\mid t_1^{trk} - t_2^{trk} \mid \leq 4.0$ ns
-7.0 ns $\leq (t_1^{trk} - t_2^{trk}) \leq 5.0$ ns
$\mid t_1^{\gamma} - t_2^{\gamma} \mid \leq 4.0$ ns
-8.0 ns $\leq (t_1^{\gamma} - t_2^{\gamma}) \leq 4.0$ ns
-3.5 ns $\leq (2t_{avg}{}^{trk} - t_1^{\gamma}) \leq 4.5$ ns
-3.5 ns $\leq (2t_{avg}{}^{trk} - t_2^{\gamma}) \leq 4.5$ ns
0.0 ns $\leq (t_{max} - t_{min}) \leq 7.0$ ns
-8.0 ns $\leq (t_{max} + t_{min}) \leq 4.0$ ns

Table 5.4. Timing Constraints in the FNG counters

Tight timing proved to be essential in reducing $K_L^0 \to \pi^0 e^+ e^-$ background. Both $K_L^0 \to \pi^0 e^+ e^-$ and $K_L^0 \to \pi^+ \pi^- \pi^0$ candidates needed to pass these cuts. The track average time is simply $t_{avg} = (t_1^{trk} + t_2^{trk})/2$. t_{max} and t_{min} are the maximum and minimum times, respectively, of the four particle times in the event.

Cut Parameter	$K_L^0 \to \pi^0 e^+ e^-$, select if:	$K_L^0 \to \pi^+\pi^-\pi^0$, select if:
TSC hits, trks	NHTUPX*NHTDNX ≥ 2 NHTUPY+NHTDNY ≥ 1	NHTUPX*NHTDNX ≥ 2 NHTUPY+NHTDNY ≥ 1
Track vertex	$z \geq 9.5$ meter[2] $x/z \leq 0.0027$, $y/z \leq 0.01$	$z \geq 9.5$ meter[2] $x/z \leq 0.0027$, $y/z \leq 0.01$
Vac. win., trks	$x_{win} \geq 0.1003$ meter	$x_{win} \geq 0.1003$ meter
Momentum, trks	$\mid \vec{p}_e \mid \leq 8.0$ GeV	—
Inv. mass, trks	$m_{e^+e^-} \leq 0.370$ GeV	$m_{\pi^+\pi^-} \leq 0.370$ GeV
E_C/E, trks	$E_C/E \geq 0.055$	—
E/p, trks	$0.75 \leq E/p \leq 1.25$	—
D_{BB}^2, trks	$D_{BB}^2 \leq 0.01$ meter^2	—
Čerenkov, trks	good time & pulse height	—
FNG mom.	$\mid \bar{x} - x \mid, \mid \bar{y} - y \mid \leq 4$ cm (trks) # vert. ≥ 2, # horiz. ≥ 2	— —
FNG timing	see table 5.4	see table 5.4
Trk-γ dist.	cuts on PBG & FNG	cuts on PBG & FNG
Fiducial, γ's	No BB's inner column Clear detector edges	No BB's inner column Clear detector edges
Energy, γ's	$E_\gamma \geq 0.400$ Gev	$E_\gamma \geq 0.400$ Gev
$\chi^2_{\pi^0}$	$\chi^2_{\pi^0} \leq 7.0$	$\chi^2_{\pi^0} \leq 7.0$
Θ_c^2	$\Theta_c^2 \leq 50$ μsr	$\Theta_c^2 \leq 50$ μsr
Mass	$.450 \leq m_{\pi^0 e^+ e^-} \leq .550$ GeV	$.450 \leq m_{\pi^0 \pi^+ \pi^-} \leq .550$ GeV

Table 5.5. Final Selection Criteria

All cuts applied to all our $K_L^0 \to \pi^0 e^+ e^-$ and $K_L^0 \to \pi^+\pi^-\pi^0$ candidates are summarized in this table. A thourough description is found in chapter 5.

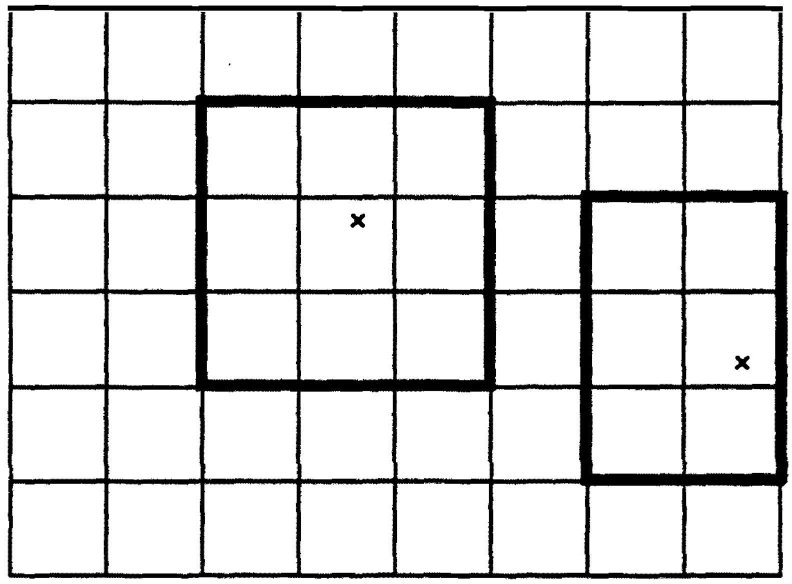

Figure 5.1. Lead glass back blocks energy cluster defintions. The x marks the projected track position. Energy is summed up for all blocks in the cluster. The same definition is used for photons.

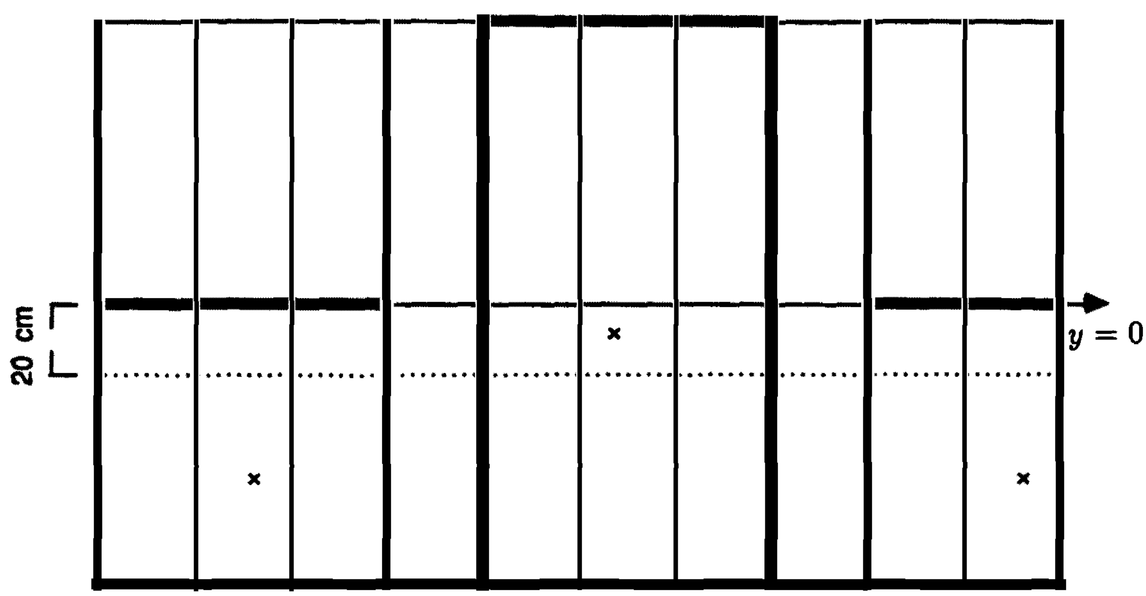

Figure 5.2. Lead glass converter cluster definitions, version A. The the x marks the projected track position. Energy is summed up for all blocks in the cluster.

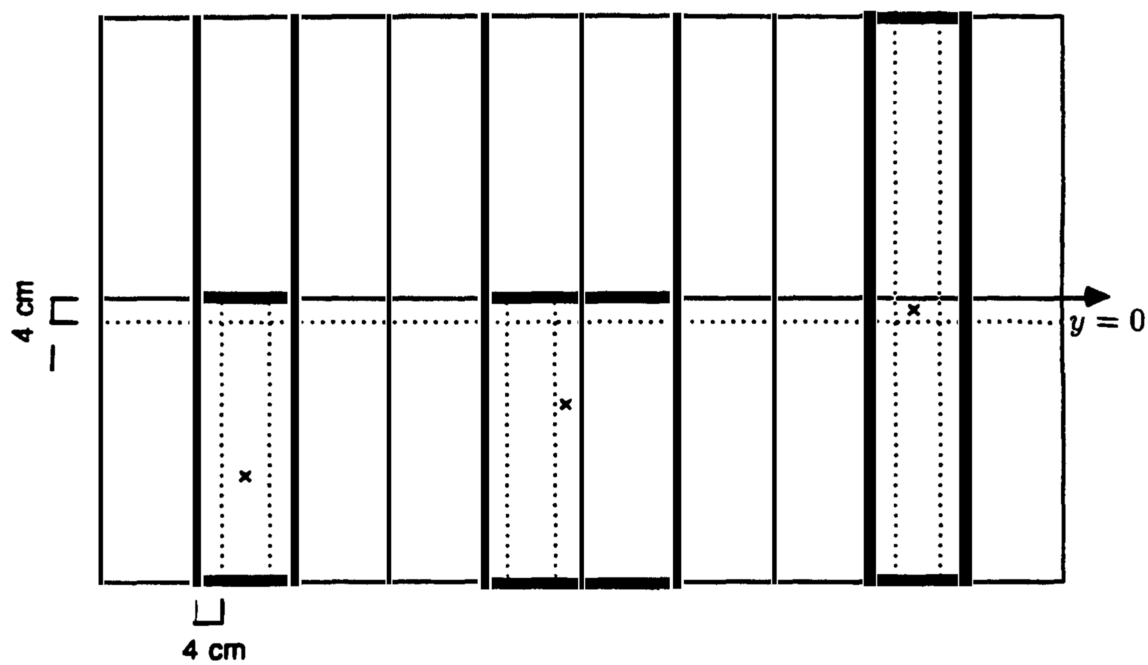

Figure. 5.3. Lead glass converter cluster definitions, version B. The the x marks the projected track position. Energy is summed up for all blocks in the cluster. If the track is more than 4 cm away from a block, that block is not part of the cluster.

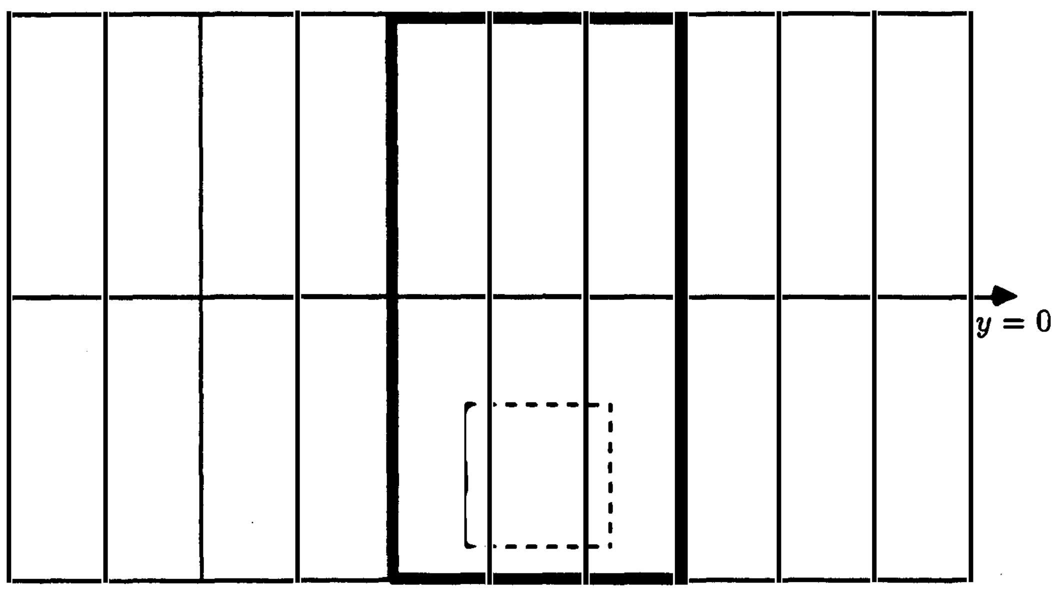

Figure 5.4 Lead glass converter cluster definitions, version A, photons. The broken line squares represent the principal back block for photon clusters. In this case all 6 converter blocks are included .

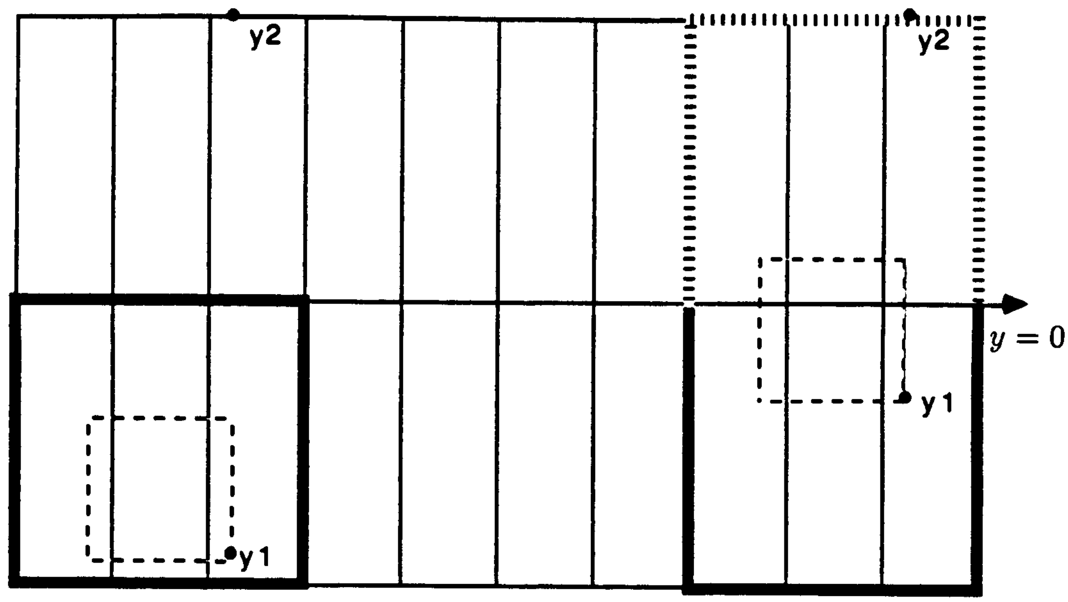

Figure 5.5. Lead glass converter cluster definitions, version B, photons. The broken line squares represent the principal back block for photon clusters. If the distance from y1 to y2 is less than 1.10 meters , the upper converter blocks will be included in the cluster.

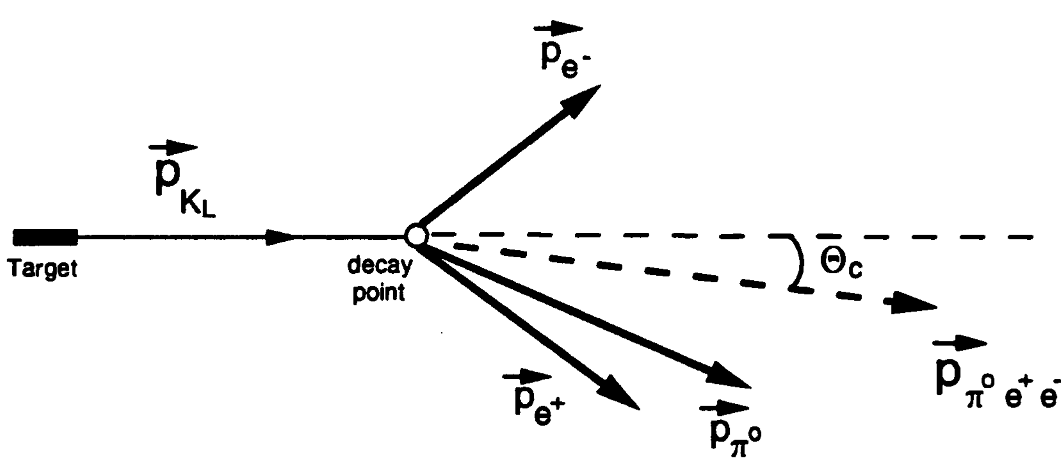

Figure 5.6. Colinearity Angle.

Θ_c is the angle between the direction of the reconstructed 3-momentum and the line connecting the target center to the reconstructed decay point.

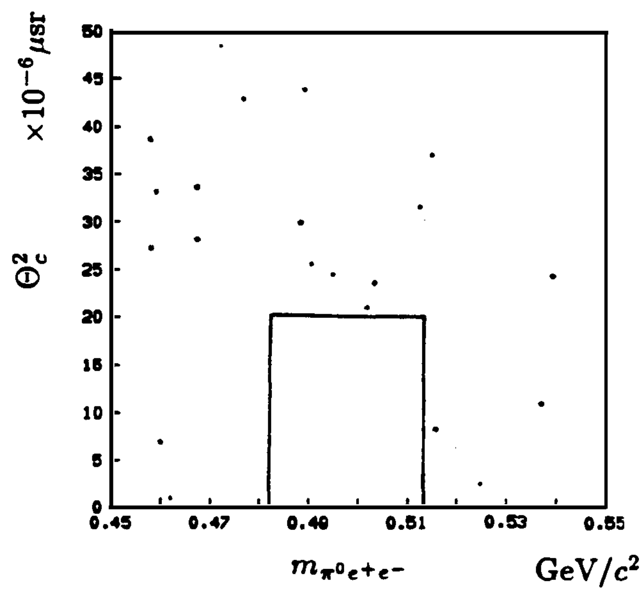

Figure 5.7(a). Θ_c^2 **vs.** $m_{\pi^0 e^+ e^-}$ **for the Final** $\pi^0 e^+ e^-$ **Data Sample.**

The box is the region in colinearity squared and invariant mass for which the sensitivity was calculated.

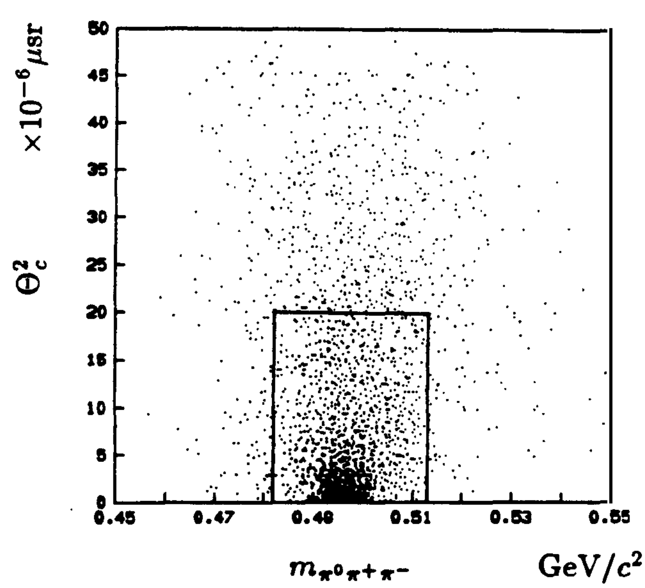

Figure 5.7(b). Θ_c^2 **vs.** $m_{\pi^0 \pi^+ \pi^-}$ **for the Final** $\pi^0 \pi^+ \pi^-$ **Data Sample.**

The box is the region in colinearity squared and invariant mass for which the final sensitivity was calculated.

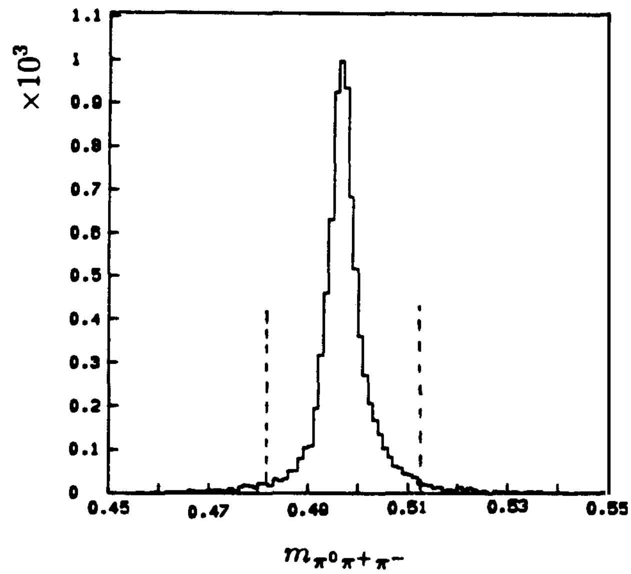

Figure 5.8. $m_{\pi^0\pi^+\pi^-}$ for the Final $\pi^0\pi^+\pi^-$ Data Sample.

This plot is the x projection of Figure 5.7(b). The lines show the region for which the sensitivity was calculated.

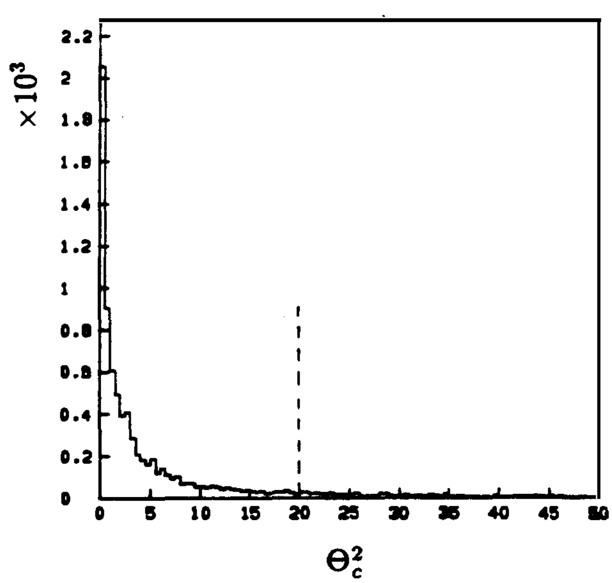

Figure 5.9. Θ_c^2 for the Final $\pi^0\pi^+\pi^-$ Data Sample.

This plot is the y projection of Figure 5.7(b). The lines show the region for which the sensitivity was calculated.

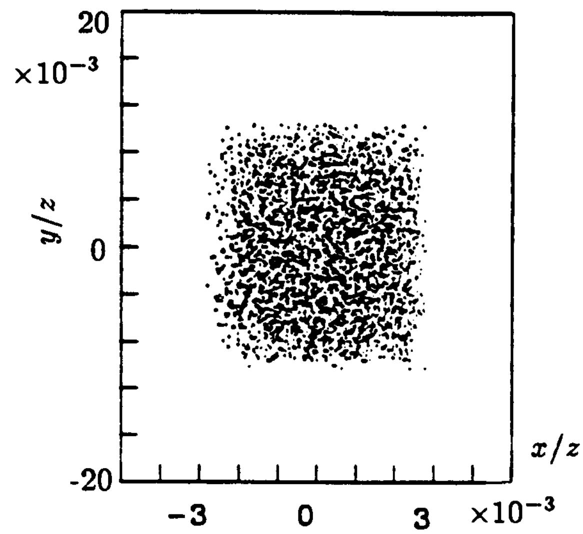

Figure 5.10. $K_L^0 \to \pi^+\pi^-\pi^0$: Beam Divergence

The plot shows the correlation between y/z and x/z for the reconstructed $K_L^0 \to \pi^+\pi^-\pi^0$ vertex.

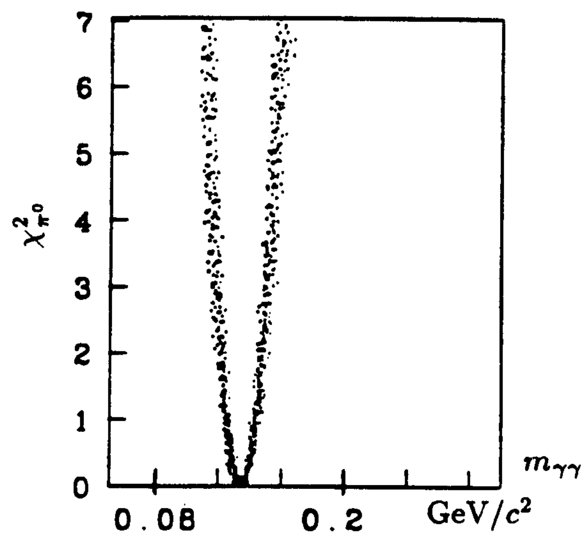

Figure 5.11. $K_L^0 \to \pi^+\pi^-\pi^0$: Chi-squared vs. Raw $m_{\gamma\gamma}$

$\chi^2_{\pi^0}$ is the minimum of the Chi-squared function formed by the energy and position measurements of the two photons in the event. It is subjected to the constrain that $m_{\gamma\gamma} = m_{\pi^0}$. $m_{\gamma\gamma}$ is the two-photon invariant mass calculated using the vertex position of the two charged tracks and the position and energy measurements of the two photons in the event.

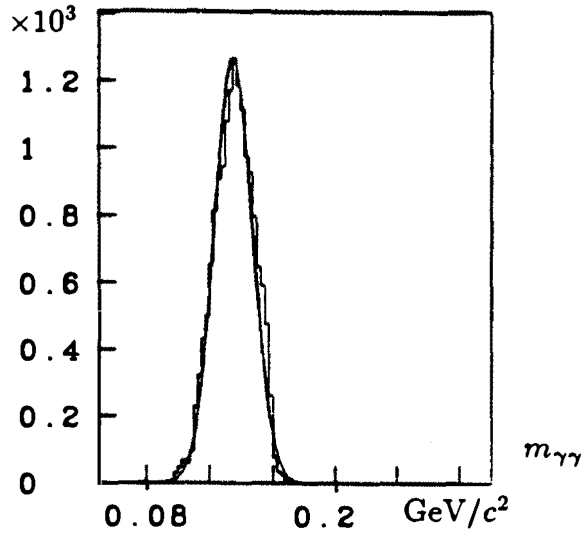

Figure 5.12. $K_L^0 \to \pi^+\pi^-\pi^0$: **Raw Two-Photon Invariant Mass.**

$m_{\gamma\gamma}$ is the two-photon invariant mass calculated using the vertex position of the two charged tracks and the position and energy measurements of the two photons in the event. This plot is the x projection of Fig. 5.11.

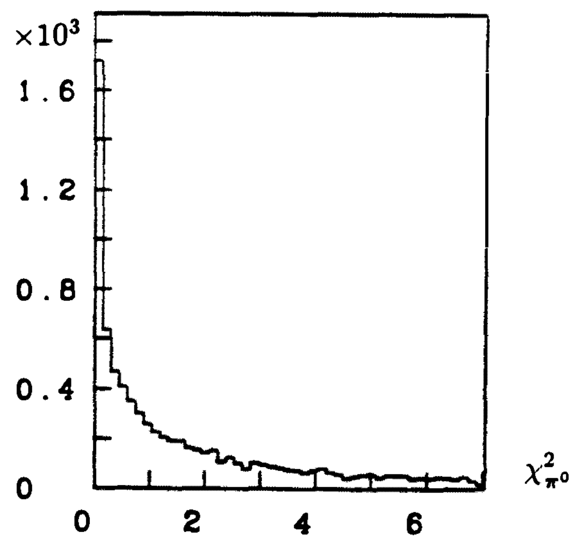

Figure 5.13. $K_L^0 \to \pi^+\pi^-\pi^0$: π^0 **Chi-squared .**

$\chi^2_{\pi^0}$ is the minimum of the Chi-squared function formed by the energy and position measurements of the two photons in the event, subjected to the constrain that $m_{\gamma\gamma} = m_{\pi^0}$ (where $m_{\gamma\gamma}$ is the raw invariant two-photon mass). This plot is the y projection of Fig. 5.10.

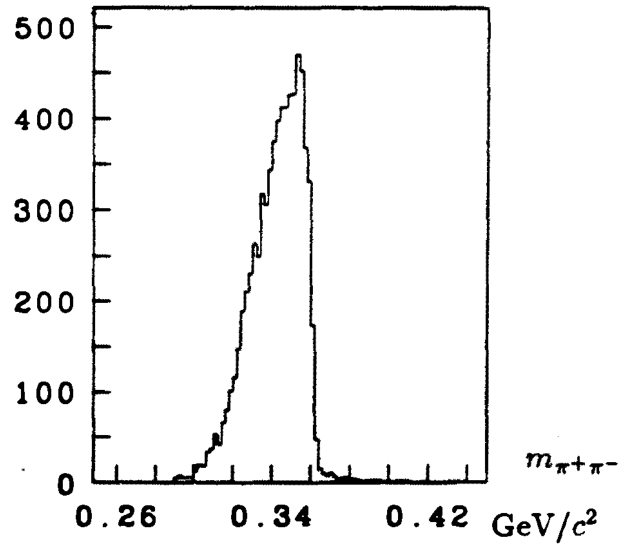

Figure 5.14. $K_L^0 \to \pi^+\pi^-\pi^0$: Two-pion invariant Mass.

The plot shows the invariant mass distribution ($m_{\pi^+\pi^-}$) for the two charged pions in our final $K_L^0 \to \pi^+\pi^-\pi^0$ sample.

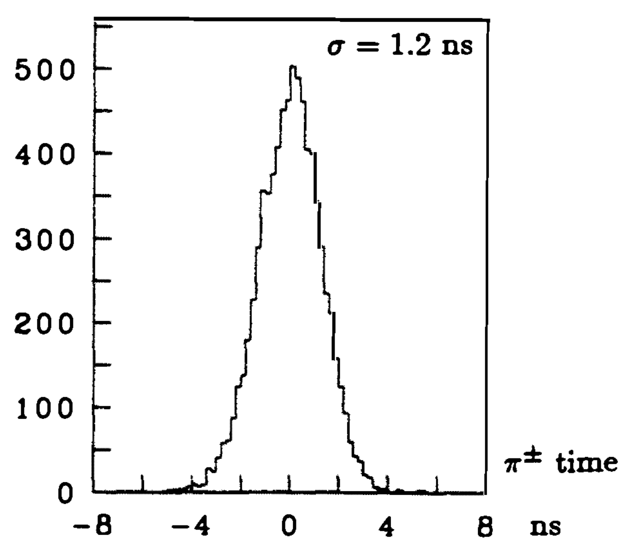

Figure 5.15. $K_L^0 \to \pi^+\pi^-\pi^0$: Charged Pions FNG times.

The measured times in the finger counters (FNG) for the two charged pions in our $K_L^0 \to \pi^+\pi^-\pi^0$ sample is shown.

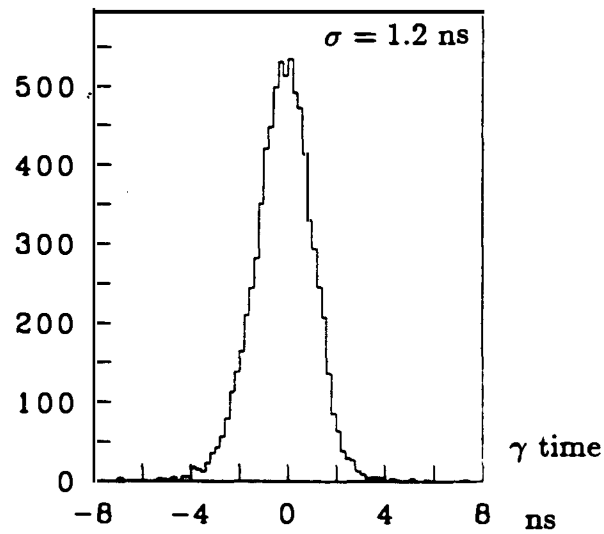

Figure 5.16. $K_L^0 \to \pi^+\pi^-\pi^0$**: Photons FNG times.**

The measured times in the finger counters (FNG) for the two photons in our $K_L^0 \to \pi^+\pi^-\pi^0$ sample is shown.

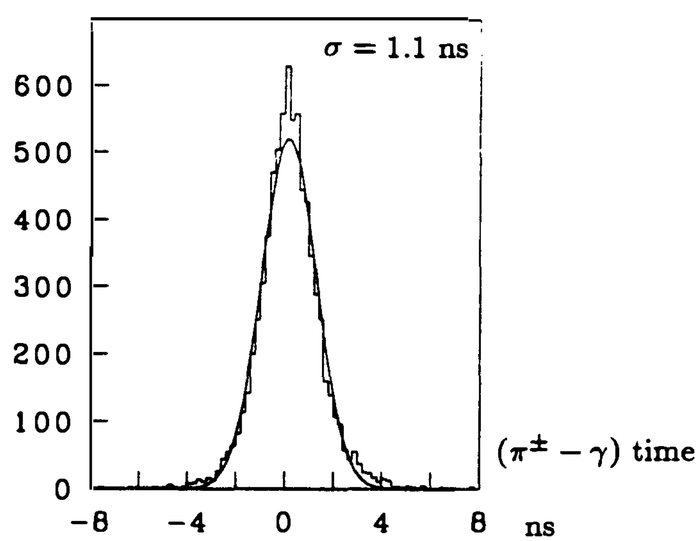

Figure 5.17. $K_L^0 \to \pi^+\pi^-\pi^0$**: Photons/Charged Pions Time Difference.**

We show the distribution of the charged pion FNG time minus the FNG time of the photon on the corresponding side of the detector for both pions in $K_L^0 \to \pi^+\pi^-\pi^0$.

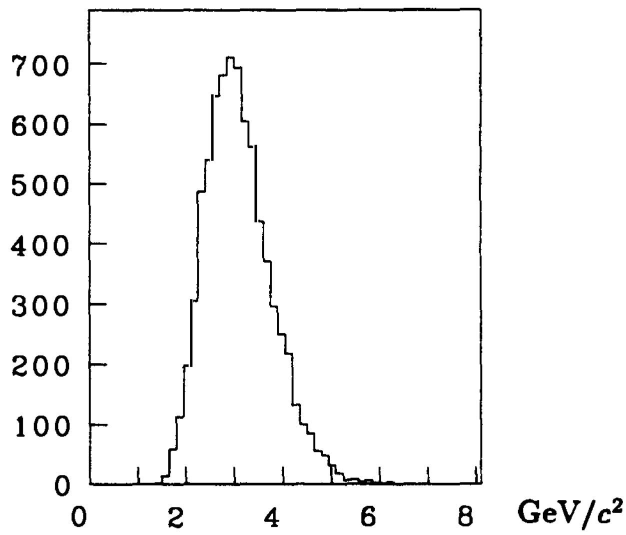

Figure 5.18. $K_L^0 \to \pi^+\pi^-\pi^0$: π^0 energy spectrum

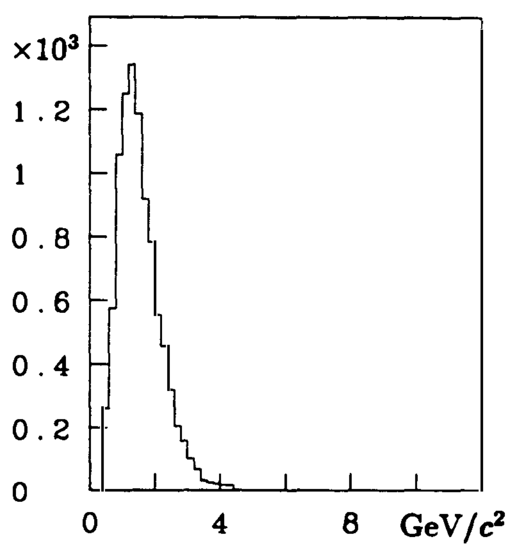

Figure 5.19. $K_L^0 \to \pi^+\pi^-\pi^0$: Photon energy spectrum

Aperture	z pos.	$\mid x \mid$ inn	$\mid x \mid$ out	$\mid y \mid$	rad. bef	rad. at
Vac window	17.8300					0.0018
D Ch 1	17.8888	0.076	0.472	0.405		0.0017
He Bag	19.43				0.0003	
D Ch 2	19.5045	0.082	0.582	0.421		0.0018
He Bag	0.10				0.0002	
Magnet 1	21.90		0.700	0.490	0.0002	
He Bag	22.43				0.0002	
D Ch 3	22.5628	0.091	0.934	0.526		0.0018
He Bag	23.49				0.0002	
Magnet 2	24.51		1.240	0.579	0.0002	
He Bag	25.13				0.0001	
D Ch 4	25.4135	0.097	1.265	0.625		0.0018
He Bag	26.63				0.0002	
D Ch 5	26.8867	0.102	1.290	0.779		0.0017
Trigg 1	26.99	0.145	1.435	0.920		0.0489
Čerenkov	29.855				0.0044	0.0383
Trigg 2	30.29	0.216	1.506	0.920		0.0619
PBG	31.15					13.8

Table 6.1. Detector Apertures and Radiation Lengths

The detector simulation in the Monte Carlo is characterized by these rectangular apertures. The two arms of the detector are identical. All numbers regarding size and position are in meters. $\mid x \mid$ inn/out are the inner/outer edges of the aperture while $\mid y \mid$ is half its vertical size. The drift chambers' dimensions are larger than the active area.

Decay Type	# evts. Gen.	# evts. acc. Geo.	Geo. Acc. $\times 10^{-4}$	Tot. # evts. acc.	Tot. Acc. $\times 10^{-5}$	Err Acc. $\times 10^{-5}$
$K_L^0 \to \pi^+\pi^-\pi^0$	8,923,121	21,243	23.80	4,726	52.96	0.8
$K_L^0 \to \pi^0 e^+ e^-$	12,136,519	5,768	4.75	974	8.02	0.3
Ratio			5.01		6.60	

Table 6.2. Monte Carlo acceptances for $K_L^0 \to \pi^+\pi^-\pi^0$ and $K_L^0 \to \pi^0 e^+ e^-$

This table shows the results for the acceptance study of Monte Carlo events performed in order to determine the $K_L^0 \to \pi^+\pi^-\pi^0$ to $K_L^0 \to \pi^0 e^+ e^-$ acceptance ratio. We determined that $A_{\pi^0\pi^+\pi^-}/A_{\pi^0 e^+ e^-} = 6.60 \pm 3.5\%$. The intermediate result of 5.01 is for the geometrical acceptance only.

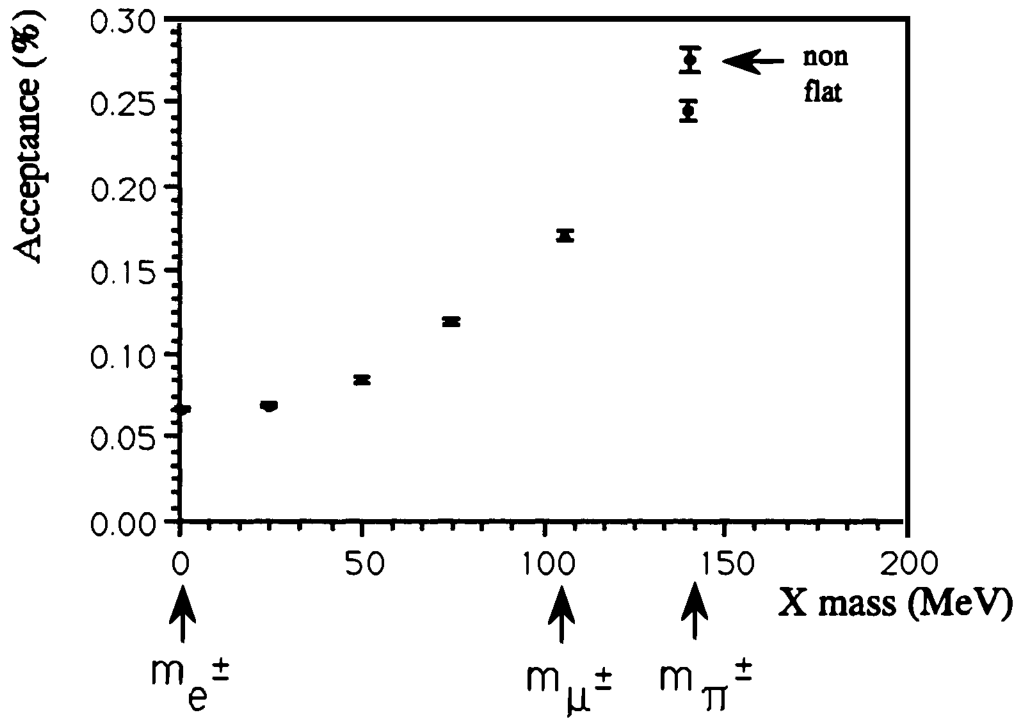

Figure 6.1. Geometrical acceptance for $K^0_L \to \pi^0 X^+ X^-$

The plot shows the variation of the geometrical acceptance for Monte Carlo generated $K^0_L \to \pi^0 X^+ X^-$ decays for various values of the mass of X, m_X. All points, except one, were generated using a uniform (flat) distribution on the Dalitz Plot. The two points at $m_X = m_{\pi^0}$ show the difference in acceptance when using a flat Dalitz density and the measured (non-flat) density[3].

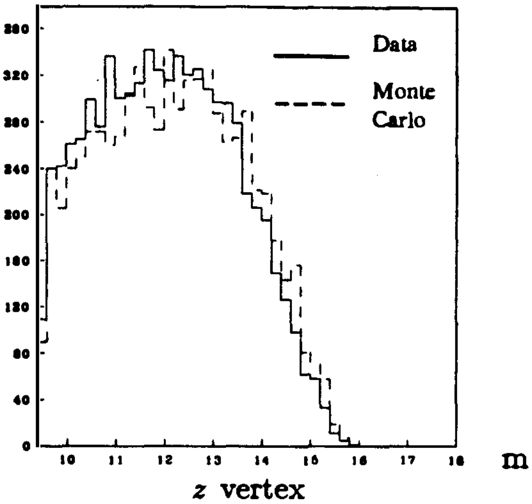

Figure 6.2. Vertex z position $K^0_L \to \pi^+\pi^-\pi^0$; Data vs. Monte Carlo

The solid line is the distribution of the z position of the reconstructed $K^0_L \to \pi^+\pi^-\pi^0$ vertex. The dashed line is the corresponding Monte Carlo distribution.

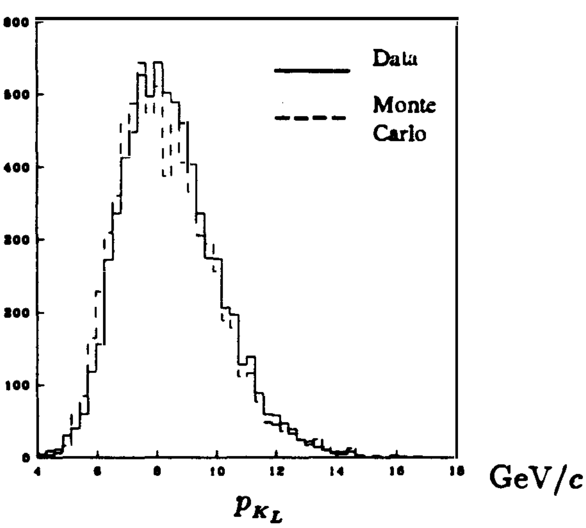

Figure 6.3. K^0_L momentum $K^0_L \to \pi^+\pi^-\pi^0$; Data vs. Monte Carlo

The solid line shows the the K^0_L momentum distribution for reconstructed kaons from $K^0_L \to \pi^+\pi^-\pi^0$ decays. The dashed line is the Monte Carlo distribution.

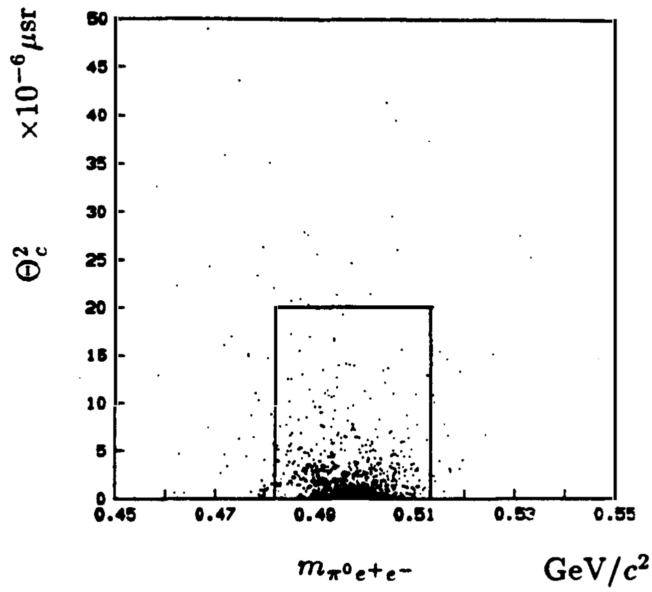

Figure 6.4(a). Θ_c^2 **vs.** $m_{\pi^0 e^+ e^-}$ **for** $K_L^0 \rightarrow \pi^0 e^+ e^-$ **Monte Carlo.**

The box is the region in colinearity squared and invariant mass for which the sensitivity was calculated.

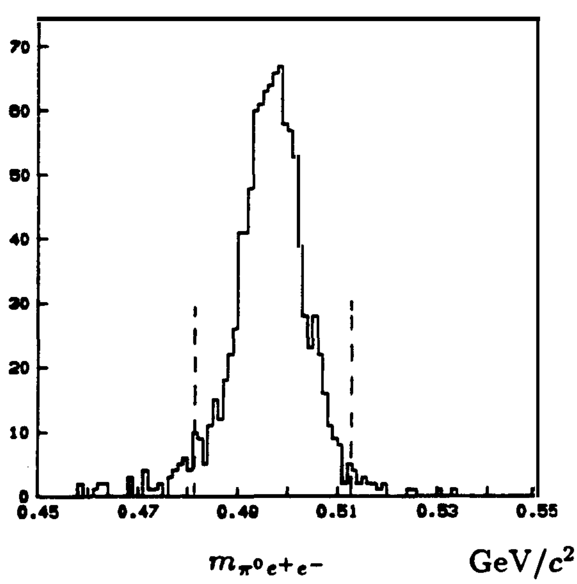

Figure 6.4(b). $m_{\pi^0 e^+ e^-}$ **for** $K_L^0 \rightarrow \pi^0 e^+ e^-$ **Monte Carlo.**

This plot is the x projection of Figure 6.4(a). The lines show the region for which the sensitivity was calculated.

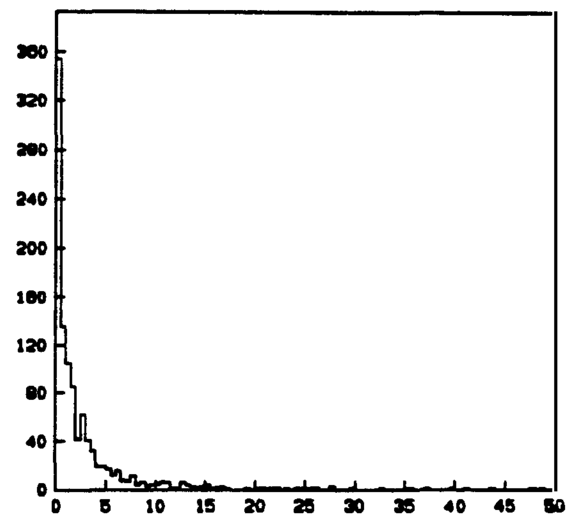

Figure 6.4(c). Θ_c^2 **for** $K_L^0 \to \pi^0 e^+ e^-$ **Monte Carlo.**

This plot is the y projection of Figure 6.4(a). The lines show the region for which the sensitivity was calculated.

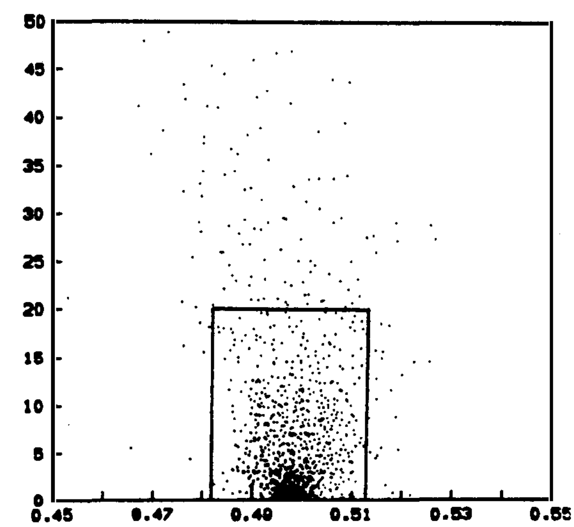

Figure 6.5(a). Θ_c^2 **vs.** $m_{\pi^0\pi^+\pi^-}$ **for** $K_L^0 \to \pi^+\pi^-\pi^0$ **Monte Carlo.**

The box is the region in colinearity squared and invariant mass for which the final sensitivity was calculated.

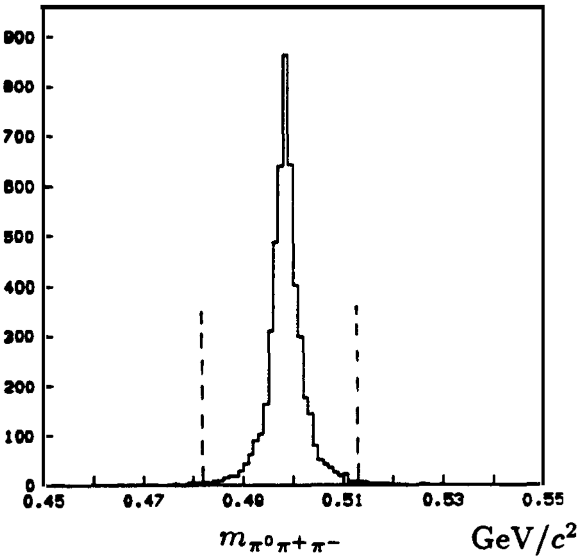

Figure 6.5(b). $m_{\pi^0\pi^+\pi^-}$ **for** $K_L^0 \to \pi^+\pi^-\pi^0$ **Monte Carlo.**

This plot is the x projection of Figure 6.5(a). The lines show the region for which the sensitivity was calculated.

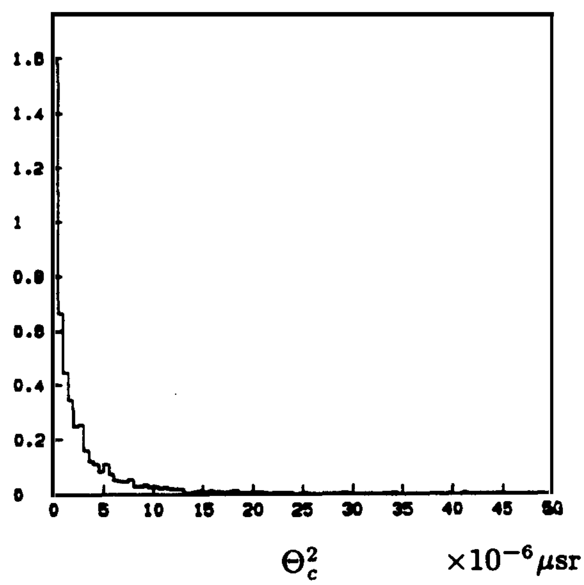

Figure 6.5(c). Θ_c^2 **for** $K_L^0 \to \pi^+\pi^-\pi^0$ **Monte Carlo.**

This plot is the y projection of Figure 6.5(a). The lines show the region for which the sensitivity was calculated.

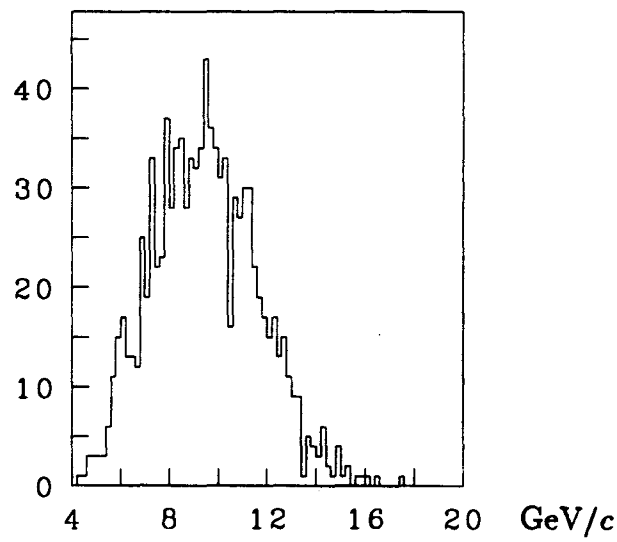

Figure 6.6. $K_L^0 \to \pi^0 e^+ e^-$ **Monte Carlo,** K_L^0 **momentum spectrum**

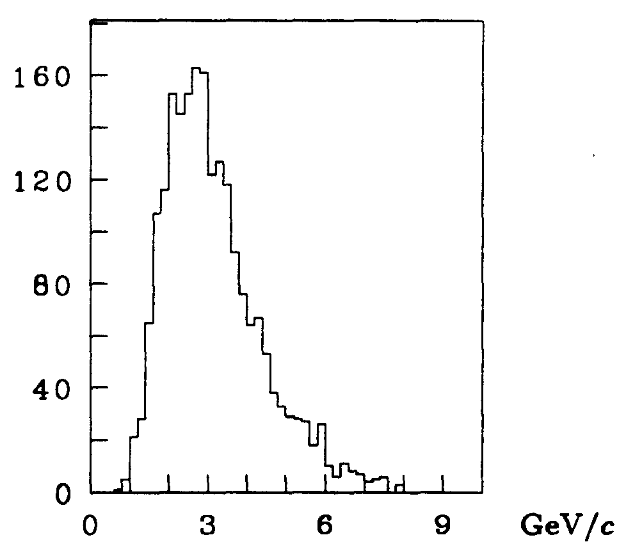

Figure 6.7. $K_L^0 \to \pi^0 e^+ e^-$ **Monte Carlo,** $e^\pm$ **momentum spectrum**

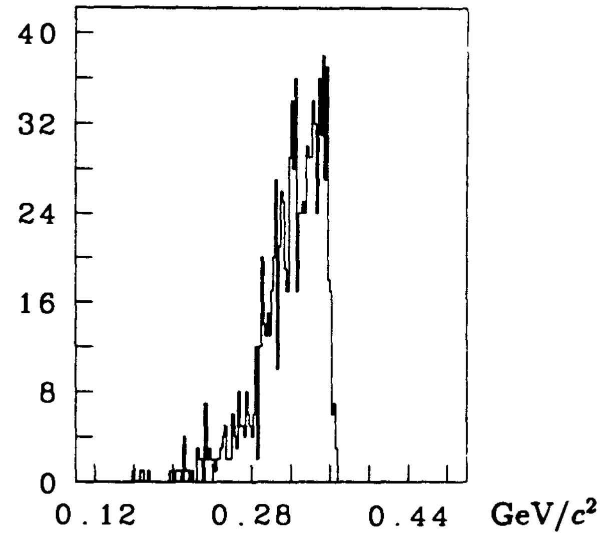

Figure 6.8. $K_L^0 \to \pi^0 e^+ e^-$ **Monte Carlo,** $m_{e^+e^-}$ **invariant mass**

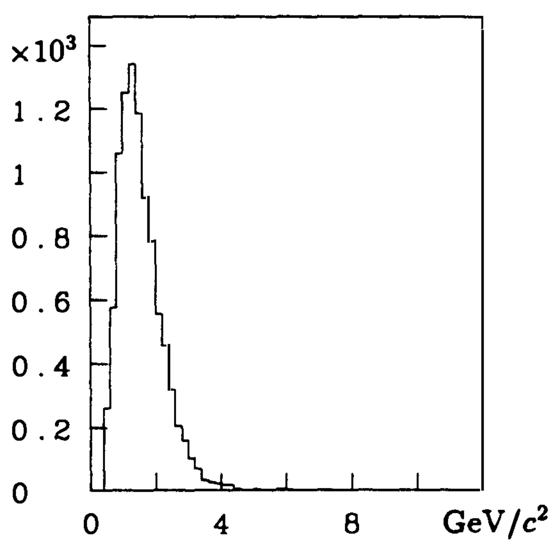

Figure 6.9. $K_L^0 \to \pi^0 e^+ e^-$ **Monte Carlo, Photon energy spectrum**

Cut #	Identify as electron if:	explanation
1	$0.75 \leq E/p \leq 1.50$	PBG energy / momentum
2	$E_C/E \geq 0.05$	Converter energy / PBG energy
3	$D^2_{BB} \leq 0.01$ meter^2	Track position to BB centroid dist.
4	$\mid \bar{x} - x \mid, \mid \bar{y} - y \mid \leq 4$ cm	Track position to FNG centroid dist.
5	# vert. ≥ 2, # horiz. ≥ 2	Num. of counters in FNG cluster

Table 7.1. Lead glass array electron selection criteria in $K^0_L \to \pi^0 e^+ e^-$

In the lead glass blocks, three cuts are implemented: E/p is the ratio of total lead glass energy to spectrometer momentum, E_C/E is the ratio of converter energy to total lead glass energy and D^2_{BB} is the square of the distance from the position of the projected track in the lead glass back blocks to the centroid of the cluster associated with that track. In the finger counters (FNG) the criteria are to select electrons by the small deviation of the cluster's centroid coordinates from the actual hit coordinates (1st moments), and by the wide shower profile (2nd moments) given by the number of hit counters.

Bin #	Position in PBG back blocks
1	Left Fast blocks
2	Left Slow blocks
3	Right Fast blocks
4	Right Slow blocks

Table 7.2. Position bins for electrons

We calculated the electron identification efficiency of the lead glass array for each of these bins as a function of the track's momentum (Table 7.3).

Bin #	Electron Momentum
1	$p_e < 1.5$ GeV
2	$1.5 < p_e < 2.0$ GeV
3	$2.0 < p_e < 2.5$ GeV
4	$2.5 < p_e < 3.0$ GeV
5	$3.0 < p_e < 4.0$ GeV
6	$4.0 < p_e < 5.0$ GeV
7	$5.0 < p_e < 6.0$ GeV
8	$6.0 < p_e < 7.0$ GeV
9	$7.0 < p_e < 8.0$ GeV
10	$p_e > 8.0$

Table 7.3. Momentum bins for electrons

We calculated the electron identification efficiency of the lead glass array for each of these bins as a function of the track position in the array (Table 7.2).

Comb. #	Cuts	# pass	pass	error
1	none	51232	normalization	
2	1	45360	88.54	0.57
3	2	48445	94.56	0.60
4	3	50302	98.18	0.62
5	4	46142	90.06	0.58
6	5	46604	90.97	0.58
7	1,2	43857	85.60	0.56
8	1,3	45021	87.88	0.57
9	2,3	47847	93.39	0.59
10	1,4	41488	80.98	0.53
11	2,4	44163	86.20	0.56
12	3,4	45828	89.45	0.58
13	1,5	41868	81.72	0.54
14	2,5	44824	87.49	0.57
15	3,5	46043	89.87	0.58
16	4,5	43032	83.99	0.55
17	1,2,3	43554	85.01	0.55
18	1,2,4	40292	78.65	0.52
19	1,3,4	41379	80.77	0.53
20	2,3,4	43909	85.71	0.56
21	1,2,5	40910	79.85	0.53
22	1,3,5	41589	81.18	0.54
23	2,3,5	44363	86.59	0.56
24	1,4,5	38978	76.08	0.51
25	2,4,5	41606	81.21	0.54
26	3,4,5	42799	83.54	0.55
27	1,2,3,4	40195	78.46	0.52
28	1,2,3,5	40653	79.35	0.53
29	1,2,4,5	38149	74.46	0.50
30	1,3,4,5	38886	75.90	0.51
31	2,3,4,5	41391	80.79	0.53
32	1,2,3,4,5	38063	74.30	0.50

Table 7.4. Electron identification efficiencies for PBG/FNG cuts

Cuts 1 to 5 are explained in table 7.1. The last combination corresponds to enforcing all cuts. The efficiency for a given entry is obtained by dividing the number of electrons that pass the cut over 53,126 which is the normalization sample.

Cell #	Eff In (%)	Err In	Eff out (%)	Err out
1	95.81	0.57	91.85	2.02
2	92.87	1.06	96.73	0.66
3	55.12	4.41	94.19	0.91
4	42.86	18.70	97.92	2.06
5	91.37	0.78	88.36	2.33
6	94.14	0.92	95.49	0.79
7	56.62	4.25	95.87	0.81
8	66.67	27.22	98.25	1.74
9	92.28	0.73	96.34	1.47
10	81.27	1.57	95.95	0.73
11	26.27	4.05	94.38	0.84
12	42.86	18.70	100.00	0.23
13	94.71	0.64	93.92	1.96
14	89.16	1.26	95.72	0.75
15	53.51	4.67	97.59	0.58
16	40.00	21.91	100.00	0.20

Table 7.5. Electron identification efficiencies for Čerenkov cut

Efficiencies are calculated for both inbend and outbend events as a function of the hit mirror, or cell, in the counter. Mirrors 1 to 4 (9 to 11) are the lower left (right) mirrors going from the beam out, and 5 to 8 (13 to 16) are the upper left (right) ones, also going from the beam out.

Comb. #	Cuts	# pass	% pass	error
1	none	45673	normalization	
2	1	2149	4.71	0.10
3	2	31602	69.19	0.51
4	3	36482	79.88	0.56
5	4	32169	70.43	0.51
6	5	9921	21.72	0.24
7	1,2	678	1.48	0.06
8	1,3	1922	4.21	0.10
9	2,3	24642	53.95	0.43
10	1,4	1551	3.40	0.09
11	2,4	21997	48.16	0.40
12	3,4	28723	62.89	0.47
13	1,5	635	1.39	0.06
14	2,5	8540	18.70	0.22
15	3,5	6680	14.63	0.19
16	4,5	5154	11.28	0.17
17	1,2,3	576	1.26	0.05
18	1,2,4	452	0.99	0.05
19	1,3,4	1442	3.16	0.08
20	2,3,4	19255	42.16	0.36
21	1,2,5	434	0.95	0.05
22	1,3,5	557	1.22	0.05
23	2,3,5	5562	12.18	0.17
24	1,4,5	433	0.95	0.05
25	2,4,5	4488	9.83	0.15
26	3,4,5	3821	8.37	0.14
27	1,2,3,4	410	0.90	0.04
28	1,2,3,5	376	0.82	0.04
29	1,2,4,5	312	0.68	0.04
30	1,3,4,5	397	0.87	0.04
31	2,3,4,5	3252	7.12	0.13
32	1,2,3,4,5	284	0.62	0.04

Table 7.6. Pion rejection efficiencies for PBG/FNG cuts

Cuts 1 to 5 are explained in table 7.1. The last combination corresponds to enforcing all cuts. In each case the number of charged pions that pass the corresponding cuts is divided by 46,685 (the normalization sample) to obtain the percentage of pions that pass. Subtracting this number from 100. gives the charged pion rejection efficiency of those cuts.

Selection Cuts	efficiency (%)	statistical error	systematic error
PBG/FNG	52.1	1.5	~ 1.0
Čerenkov	84.3	1.1	~ 2.0
All	44.4	1.5	~ 2.5

Table 7.7. Particle Identification efficiencies for $K_L^0 \to \pi^0 e^+ e^-$

The description of the selection cuts can be found in sections 7.1 and 7.2. Efficiencies were found from studying selected electrons from K_{e3} decays and folding in the appropriate Monte Carlo distributions for electrons from $K_L^0 \to \pi^0 e^+ e^-$ events that pass all other analysis cuts. The efficiencies in the table are independent of each other. The Čerenkov efficiency for events that have passed the PBG/FNG efficiency cut is $85.3 \pm 1.5\%$ (Sec 7.3).

Applied Cuts	Rejection Probability	Statistical Error	Rejection Factor
PBG/FNG	$1. - .0062 = .9938$	0.0004	$\sim 160 : 1$
Čerenkov	$1. - .0080 = .9920$	0.0006	$\sim 125 : 1$

Table 7.8. Charged pion rejection probabilities in $K_L^0 \to \pi^0 e^+ e^-$ analysis

By applying the electron identification cuts on charged pions from K_{e3} decays, lower bounds on their rejection probability can be established. Sections 7.1 and 7.2 detail the selection cuts.

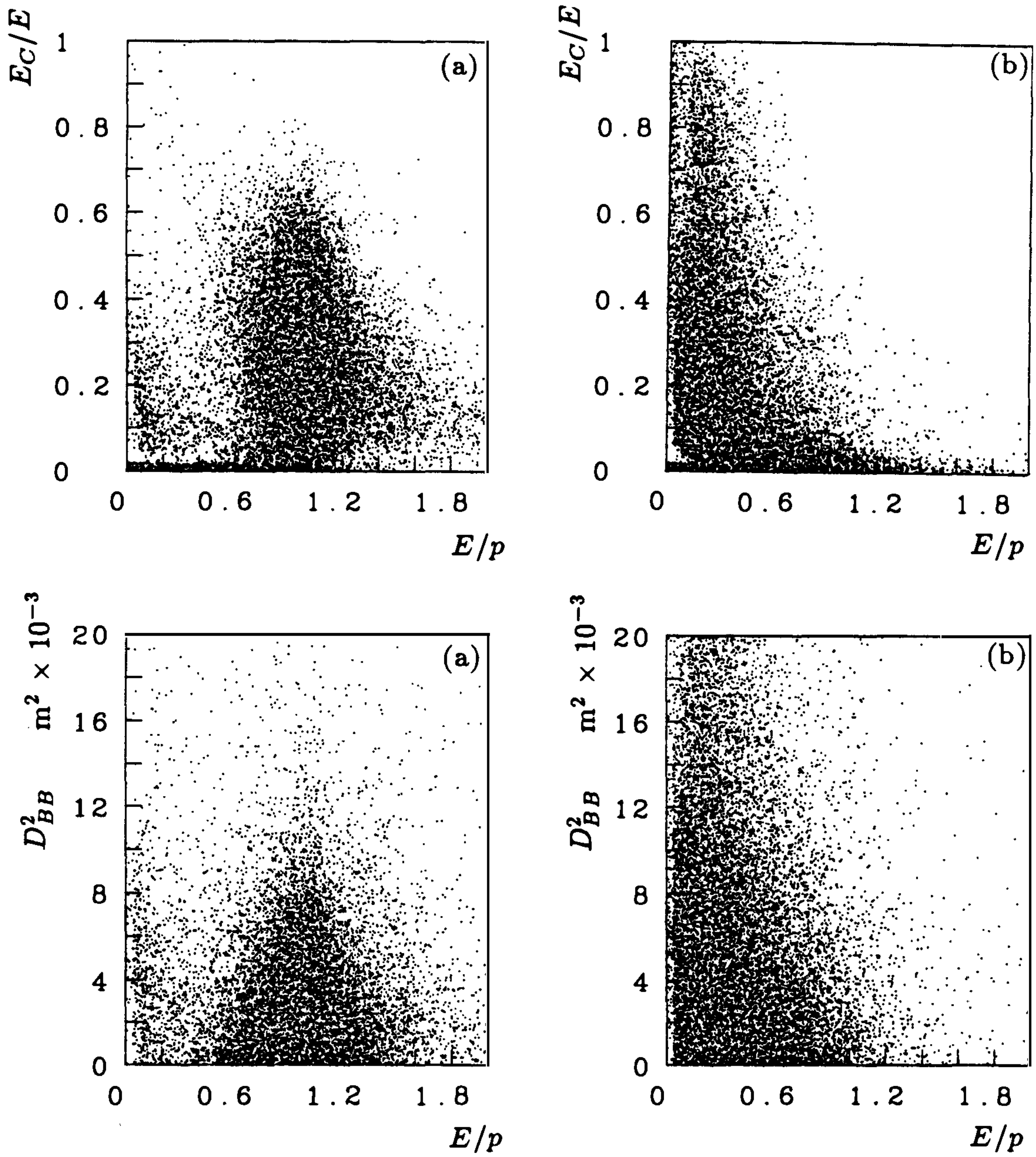

Figures 7.1 and 7.2. E_C/E and D^2_{BB} vs. E/p for electrons and pions

E_C/E is the ratio of the energy in the lead glass converters to the total energy. D^2_{BB} is the squared of the distance from the projected track to the back blocks centroid and E/p is the ratio of total energy to spectrometer momentum. Figures 7.1(a) and 7.2(a) show the correlation of these variables for electrons while figures 7.1(b) and 7.2(b) show the same correlation for charged pions.

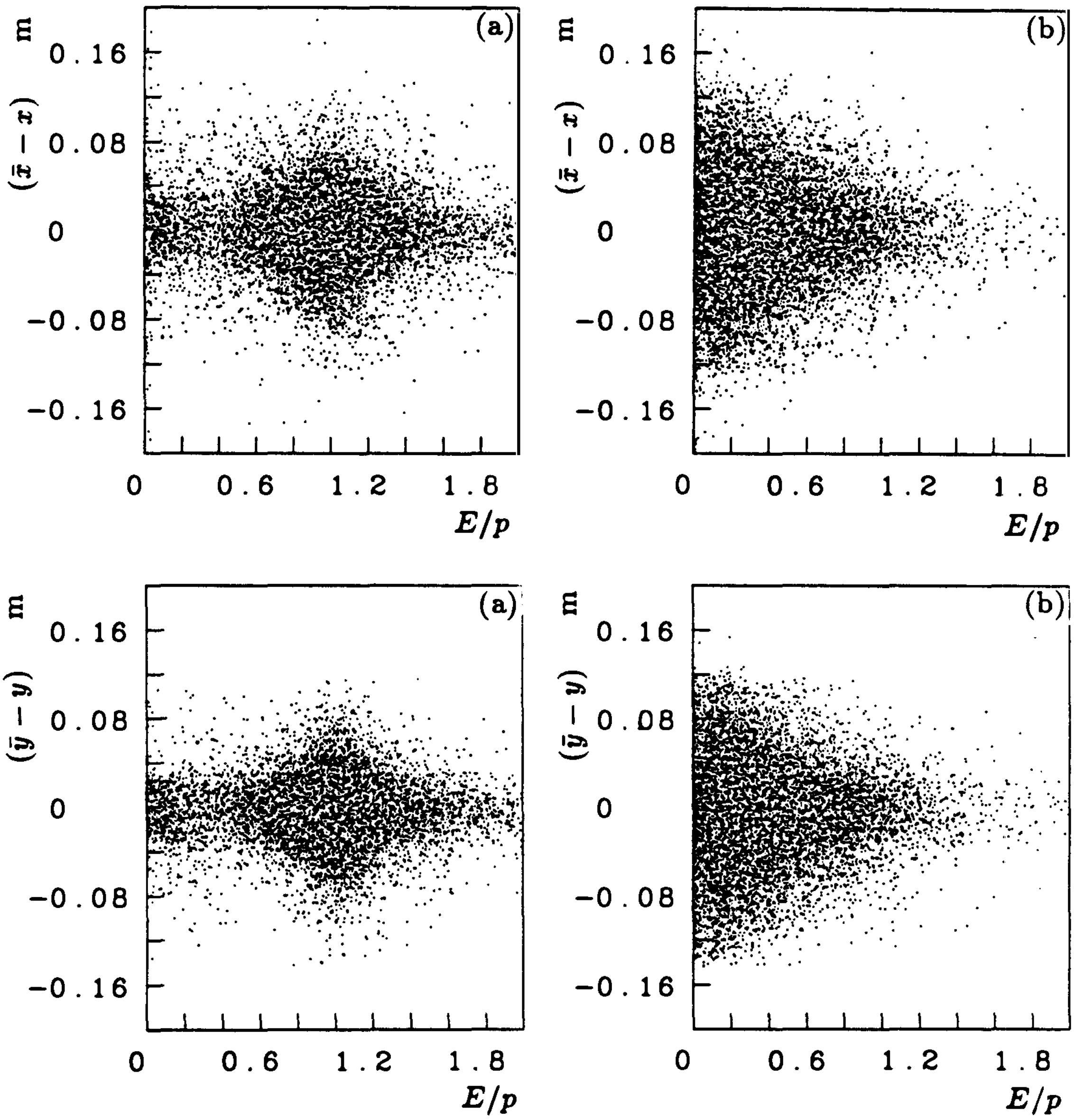

Figures 7.3 and 7.4. x, y FNG first moments for electrons and pions

$(\bar{x}, \bar{y})$ are the tracks' pulse height centroid coordinates in the finger counter array. In figures 7.3(a) and 7.3(b) the distance from $\bar{x}$ to the actual track x position (first moment) is plotted vs. E/p (the ratio of lead glass to spectrometer momentum) for electrons and charged pions, respectively. Figures 7.4(a) and (b) show the correlation of the y first moments with E/p.

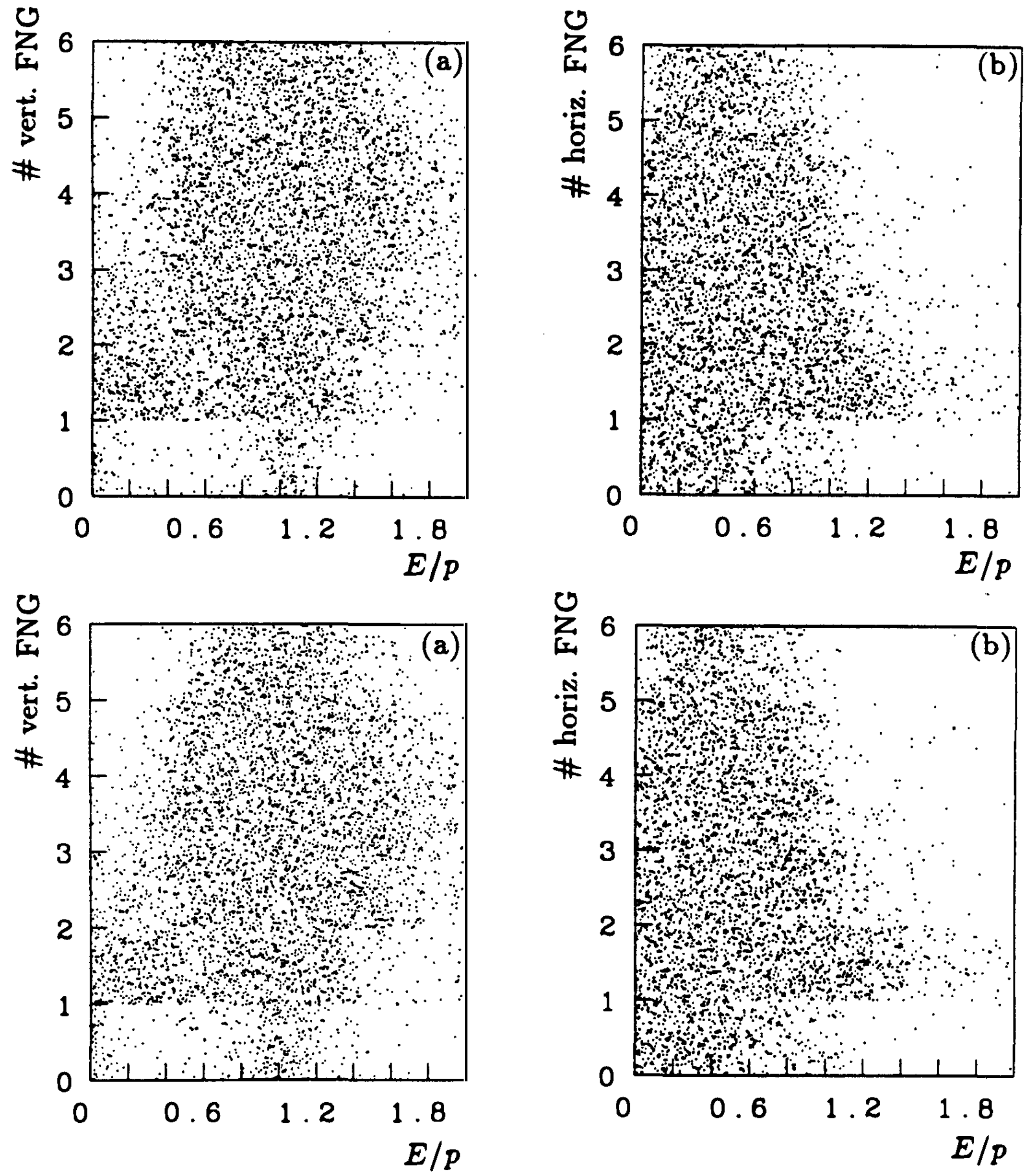

Figures 7.5 and 7.6. x, y FNG 2nd moments for electrons and pions

The FNG second moments are represented by the number of vertical and horizontal FNG counters associated with the EM shower. Figures 7.5 and 7.6 show the correlation of these moments with E/p (the energy to momentum ratio) for vertical and horizontal counters respectively. Figures (a) represent electrons while figures (b) represent pions.

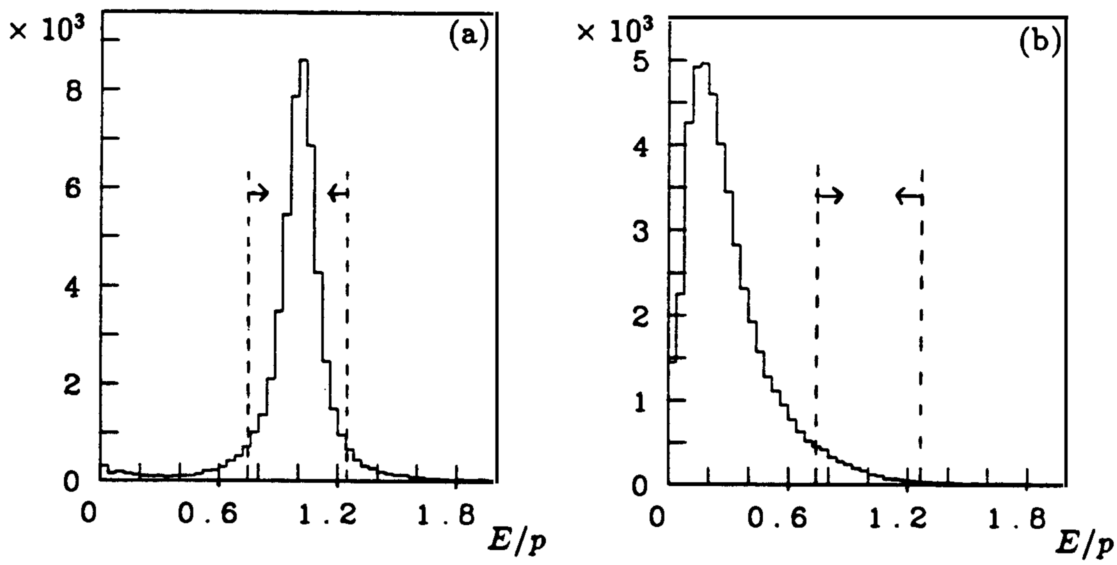

Figures 7.7. E/p for electrons and pions from K_{e3} decays

Figure 7.7(a) shows the E/p (ratio of energy to momentum) distribution for electrons while in figure 7.7(b) the charged pion E/p distribution is depicted. These histograms are the x projections of figures 7.1 to 7.6.

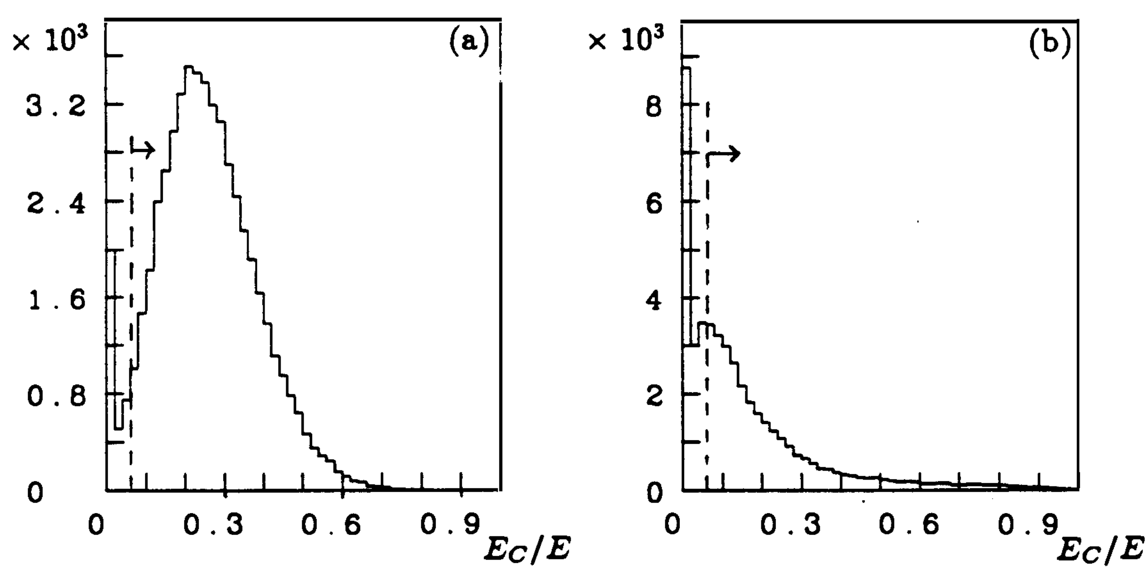

Figures 7.8. E_C/E for electrons and pions from K_{e3} decays

Figure 7.8(a) shows the E_C/E (ratio of lead glass converter energy to total energy) distribution for electrons. Figure 7.8(b) shows the charged pion E/p distribution. These histograms are the y projections of figures 7.1.

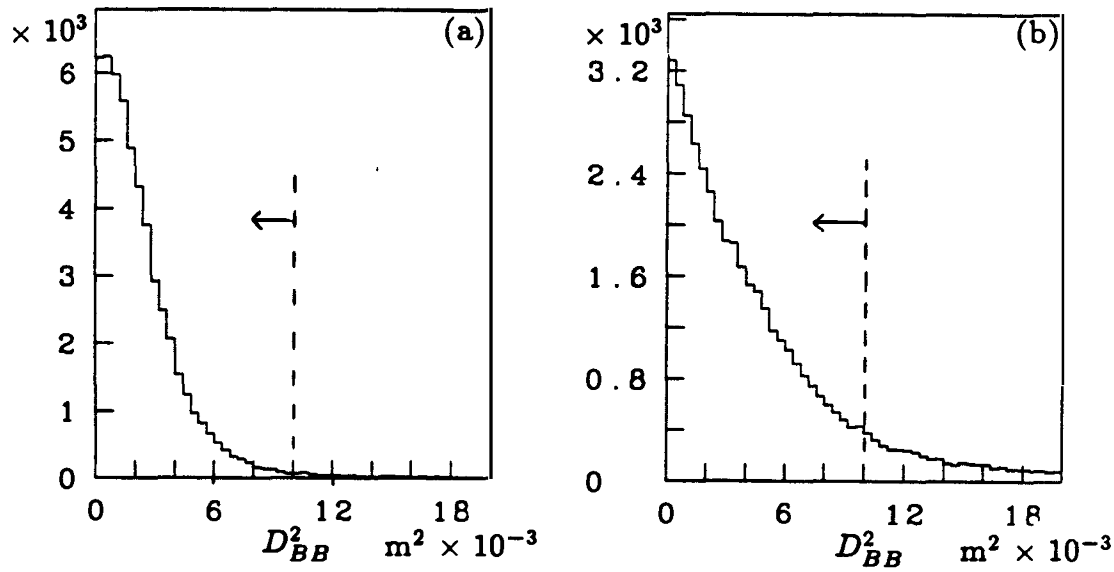

Figures 7.9. D^2_{BB} for electrons and pions from K_{e3} decays

Figure 7.9(a) shows the D^2_{BB}, squared distance from lead glass back blocks centroid to track position, for electrons. Figure 7.8(b) is the D^2_{BB} distribution for pions. These histograms are the y projections of figures 7.2.

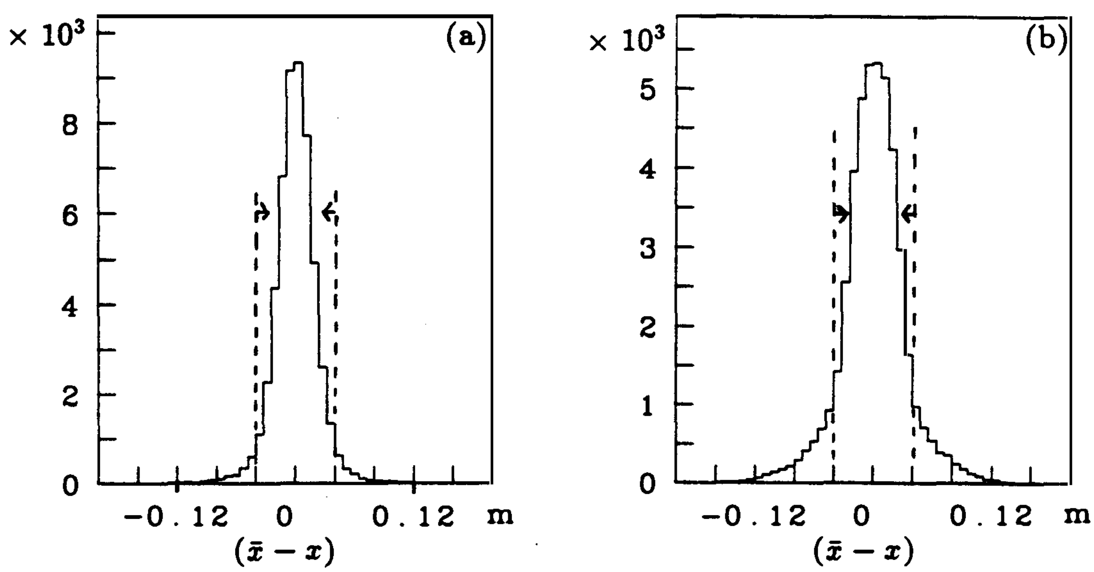

Figures 7.10. x 1st moments for electrons and pions from K_{e3} decays

Figure 7.10(a) is the distance in x from electron track FNG centroids, $\bar{x}$, to their actual x position (first moment). Figure 7.10(b) are the charged pions x first moments. These histograms are the y projections of figures 7.3.

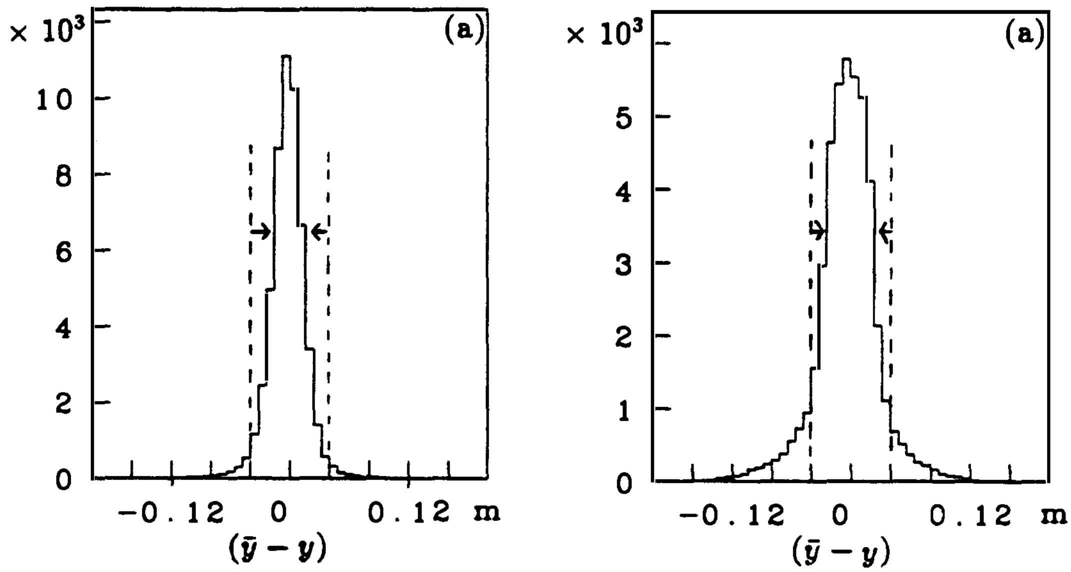

Figures 7.11. y 1st moments for electrons and pions from K_{e3} decays

Figure 7.10(a) is the distance in y from electron track FNG centroids, $\bar{y}$, to their actual y position (first moment). Figure 7.10(b) are the charged pions y first moments. These histograms are the y projections of figures 7.4.

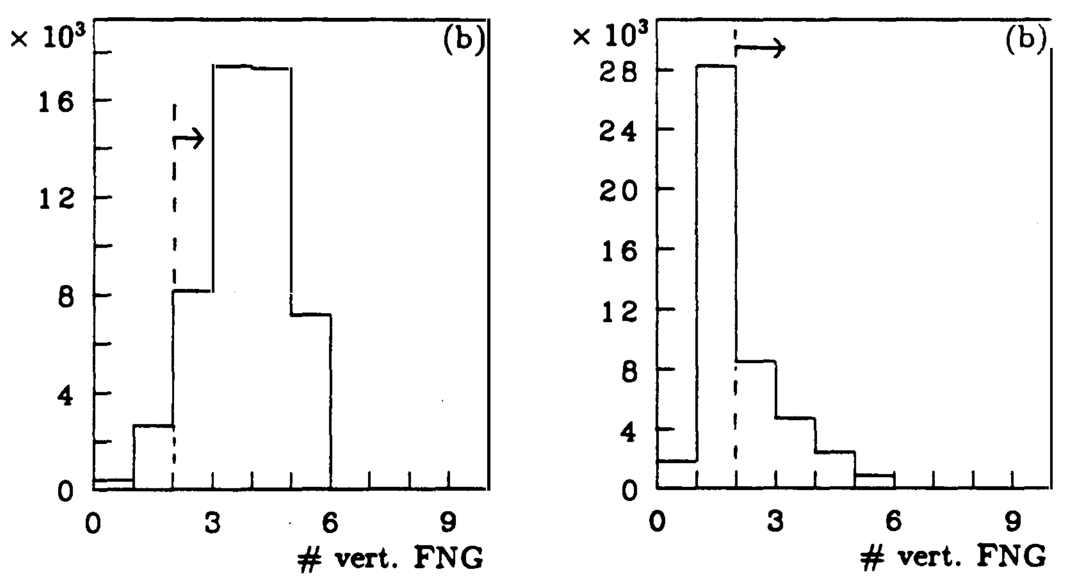

Figures 7.12. x 2nd moments for electrons and pions from K_{e3} decays

Figure 7.12(a) is the # of vertical FNG counters associated to the electron's EM shower (x 2nd moment). Figure 7.12(b) shows the charged pions x 2nd moment distribution. These histograms are the y projections of figures 7.5.

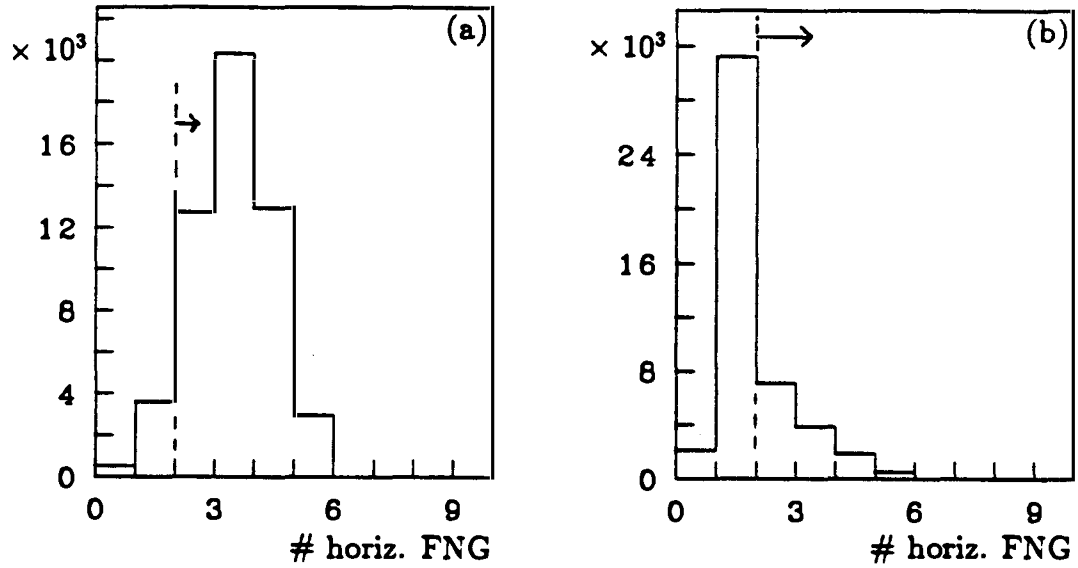

Figures 7.13. *y* 2nd moments for electrons and pions from K_{e3} decays

Figure 7.13(a) is the # of horizontal FNG counters associated to the electron's EM shower (y 2nd moment). Figure 7.13(b) shows the charged pions y 2nd moment distribution. These histograms are the y projections of figures 7.6.

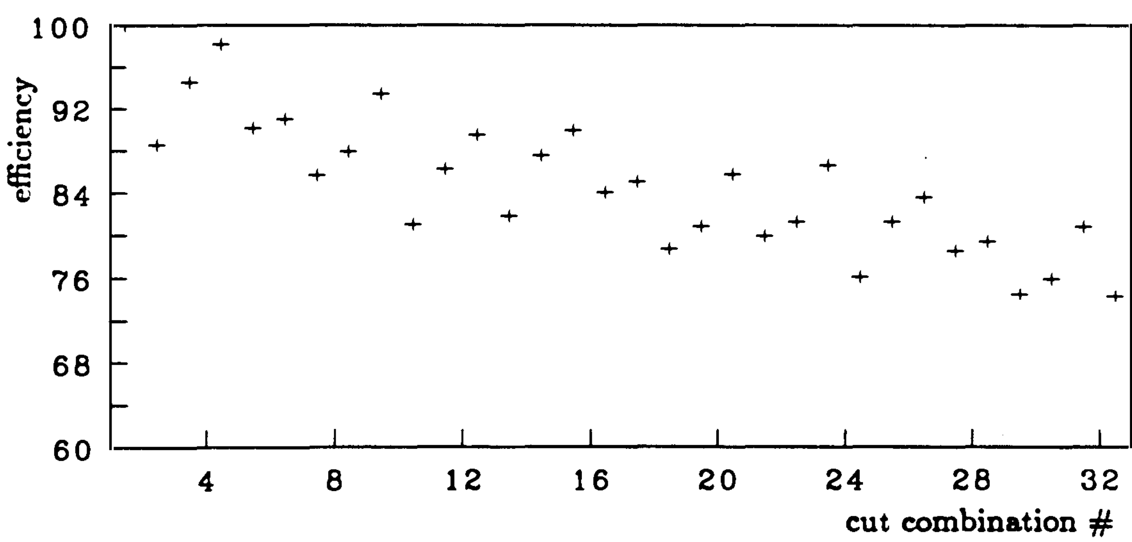

Figure 7.14. K_{e3} electron efficiency for PBG/FNG cut combinations

The combination of applied cuts corresponding to each bin is listed in table 7.4. The error bars are statistical. In combination number 32 all cuts are implemented, the resulting efficiency is 73.2%.

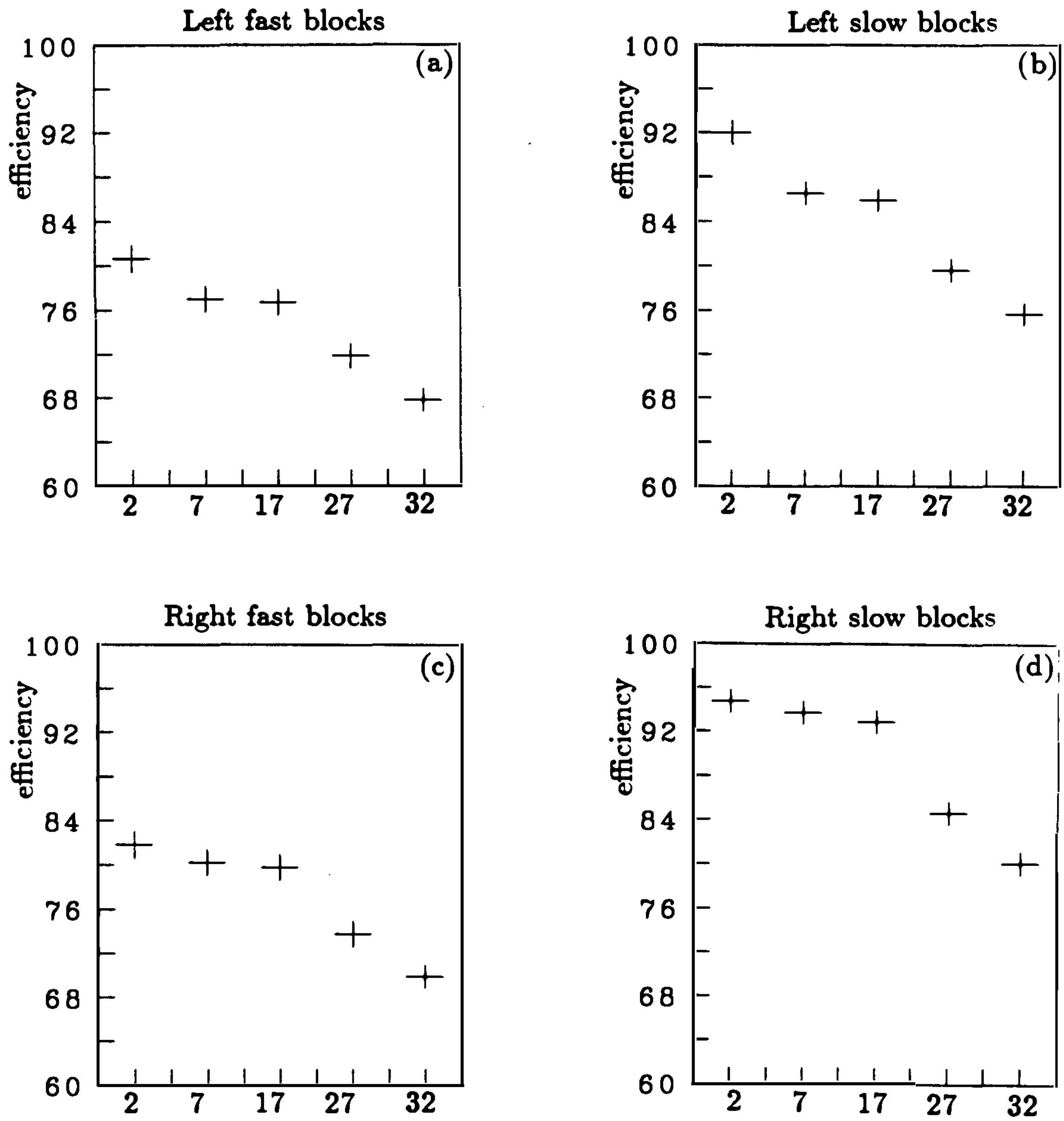

Figures 7.15. K_{e3} electron efficiencies for sequential FNG/PBG cuts.

The figures show, for the different classes of back blocks, the loss of efficiency when one after another, the five PBG/FNG cuts are implemented. The numbers in the abscissa are the cut combination numbers from table 7.4. The first entry (comb. 2) corresponds to applying only cut # 1, combination 7 corresponds to cuts 1 and 2, and so on, in sequence; combination 32 is when all five cuts are applied. The error bars are statistical.

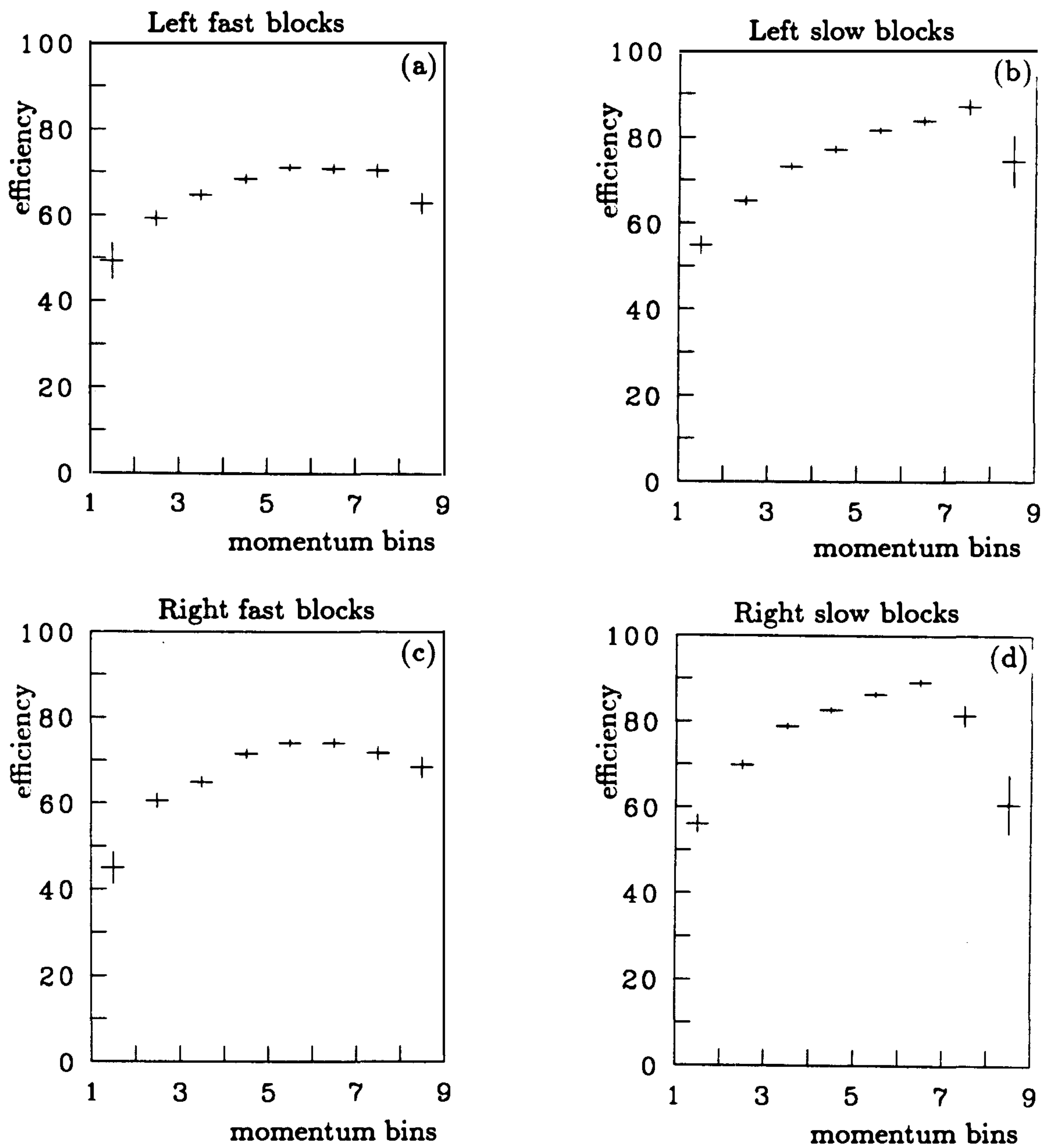

Figures 7.16. Momentum dependance of the PBG/FNG electron cuts

These plots show the efficiency of implementing all five PBG/FNG cuts on electrons from K_{e3} decays. Bins 1 to 8 correspond to the ranges of increasing momentum listed in table 7.3. From figures 7.16(a) to 7.16(d) the efficiency dependance on the back blocks classes is evident.

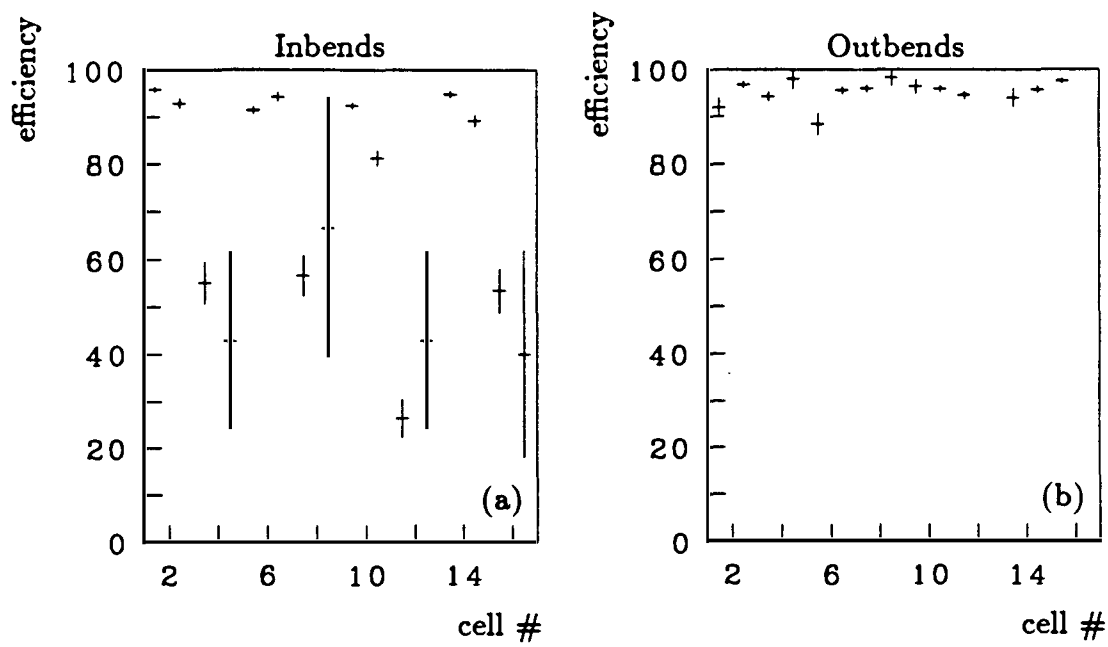

Figures 7.17. Electron identification efficiencies for Čerenkov cut

Efficiencies are calculated for both inbend, Fig. 7.17(a), and outbend events, Fig. 7.17(b), as a function of the hit mirror, or cell, in the counter. Bins 1 to 4 (9 to 11) are the efficiencies for the lower left (right) mirrors going from the beam out, and bins 5 to 8 (13 to 16) are the efficiencies for the upper left (right) ones, also going from the beam out.

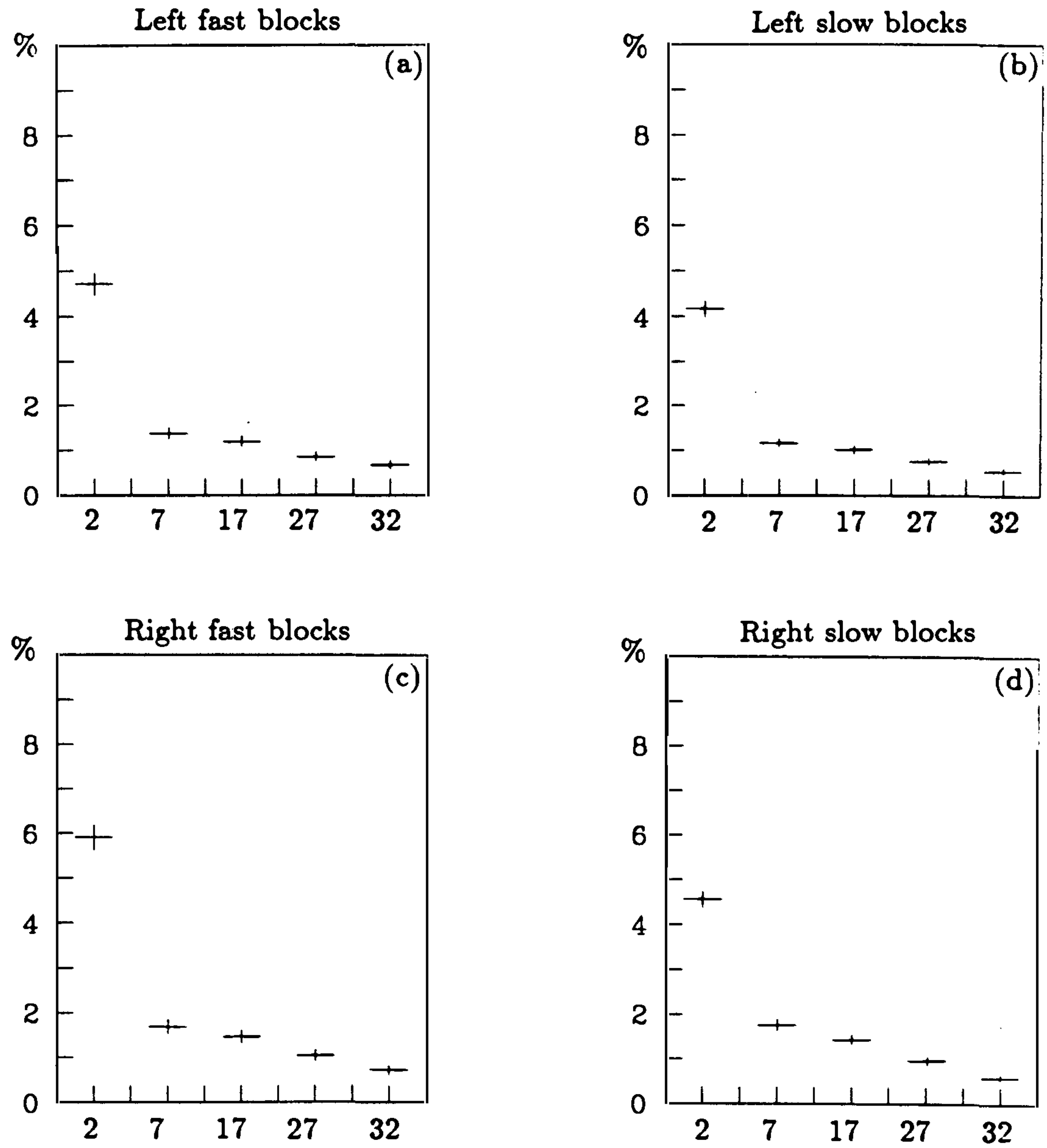

Figures 7.18. Pion residuals for sequential FNG/PBG electron cuts.

The figures show, for the different classes of back blocks, the residual percentage of pions when one after another, the five PBG/FNG electron identification cuts are implemented. The numbers in the abscissa are the cut combination numbers from table 7.4. The first entry (comb. 2) corresponds to applying only cut # 1, combination 7 corresponds to cuts 1 and 2, and so on, in sequence; combination 32 is when all five cuts are applied. The error bars are statistical.

Account for:	Factor	Error	Sensitivity
$N_{\pi^0\pi^+\pi^-}$	—	1.5%	1.01×10^{-8}
$A_{\pi^0\pi^+\pi^-}/A_{\pi^0e^+e^-}$	6.60	3.5%	6.67×10^{-8}
L1 electronic bit efficiency, $(\epsilon^a_{\mathrm{L1}})^{-1}$	$(.985)^{-1}$	—	6.77×10^{-8}
L1 photon condition, $(\epsilon^b_{\mathrm{L1}})^{-1}$	$(.982)^{-1}$	1.0%	6.89×10^{-8}
Electron Id. efficiency, $(\epsilon_{\mathrm{ID}})^{-1}$	$(.444)^{-1}$	2.5%	1.55×10^{-7}
L3 trigger efficiency, $(\epsilon^a_{\mathrm{L3}})^{-1}$	$(.691)^{-1}$	2.1%	2.25×10^{-7}
L3 two-track colinearity loss, $(\epsilon^b_{\mathrm{L3}})^{-1}$	$(.850)^{-1}$	1.2%	2.64×10^{-7}
$\pi^{\pm}$ interactions, (f_π)	.985	1.0%	2.6×10^{-7}
90% C.L. correction	2.3	—	6.0×10^{-7}

Table 8.1. Correction factors in $K^0_L \to \pi^0 e^+ e^-$ sensitivity estimate

This table lists the factors used in order to obtain the sensitivity of our $K^0_L \to \pi^0 e^+ e^-$ search. 1.01×10^{-8} is the single event sensitivity for $K^0_L \to \pi^+\pi^-\pi^0$, obtained by dividing the branching ratio for $K^0_L \to \pi^+\pi^-\pi^0$ by the effective number of observed events ($N_{\pi^0\pi^+\pi^-}$). $A_{\pi^0\pi^+\pi^-}/A_{\pi^0e^+e^-}$ is the $K^0_L \to \pi^+\pi^-\pi^0$ to $K^0_L \to \pi^0 e^+ e^-$ acceptance ratio (Chapt. 6). $\epsilon_{\mathrm{L1}} = \epsilon^a_{\mathrm{L1}} \cdot \epsilon^b_{\mathrm{L1}}$ is the total L1 efficiency in the recipee for the $K^0_L \to \pi^0 e^+ e^-$ sensitivity calculation in section 8.1. $\epsilon_{\mathrm{L3}} = \epsilon^a_{\mathrm{L3}} \cdot \epsilon^b_{\mathrm{L3}}$ is the total L3 efficiency. The resulting limit to the $K^0_L \to \pi^0 e^+ e^-$ branching ratio is 6.0×10^{-7}. The errors added in quadrature give a total error of 5% in the calculation.

Experiment	Features	Limit	Date
Carroll et al.	Observed 4 $K_L^0 \to e^+e^-\gamma$ events	2.3×10^{-6}	PRL 44, 525 (1980)
BNL E780 (AGS)	Optimized for $K_L^0 \to \mu e$	3.2×10^{-7}	PRL 61, 2300 (1988)
CERN NA-31 (SPS)	Designed for $\lvert\epsilon'/\epsilon\rvert$, $\pi^0 e^+e^-$ from their $\pi^0\pi^0$ trigger. Taking data in 1989, expect ~ 2 better	4.0×10^{-8}	PL 214B, 303 (1988)
BNL E791 (AGS)	Optimized for $K_L^0 \to \mu e$	6.0×10^{-7}	1989
FNAL 731 (Tevatron Meson Center)	Designed for $\lvert\epsilon'/\epsilon\rvert$, $\pi^0 e^+e^-$ from their $\pi^0\pi^0$ trigger. 800 GeV/c proton beam, expect ~ 5 better	4.2×10^{-8}	PRL 61, 2661 (1988)
	Next generation: dedicated and/or optimized for $K_L^0 \to \pi^0 e^+e^-$ $\Downarrow$		
BNL E845 (previous E780)	High acceptance: smaller mag. field, Č inside magnet. Added veto counters, same 780 Pb glass	few 10^{-11} in proposal	1989-1990
KEK 164	High acceptance. CsI EM Calorimeter: good energy and position resolution, extra $\pi\|e$ separation	$\sim 5 \times 10^{-11}$ in proposal	~ 1991
FNAL 799 (previous E731)	Higher beam intensity and acceptance. TRD detector for better $\pi\|e$ separation. BaF_2 calorimeter	$10^{-10} \to 10^{-11}$ in two stages	$\sim 1990 - 1991$ $\sim 1991 - 1992$

Table 8.2. Status of $K_L^0 \to \pi^0 e^+ e^-$ Experiments.